5-17-07
0633
ENTERED FM 5-21-07

Final Technical Report

Project Title: Virtual Welded-Joint Design Integrating Advanced Materials and Processing Technologies

Award Number: DE-FC36-01ID14242

Project Period: Oct. 1, 2001 through Mar. 31, 2005

Recipient: Caterpillar Inc.
P.O. Box 1875
Peoria (Peoria County), Illinois 61656-1875

Project Manager: Howard W. Ludewig, (309) 578-4469, Ludewig_Howard_W@cat.com

Principal Investigator: Zhishang Yang, (309) 578-2761, Yang_Zhishang@cat.com

Co-PIs at Team Member Organizations:
Battelle Memorial Institute, Pingsha Dong, (614) 424-4908, dongp@battelle.org
Colorado School of Mines, Stephen Liu, (303) 273-3796, sliu@mines.edu
Oak Ridge National Laboratory, Suresh Babu, (865) 574-4806, babuss@ornl.gov
QuesTek Innovations, LLC, Greg Olson, (847) 425-8220, golson@questek.com
The Pennsylvania State University, Tarasankar DebRoy, (814) 865-1974, rtd1@psu.edu

Acknowledgment, Disclaimer and Proprietary Data Notice

Acknowledgment: This report is based upon work supported by the U. S. Department of Energy under Award No. DE-FC36-01ID14242.

Disclaimer: Any findings, opinions, and conclusions or recommendations expressed in this report are those of the authors and do not necessarily reflect the views of the Department of Energy

Proprietary Data Notice: This report does not contain proprietary data (limited rights data), classified information, information subject to export control classification, or other information not subject to release.

Table of Contents

Lists of Figures

Lists of Tables

Executive Summary

Primary Objectives:

The primary goal of this project is to increase the fatigue life of a welded-joint by 10 times and to reduce energy use by 25 percent through product performance and productivity improvements using an integrated modeling approach. The fatigue strength of a welded-joint is currently the bottleneck to design high performance and lightweight welded structures using advanced materials such as high strength steels.

In order to achieve high fatigue strength in a welded-joint it is necessary to manage the weld bead shape for lower stress concentration, produce preferable residual stress distribution, and obtain the desired microstructure for improved material toughness and strength. This is a systems challenge that requires the optimization of the welding process, the welding consumable, the base material, as well as the structure design.

Project Scope

The concept of virtual welded-joint design has been proposed and established in this project. The goal of virtual welded-joint design is to develop a thorough procedure to predict the relationship of welding process, microstructure, property, residual stress, and the ultimate weld fatigue strength by a systematic modeling approach. The systematic approach combines five sub-models: weld thermo-fluid model, weld microstructure model, weld material property model, weld residual stress model, and weld fatigue model. The systematic approach is thus based on interdisciplinary applied sciences including heat transfer, computational fluid dynamics, materials science, engineering mechanics, and material fracture mechanics. The sub-models are based on existing models with further development. The results from modeling have been validated with critical experiments.

The systematic modeling approach has been used to design high fatigue resistant welds considering the combined effects of weld bead geometry, residual stress, microstructure, and material property. In particular, a special welding wire has been developed in this project to introduce compressive residual stress at weld toe for weld fatigue resistance.

Results:

Two major technologies have been generated from this project: (1) a systematic simulation approach for virtual welded-joint design and (2) a technology to increase the fatigue strength of high strength steel welds by the combination of compressive residual stress from special welding wire and the desired weld bead shape from a unique welding process. In virtual welded-joint design, the accomplishments in modeling include:

1. Development of a 3D thermo-fluid model to predict weld bead shape for Gas-Metal-Arc (GMA) welding with free surface, which can be used to design welding parameters for desired weld bead shape;
2. Modification of a weld microstructure model to predict the phase transformations and grain growth in the weld fusion zone and heat affected zone;
3. Establishment of the relation of weld properties (strength, hardness, stress-strain curves) vs. weld microstructure;
4. Enhancement of a weld residual stress model by the incorporation of the effects of phase transformations (e.g. volume change and transformation induced plasticity);
5. Development of a two-stage crack growth model for the weld fatigue life prediction considering the effect of residual stress.

The accomplishments for practical applications in this project include the development of a unique welding procedure (welding wire + welding process) for making fatigue resistant welded-joints. The weld bead shape with larger toe radius and thus lower stress concentration was obtained by adopting a Caterpillar proprietary welding process through optimizing welding parameter. The compressive residual stress at weld toe was achieved by using special welding wires. The results from neutron and x-ray diffraction analysis show that compressive residual stresses were formed in the welded-joints using special welding wires. In contrast, tensile residual stresses exist at the weld toe using conventional welding wire. More than 10 times fatigue life improvement has been achieved in high strength steel welds by the combination of the desired weld bead shape and compressive residual stresses.

Conclusions:

The results from this project have clearly demonstrated that the fatigue strength of high strength steel welds can be significantly improved by the systematic design approach considering the weld bead shape, residual stress, and microstructure. In particular, the following conclusions can be made based on the results from this project:

1. The 3D transient thermo-fluid model developed in this project is able to simulate the complex heat transfer and fluid flow phenomena in GMA weld pool. The model can be used to predict weld bead formation for various types of welded-joints including butt and T-fillet joints. The results here indicate the significant promise to use weld thermo-fluid model to design desired weld bead shape for high performance welded-joint.
2. The inhomogeneous microstructures in both the weld fusion zone and the heat-affected zone can be predicted by coupling a modified weld microstructure model with the thermal cycles from thermal model. Some weld material properties such as yield strength and hardness can be predicted accordingly based on the predicted microstructures.
3. The effect of phase transformations on weld residual stress formation can be effectively simulated after the incorporation of the transformation-induced plasticity in the residual stress model.
4. The structural stress based two-stage crack growth weld fatigue model is effective in the prediction of the effect of residual stress on weld fatigue life.
5. The special welding wire developed in this project can introduce compressive residual stress at weld toe.
6. The fatigue life/strength in high strength steel welds can be significantly improved by the combination of weld bead shape, residual stress, and microstructure.

Technology Transfer and Commercialization:

For the purpose of technology transfer and commercialization, one technical paper has been published in a peer-reviewed journal and 5 technical papers have been published in conference proceedings. Nine technical presentations have been made at International conferences and 3 presentations made at Corporate level technical forum within Caterpillar. An advisory committee, which includes members from different industrial sectors, welding institutes (Edison Welding Institute and The Welding Institute), and national laboratories, was formed to diffuse the technologies developed in this project.

The models developed in this project have been applied within Caterpillar for both R&D and technical assistance projects. Caterpillar has also allocated new research funding to further evaluate and benchmark the welding wire and procedure for fatigue life improvement in high strength steel welds. The ultimate goal is to apply the fatigue resistant welded-joints for the design of high performance and lightweight fabricated structures.

Recommendations:

1. Further development is needed for the 3D transient thermo-fluid model, which should include the enhancement of the simulation of the effect of surface tension on the small droplets from welding wire.
2. For general engineering design applications, the fracture mechanics based fatigue model developed in this project should be further validated and refined by comparing fatigue life predictions with experimental testing for some selected joint types in which more complex 3D residual stress distributions dominate.
3. The individual models so far can only be manually "integrated" due to the challenges such as different software involved and the long computational time for the weld thermo-fluid model. The models ideally should be integrated using a unified framework, which needs further research on model integration and the speed up of the welding pool simulation.
4. Further evaluation and benchmark of the special welding wire are recommended before applying this technology.

I. Introduction

I.1: Description of the Technology

Attempts to improve fuel economy in both on-highway and off-highway vehicles are accelerating due to energy shortage and environmental factors. Global competitions have forced the heavy manufacturing industry to increase product life, reduce manufacturing cost, and improve the customer owning and operation cost. "Use of cost-effective light weight materials" and "reduction of transportation cost" have been highlighted in the technology roadmaps for future mining industry. Producing lighter weight structures by using high strength materials such as High Strength Low Alloy (HSLA) steels or aluminum alloys over conventional structural steels is limited by the weakness of weld joint that determines the life of the fabricated structures. The most significant technological innovations in loading and hauling industry related to mining will take place in load capacity improvement accompanied by efficiency and product reliability.

The focus of the project is the fatigue strength of welded-joints in high strength steels. It is well known that placement of a weld on a cyclically stressed member can drastically reduce the fatigue strength of the structure. The failure is due to either stress concentration at the weld toe associated with a sharp change of weld bead geometry, welding induced tensile residual stresses, or welding induced change of microstructure and material property, etc. The complex nature of the problem coupled with lack of the system knowledge and predictive tools makes it very difficult for industry to predict and to prevent the early failure of the product in service.

The major technical barriers related to develop fatigue resistant welds for high strength steels include: (1) Limited knowledge and no effective methods available on how to make welds with desired bead shape, residual stress, and microstructure to improve the fatigue strength of high strength steel welded-joints; (2) High tensile residual stresses, which accelerate the fatigue crack propagation and reduce weld fatigue life, are usually formed in high strength steel welds; (3) Lack of systematic approach to improve weld fatigue strength.

This is a systems challenge that requires the optimization of the welding process, the welding consumable, the base material, as well as the structure design. This project has developed an integrated modeling and simulation tool for addressing these issues in a systems approach, as shown in Figure 1.

The systematic approach combines five sub-models: weld thermo-fluid model, weld microstructure model, weld material property model, weld residual stress model, and weld fatigue model. The systematic approach is thus based on interdisciplinary applied sciences including heat transfer, computational fluid dynamics, materials science, engineering mechanics, and material fracture mechanics. The sub-models are developed based on the existing models.

The systematic modeling approach can lead to an optimized welded-joint design considering combined effects of weld bead geometry, residual stress, microstructure, material property, and the final fatigue strength. A unique welding procedure (process+wire) has been developed to improve the fatigue strength of high strength steel welds for lightweight and high performance structures. In particular, special welding wires have been developed and evaluated in this project to introduce compressive residual stress at weld toe for the fatigue life improvement.

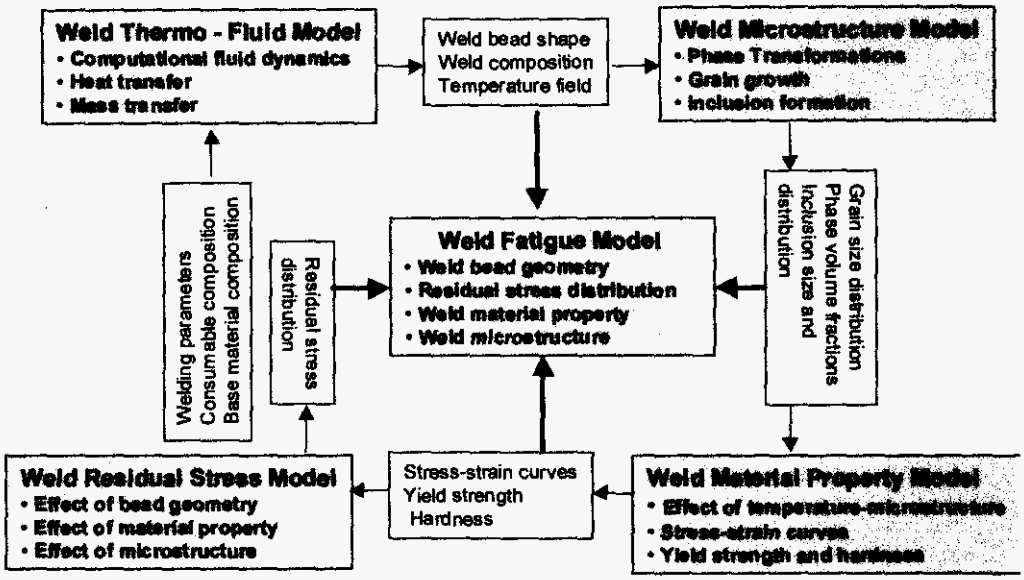

Fig. 1: A systems approach for virtual design of welded-joints.

I.2: Potential Applications And Energy Savings

The significant fatigue strength improvement for high strength steel welds can have fundamental impact on the application of high strength steels in many industrial sectors such as mining, shipbuilding, bridges, and automotive. The estimated energy savings in mining industry alone will be 10.22 trillion BTU/year through the implementation of the technologies developed in this project. The savings in energy will result from three parts: (1) Lightweight welded-structures for loading and hauling machines in mining: the weight reduction in front linkage and truck bodies will increase the capacity for loading and hauling and reduce fuel consumption. This will result in the saving of energy 7.32 trillion BTUs. (2) Energy saving in making steel: assuming that better welded-joint design will lead to the more use of high strength steels, which in turn will enable a 15 percent reduction in the total weight of the vehicle structures for mining, the total energy saving for steel making will be 2.85 trillion BTUs; (3) Energy saving in manufacturing: Less energy will be used in making the welding wire and welding process due to smaller weld size for thinner plate of high strength steels. The estimated energy saving for this part is 0.047 trillion BTU/year. The total carbon emission reduction for mining industry is estimated to be 0.6 MMTCe by year 2020 through weight reduction and reduced welding emission.

II. Background

II.1: Relevant Technologies

In fabricated structures, weld fatigue life is the limiting design factor affecting the reliability of the product. Previous work shows that the fatigue life of welded joint can be significantly improved by obtaining desired weld bead shape through the reduction of stress concentration. During 1995-1999, Caterpillar conducted a $20M NIST sponsored advanced technology program, "Fabrication of Advanced Structures using Intelligent and Synergistic Material Processing (FASIP)," to improve the fatigue life of welded structures. The project developed procedures for desired weld bead shape, FASIP weld, to reduce stress concentrations, which can lead to significant fatigue life improvement. However, the focus of FASIP program was conventional mild steels, which accounts for more than 95% steels currently used in CAT's welded structures. Compared to the welding of conventional mild steel, welding of high strength steel has many new challenges such as higher weld tensile residual stresses and poor weldability. The effect of weld residual stress on fatigue life has not been systematically investigated. In addition, the computer simulation model developed in FASIP project was primarily used for welding distortion prediction in mild steel. The effect of phase transformations on weld residual stress, which is critical to the welding of high strength steels, was not considered in the previous code.

Integrated weld process modeling is an emerging technology throughout the world. European countries have invested in sub-process models and methods to integrate them for virtual component design [15]. The initial efforts indicate that welding fabrication issues can only be effectively addressed by considering joint design and intended performance along with material characteristics and weldability. This requires certain critical technologies: (1) Physics-based process simulation tools that can capture important material and process interactions; and (2) A robust modeling-based framework that allows engineers to correlate process-specific (often multi-physics based) and design simulation results and to make decisions based on all the interactions among materials, joining processes and design characteristics. However, the above mentioned models are not capable of simultaneously predicting weld bead shape due to weld pool formation, microstructure evolution in the weld fusion zone, and the effect of weld residual stresses on the weld fatigue life.

Many US manufacturers, like Caterpillar, have initiated or are initiating integrated product and process development (IPPD). In this approach, production processes related to product development are integrated in computer based virtual manufacturing environments. IPPD will optimize material processes, improve product quality, significantly reduce the manufacturing cost and shorten the product development cycle. However, current weld models are isolated and inadequate to realize the full potential of IPPD. The demand from industry thus provides a driving force to assemble all of the essential models to design high performance welded-joints. As the end user, industry needs a thorough understanding of relationships among material characteristics, weldability, manufacturability, and joint performance. The research reported here represents the first effort in this area.

II.2: Project Team

To achieve the ambitious goal proposed in this project, the world-class experts in each individual research area have worked as a team for the development of the systematic modeling approach.

Caterpillar Inc is the world leader in the design and manufacturing of mining and construction equipment. Fabricated structures make up 30 percent of Caterpillar's $30 billion annual business, and welding is a major fabrication process, so Caterpillar has been proactively pursuing welded-joint improvement technology. As mentioned previously, Caterpillar has made tremendous efforts in developing advanced welding technologies for weld fatigue life improvement, which including the $20M NIST sponsored FASIP program. The Virtual Welded-Joint Design project builds on the technology developed under the FASIP program. Caterpillar has led this project based on industry needs. Caterpillar has coordinated the project research activities, led the development of weld models, coordinated the experimental validation, and provided technology transfer to industry.

Battelle Memorial Institute (Battelle) is a non-profit research and development corporation and, they have been modeling welding processes and structures for over 30 years. Battelle has worked with Caterpillar in FASIP project to

develop thermal-mechanical models for weld stress analysis and distortion control for large welded structures. Battelle has led the weld fatigue model development. Battelle also made contributions in the development of the 3D transient weld thermo-fluid model and the enhancement of the weld residual stress model.

Oak Ridge National Laboratory (ORNL) is a multi-program science and technology laboratory managed for the US Department of Energy (DOE) by a partnership composed of Battelle and the University of Tennessee. The laboratory has significant capabilities in process-microstructure-property model development and advanced characterization of weld microstructures and residual stresses using neutron and synchrotron diffractions. The contributions of ORNL in this project include (1) Determination of the stress-strain curves for the steels using the Gleeble thermal mechanical simulator; (2) Development of an experimental based model to predict stress-strain curves for the investigated steels; and (3) Measurement of weld residual stress using neutron and x-ray diffractions.

Colorado School of Mines (CSM) The Center for Welding, Joining, and Coatings Research has made significant contributions in welding metallurgy and materials joining. In the past 10 years, they have accumulated significant experience in weld consumable design. In this project, CSM has designed and manufactured a special weld consumable to provide the desired residual stress distribution in a weld joint through controlled phase transformations.

QuesTek Innovations LLC (QuesTek) is commercializing the modeling-based systems approach for material design in collaboration with the Steel Research Group at Northwestern University. The approach was adopted in this project to develop advanced structural materials and weld consumables.

The Pennsylvania State University (Penn State) Department of Materials Science and Engineering at Penn State has an active program to develop computer models and new experimental tools to solve welding problems. Much of their work has involved the application of transport phenomena to quantitatively understand the geometry, composition and microstructure of welds. In this project, Penn State has modified their in-house weld thermo-fluid code and developed the quasi-steady state weld thermo-fluid model with free surface.

III. Results and Discussions

The results from the three primary tasks carried out in this project (e.g. model development; special welding wire design; and technical demo) are presented in this part. In the model development, the individual models developed in this project are described with details on the background of the models, the principles and theories, formulations, and validations. For the special welding wire design, relevant information has been presented including background, wire composition design, and the evaluation of the weldability, residual stress, and properties from the designed welding wire. In the technical demo part, the primary focus is the fatigue life improvement for high strength steel welds. The welding process and welding wire to achieve the desired weld bead shape and residual stresses for the fatigue life improvement are discussed. The fatigue test and modeling results are also presented in this section.

III. 1: Model Development in Virtual Welded-Joint Design

III. 1.1 Weld Thermo-Fluid Model

III.1.1.1: Background on Weld Pool Simulation

The weld bead shape is determined by the heat transfer and fluid flow in the weld pool. The fluid flow inside weld pool affects the heat transfer in weld pool, the uniformity of weld composition, and the final weld bead profile. Furthermore, the thermal cycles experienced by the heat-affected zone during a welding operation determines solid-state transformations, thereby influencing the microstructure. In addition, weld bead profile is one of the critical factors in the specification for a welded-joint design since it has a direct influence on welded structure stresses, weld joint strength, and fatigue life. Therefore, it is crucial to establish an accurate thermo-fluid model to simulate the entire welding thermal and fluid processes to obtain the desired weld bead profile and thermal history for structurally sound and high performance welded-joint design.

The Gas Metal Arc (GMA) welding process, the welding process investigated in this project, is one of the most commonly used joining methods because of its high productivity and process robustness. During GMA welding, weld metal is deposited into a weld pool from electrode as a droplet stream. The metal transfer mechanisms play an important role in determining the resulting heat and fluid flow characteristics and final weld profile. The heat content and impact force of droplets tend to induce a series of physical, chemical, and metallurgical changes in the weld pool. Therefore, it is difficult to simulate GMA welding process, mainly due to the droplet impact and the large flow and temperature gradients associated with this process. It has been realized that a better understanding of droplet impact effects on weld heat transfer and fluid flow is critical to determine welding procedures and to predict weld bead profiles.

To date most investigations of fluid flow in weld pools have concentrated on gas tungsten arc (GTA) welding processes, without including the complexity of metal transfer across the plasma. Unfortunately, little work has been done in the area of fluid flow and heat transfer in GMA weld pools due to its complexity. Considering the challenges of this task, two approaches have been taken in weld pool simulation in this project. The first approach is to develop a 3D transient weld thermo-fluid flow model based on a commercial software, FLOW3D® [1], which was primarily used for casting simulation. In this project, special user subroutines have been developed for FLOW3D® to make it suitable for the simulation of GMA welding process. The second approach is to further develop a quasi-steady state weld pool model based on Penn State's in-house code to simulate GMA welding pool with free surface. The transient model from the first approach can explicitly simulate the interaction of metal droplet with the weld pool due to FOLW3D®'s excellent capability in handling the free surface. However, the computational time is relatively longer with around 20 hrs for a typical simulation. The quasi-steady model from the second approach takes much shorter time than the first model. However, the quasi-steady state model cannot explicitly simulate some essential features for GMA welding process such as the addition of metal droplet from welding wire. Thus, many assumptions have to be made in the second model.

III.1.1.2: 3D Transient Weld Pool Simulation

III.1.1.2.A: Model Description

Battelle and Caterpillar worked together to develop the customized user subroutines in FLOW3D for the simulation of GMA weld pool formation. Flat and fixed weld pool surface was assumed in most available weld thermo-fluid models due to the challenges to track the moving free surface and the extensive computation time. However, the fixed flat weld pool surface is not sufficient to predict some essential features of the weld bead shape such as weld toe geometry, which is the pre-requisite for accurate prediction of weld residual stress and fatigue strength.

In order to simplify the mathematical model, the following additional assumptions have been adopted: (1) the flow is Newtonian and laminar, and compressibility is only included through the buoyancy term and the Boussinesq approximation, (2) physical properties, as listed in Table 1, are constant with temperature, and (3) the arc is regarded as a spatially distributed source of heat, current, and pressure flux.

Table 1: Parameters used in weld thermo-fluid calculation (the meaning the of symbols are listed in Appendix A)

K_s	32.3(solid)	W/m K	h_c	100	W/m^2 K
K_l	26.9(liquid)	W/m K	L_f	2.77×10^5	J/kg
C_p	732	J/kg K	L_e	7.34×10^6	J/kg
ρ	6900	Kg/m^3	L	12.7	mm
μ	5×10^{-3}	Kg/m s	σ_q	4	mm
μ_o	1.26×10^{-6}	H/m	σ_j	2	mm
γ	1	N/m	u_o	5	mm/s
γ_T	-0.2×10^{-3}	N/m K	I	210	A
β	1.0×10^{-4}	K^{-1}	V	30	V
T_v	2900	K	V_d	500	mm/s
T_l	1798	K	F_d	400	drops/second
T_s	1768	K	R_d	0.5	mm

Governing Equations

The coordinate system (x, y, z) is shown in the Fig. 2. The workpiece bottom surface is used to define the x-y plane and the torch travels along the x-axis. A three-dimensional transient model was developed to analyze the heat transfer and fluid flow for the GMA welding process. The computation domain was established to include the interaction of the metal droplets with the weld pool. A moving arc and a fixed coordinate system were adopted for solving the transient problem. The metal droplets were generated as source term in the computation domain. It is assumed that spherical droplets at certain height transfer into weld pool. The droplets carry mass, momentum, and thermal energy, and periodically impinge into the weld pool. The initial temperature of the droplet is assumed to be constant. The droplet is also given an initial transfer speed, together with a horizontal speed with the welding torch. Once a droplet reaches the weld pool surface, the droplet interacts with weld pool by transferring mass, momentum, and energy.

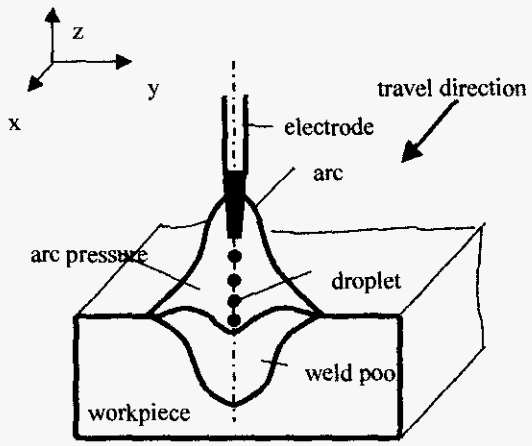

Fig. 2 — Schematic sketch of GMA welding

The governing equations, including continuity, momentum, and energy equations, are discretized using the control volume method. The regular rectangle meshes are used in the whole domain. Convection, radiation, and evaporation are incorporated as thermal boundary conditions. Both droplet travel speed and arc pressure are involved to determine fluid flow field and free surfaces. Furthermore, latent heat of fusion and evaporation are considered in the model. The heat transfer and fluid flow were calculated by numerical solution of the equations of conservation of mass, momentum, and energy in three-dimensional form. The governing equations for the model are given by Equations (1) to (3). The mathematical equations provided are valid for whole computation domain, which includes droplet, weld pool, and base material. The meaning of symbols in the equations (1) to (6) is listed in Appendix A.

Mass continuity equation:

$$\nabla \cdot \vec{V} = 0 \tag{1}$$

Momentum equation:

$$\frac{\partial \vec{V}}{\partial t} + (\vec{V} \cdot \nabla)\vec{V} = \frac{1}{\rho}(\nabla p + \mu \nabla^2 \vec{V} + F_b) \tag{2}$$

Energy equation:

$$\frac{1}{\rho}\left(\frac{\partial h}{\partial t} + (\vec{V} \cdot \nabla)h\right) = \nabla \cdot (K \nabla T) \tag{3}$$

where

$$h = C_p \cdot T + f \cdot L$$

$$f(T) = \begin{cases} 0, \text{if } T \le T_s \\ \dfrac{T - T_s}{T_l - T_s}, \text{if } T_s < T < T_l \\ 1, T \ge T_l \end{cases} \tag{4}$$

The body force is calculated using the electromagnetic and buoyancy forces:

$$F_b = \vec{J} \times \vec{B} - \rho\beta\vec{g}(T - T_m) \tag{5}$$

Arc pressure is determined using the following formula:

$$P_{arc}(x,y) = \frac{\mu_0 I^2}{4\pi^2 \sigma_j^2} \exp\left(-\frac{r^2}{2\sigma_j^2}\right) \quad (6)$$

It should be pointed out that the arc pressure in equation (6) is adopted from the GTA arc welding process due to lack of arc pressure expression for GMA arc.

III.1.1.2.B: Numerical Method

The developed weld thermo-fluid model in this research used the software package FLOW-3D (Ref. 1) as the solver of the heat transfer and fluid flow in the weld pool. The selected solver has the capability of modeling fluid flow with free surface, which is a must to predict non-flat weld bead shape. A unique technique called the FAVOR (Fractional-Area-Volume-Obstacle-Representation) method is used to define general geometric regions within the rectangular grid. Its free girding feature eliminates the tedious tasks of generating body fitted or finite-element grids. Furthermore, this feature makes it possible to simulate the dynamic weld pool with free surface within a reasonable computation time frame. The flow region is subdivided into a mesh of fixed rectangular cells. With each cell there are associated local average values of all dependent variables. All variables are located at the centers of the cells except for velocities, which are located at the cell faces (staggered grid arrangement). Curved weld surfaces (both molten and solidified) and other geometry features are embedded in the mesh by defining the fractional face areas and fractional volumes of the cells that are open to flow (Ref. 2). To construct discrete numerical approximations to the governing equations, control volumes are defined surrounding each dependent variable location.

III.1.1.2.C: Model Test and Validation

Three cases were analyzed in the study, which include bead-on-plate, horizontal-vertical T-joint, and T-joint with 45 degree. The welding parameters and work piece geometry are given in Table 2. Other parameters and constants for simulation have been listed in Table 1.

Table 2 — Experimental Conditions

Material	A36 steel	Wire feed rate	137.6 mm/sec
Thickness	12.7mm	Welding current	280 A
Length×width	6000mm×1000mm	Welding voltage	30 V
Wire diameter	1.32mm	Welding speed	5mm/sec

Bead-on-plate

The calculated temperature distribution and fluid flow field at different sections and at different moments for the bead-on-plate case are displayed in the Figs 3-5. The dark color at the middle indicates above-melting temperature, and the small arrows inside the weld pool represent molten material flow direction and magnitude. It can be seen that the weld pool penetration is developed gradually as welding time increases. As droplets enter the weld pool, both deep pool surface depression under the arc and high elevation away from the arc are clearly observed. The deposit material forms big weld reinforcement behind the welding torch.

In the longitudinal central cross section in Fig.3, the three figures on the left side show temperature and fluid flow fields, and the three figures on the right show enlarged local views of their counter parts from the left side. It is seen that the weld pool depth does not change much after 3 seconds, which means majority of penetration happens in the first 3 seconds since the high speed droplets penetrate the pool so quick that this kind of penetration reaches equilibration after 3 second between the pool and droplets. As for fluid flow inside the weld pool, the Fig.3 (left side) shows a complex flow pattern in the weld pool. There exist two flow loops at the longitudinal cross section at all the three moments. The big radially inward flow loop is dominated by the high-speed droplets and electromagnetic force. This is the driving force for GMA to form a deeply penetrated weld. The small radially outward flow loop behind the former one is driven by the surface tension gradient, and it makes the weld pool longer.

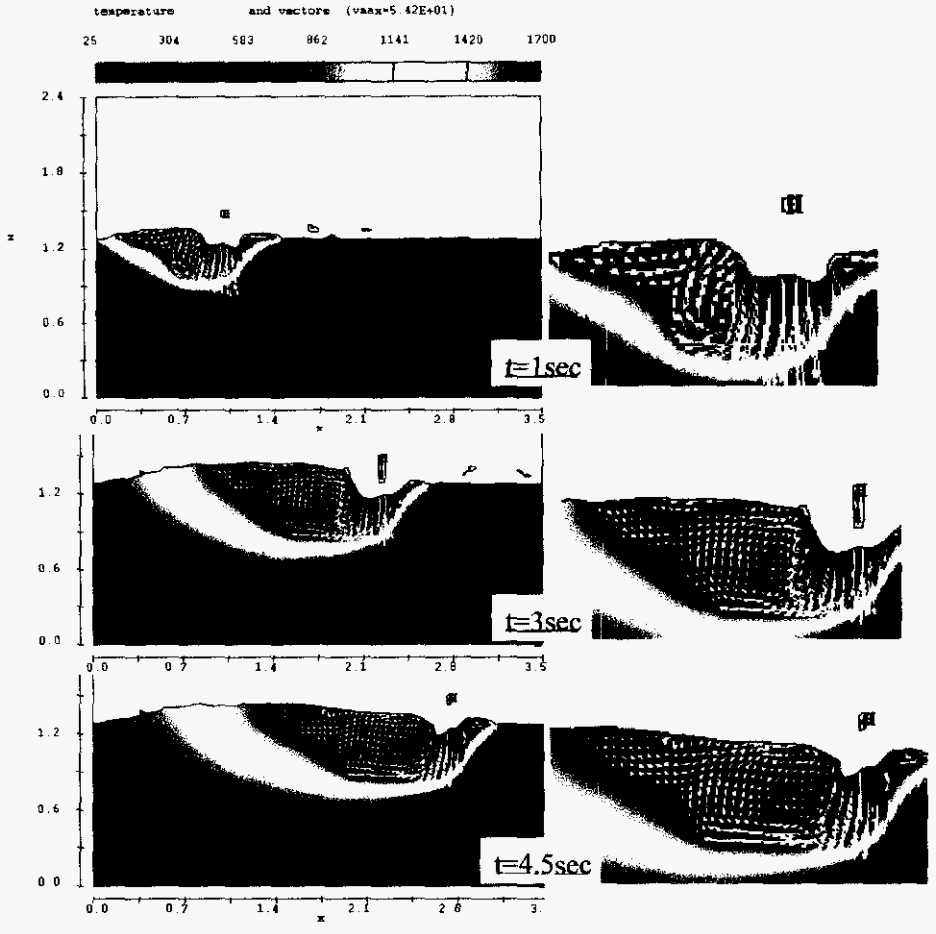

Fig. 3 — Temperature and fluid flow field at longitudinal cross section at different moments for bead-on-plate case.

In order to capture the temperature and fluid flow features at the top view, results at the two cross sections (A-A is z=12.5mm for the left three figures, and B-B is z=12.9mm for the right three ones) are plotted in the Fig. 4. Since the plate thickness is 12.7mm, only weld reinforcement is sectioned at B-B. From the top view, the weld pool is elliptical at the beginning, and then it gradually becomes a teardrop shape, due to the small radially outward flow loop mentioned at the longitudinal cross section. Also, it is because the part of weld pool behind the torch still holds higher than melting temperature, and the part of weld pool directly under the torch is continuously heated. This type of teardrop shaped weld pool was observed by Kou (Ref. 3) for high heat input and high travel speed. Also, it can be seen that there are two small flow loops behind the arc near fusion line. They are caused by the strong backward flow, and are contributing to enlarging the weld width.

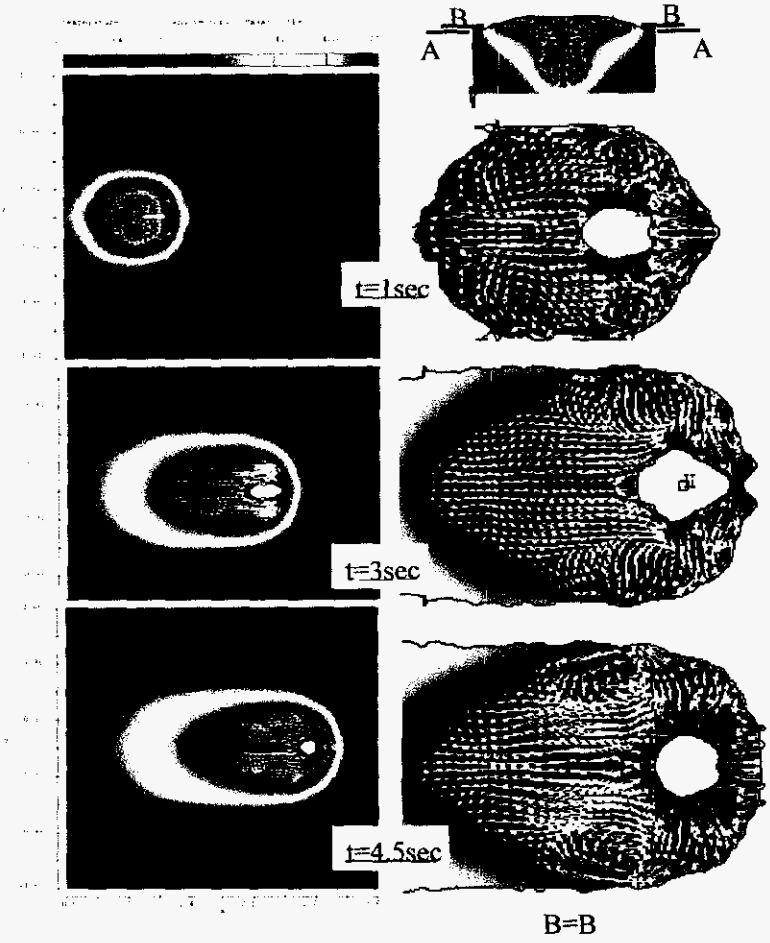

Fig. 4 — Temperature and fluid flow field at z = 1.25 cross section at different moments for bead-on-plate case

From the transverse cross section in Fig.5, it is found that the deepest penetration occurs at the section when arc reaches the surface. Reinforcement forms after arc passes. Fluid at the cross section when t=2.5 seconds flows downward at center driven by droplet flow, and flows outward driven by surface tension gradient. This trend can be observed more clearly at the cross section when t=3.1 seconds. Deep inside the pool, there are two downward flow loops, which produces deep and finger-like penetration. Near the pool surface, there are tow outward flow loops, which generate wide pool width.

Weld penetration is primarily determined by the droplet impact force, while weld width is determined by surface tension gradient force. Compared to metal droplet impact force, the effect of electromagnetic force on weld penetration is much less under the investigated GMA welding condition. The finger-like penetration occurs in GMA welding is caused by the combination of the droplet impact force, surface tension gradient, and electromagnetic force.

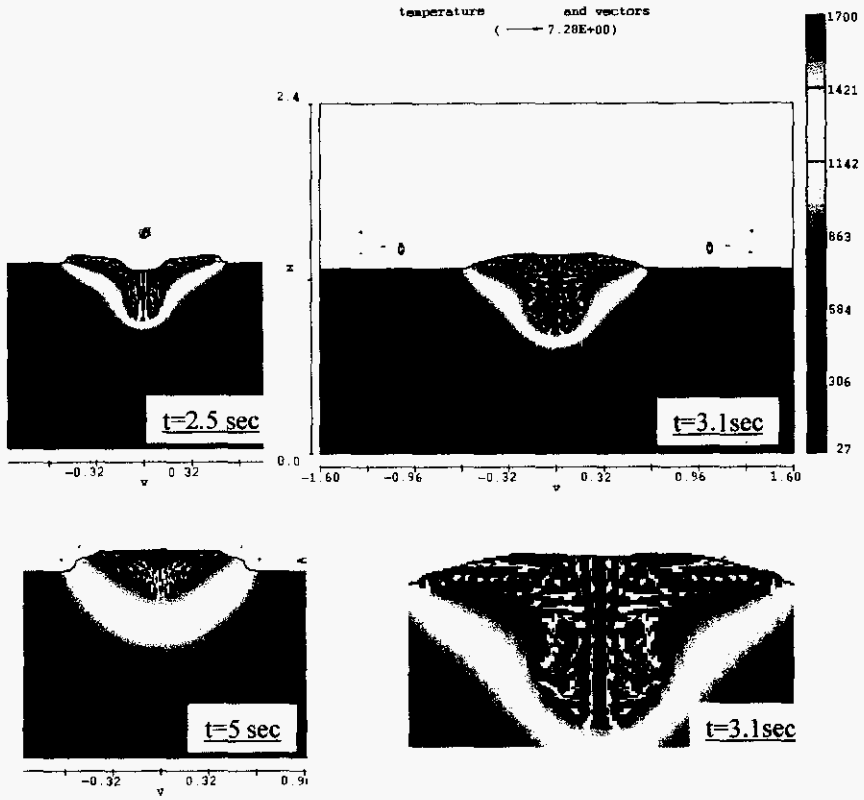

Fig. 5 — Temperature and fluid flow field at transverse cross section at different moments for bead-on-plate case

Horizontal-Vertical T-Joint

Unlike the bead-on-plate cases, there are both horizontal and vertical plates, and the arc torch has a 45-degree with respect to the horizon. In order to compare the joint type effects, all the calculation parameters used are the same as in the bead-on-plate case.

The calculated temperature distribution and fluid flow field at transverse cross sections and at different moments are displayed in the Fig. 6. The arc center is located at the cross section when t=2.5 seconds. As shown in Figure 6(a), finger-like penetration still occurs for this case due to the combination of droplet impact force and electromagnetic force. The maximum velocity at this moment is 53.9 mm/s, which is a little bit larger than the specified velocity of metal droplet. When the arc moves away from this location, as shown in Fig. 6(b), the maximum velocity decreased to 7.29 mm/s. This is because surface tension gradient force at this moment is dominant at this location. Thus, the fluid near the pool surface flows from the center outward. In addition, more fluid is formed near the horizontal plate due to gravity. As a result, the leg length of the weld on the horizontal side is larger than that on the vertical side. The predicted final weld bead shape after solidification is shown in Fig. 6(c).

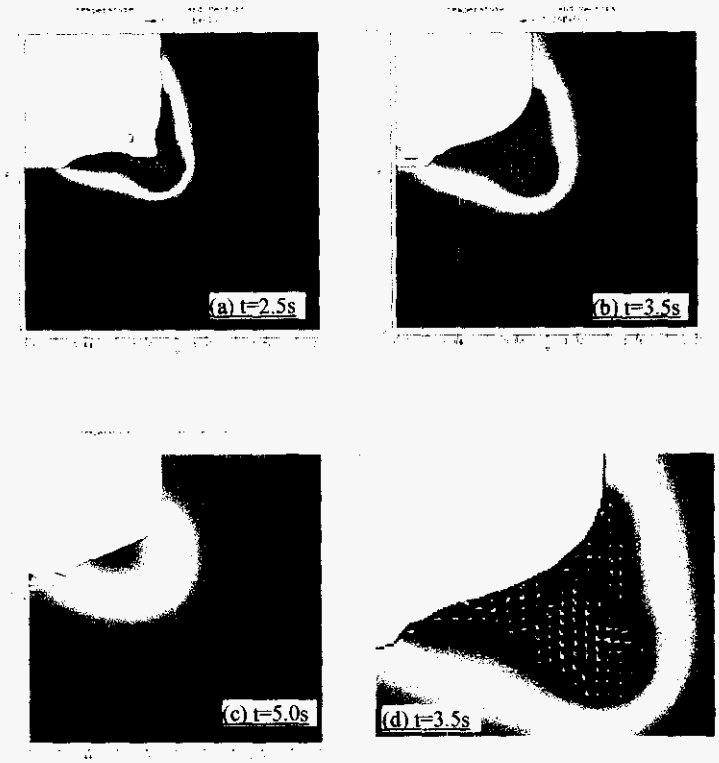

Fig. 6 — Temperature and fluid flow field at transverse cross section at different moments for horizontal T-fillet case.

The three-dimensional temperature distribution is shown in the Fig. 7. It can be observed that there is severe spatter at the beginning of the weld, and some spatter is located on the side of the weld on the horizontal plate. However, the situation is improved when time increases. Also, the weld bead shape can be observed clearly.

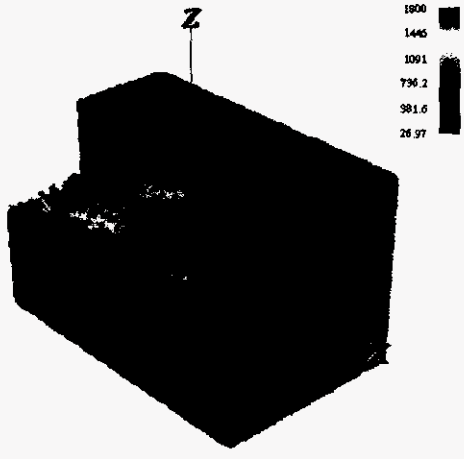

Fig. 7 — Three-dimensional temperature distribution for horizontal T-fillet case

T-JOINT WITH 45 DEGREE

In this case, the horizontal-vertical T-joint structure from the last case is rotated 45 degree around the x-axis, so that the weld torch is located at the vertical position and it has the same angles (45 degree) to the two plates. The calculated temperature distribution and fluid flow field at longitudinal and transverse cross sections and at different

moments are displayed in Fig. 8. There is much splatter in the torch travel direction, and less splatter along the side of weld, which is due to its special joint position.

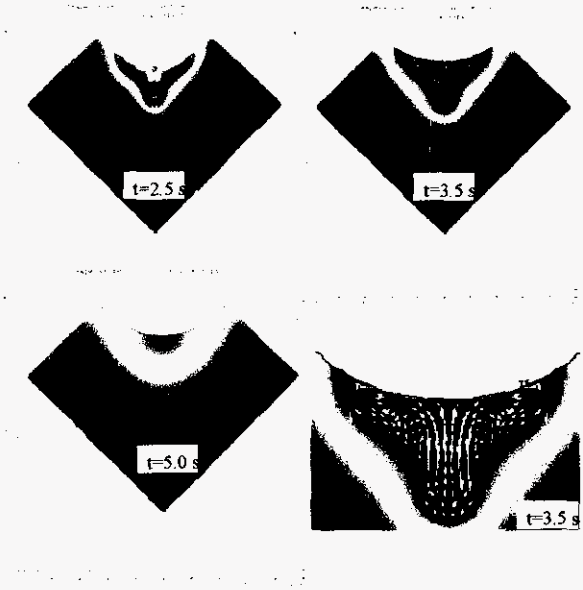

Fig. 8 — Temperature and fluid flow field at transverse cross section at different moments for 45 degree T-joint case

VALIDATION

To validate the modeling results, GMA welding experiments were carried out for both bead-on-plate and T-fillet welds. The test conditions are listed in the Table 2. Comparison between the calculated and actual welds bead shape for both bead-on-plate and T-fillet welds is shown in Figure 9. It can be seen that the predicted weld width and depth are close to experimental ones in both cases. In bead-on-plate case, the predicted width and depth are 1.24mm and 0.39mm, and the measured width and depth are 1.29mm and 0.41mm. Also, the finger-like penetration is captured from the prediction, and its penetration shape matches the experimental one well. In T-fillet weld case, the concave weld bead shape was well predicted from simulation. As shown in Figure 9(b), the predicted penetration and weld toe radius are comparable with the actual weld geometry.

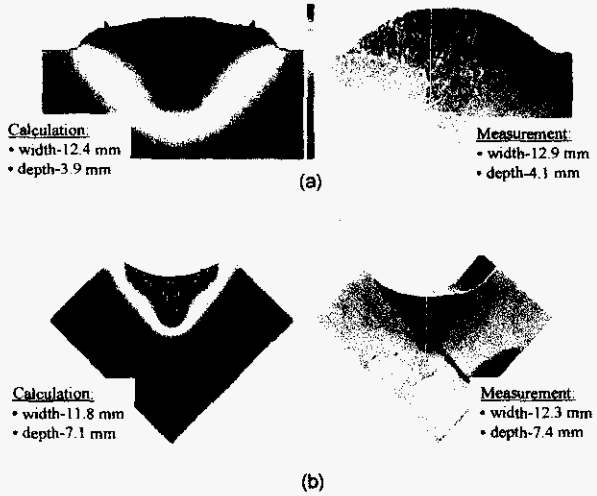

Fig. 9 — Weld profile comparison between calculation and measurement for (a) bead-on-plate and (b) 45 degree T-fillet weld.

The present weld thermo-fluid model represents the leading position in this research area due to its unique capacity in simulation of the free surface of weld pool and the detailed features of the interaction of metal droplets with the weld pool. Based on Weld Thermo-Fluid model, the weld bead shape can be predicted based on the input parameters such as heat input, torch angle, and material properties. The model has been applied for weld bead shape prediction in different types of welded-joints including butt welds, T-fillet welds, and plug welds. Fig. 10 shows the comparison of the predicted and actual weld bead shapes as well as predicted weld defects. The good agreement between the simulated and actual results indicates significant promise to optimize welding parameters and materials for desired weld bead shape based on the simulation results.

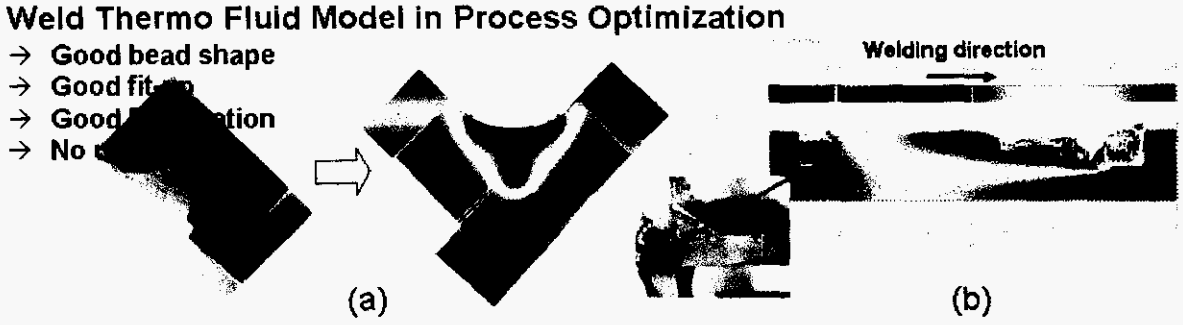

Fig. 10: (a) Comparison of simulated and actual welds bead shape in T-fillet weld and (b) Comparison of predicted and actual weld defect.

III.1.1.3: Quasi-steady state Weld Pool Simulation

A quasi-steady state three-dimensional heat transfer and fluid flow model considering the weld pool free surface deformation and the additional heat from the metal droplets was developed at Penn State to calculate temperature and velocity fields and solidified surface profile for gas metal arc (GMA) fillet welding [16]. The numerical model solves the continuity, momentum conservation and energy conservation equations in a boundary fitted coordinate system. The governing equations of conservation of mass, momentum, and energy and their corresponding boundary conditions were similar to those in the previous transient model. At Penn State's model, the transformed equations were discretized using control volume method and then solved using a modified SIMPLE algorithm. The free surface profile was calculated by minimizing the total free surface energy considering the addition of filler metal. The additional heat from the metal droplets was modeled considering the available knowledge base of the interaction between metal droplets and the weld pool for various welding conditions.

The fillet model has been well tested to be quite efficient and stable. For a typical grid system of 53 × 66 × 47, the calculation can converge in 3900 iterations and it takes only about 17 minutes in the server with Pentium IV 2.53 GHz CPU and 512 DDR-SDRAM memory.

III.1.1.3.A: Heat transfer and fluid flow in the fillet weld

The calculated temperature and velocity fields for case #2 in Table 3 are shown in Fig. 11. As shown in this figure, the liquid metal motion is quite complicated due to the combined effect of the three driving forces. The liquid metal is mainly driven by the electromagnetic and surface tension gradient forces and to a much less extent by the surface tension force. In the middle of the weld pool, the liquid metal is driven downwards by the electromagnetic force, and a major anticlockwise circulation.

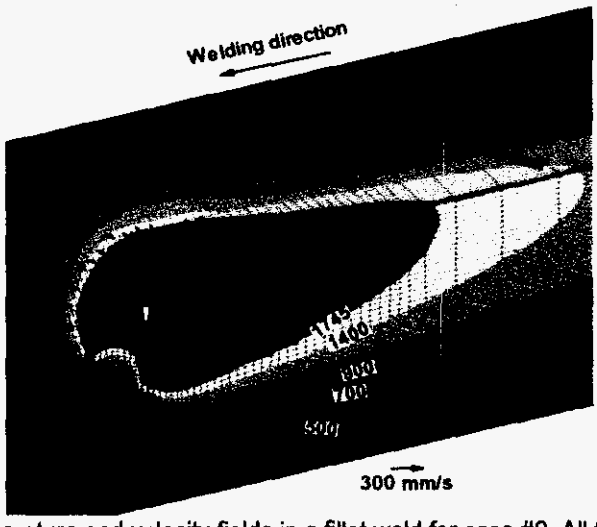

Figure 11: Calculated 3D temperature and velocity fields in a fillet weld for case #2. All the temperatures are given in Kelvin. The white arrow in the middle of the weld pool indicates the location of the heat source. The weld pool boundary is represented by the 1745 K isothermal line.

Loop is formed along the central longitudinal plane. On the other hand, at the top surface of the weld pool, the Marangoni shear stress drives the melt from the center to the edge of the pool in the region close to the heat source, where the spatial variation of the surface temperature is relatively high. In the rear part of the weld pool, where the temperature gradient is relatively low, the effect of Marangoni shear stress is less strong than that of electromagnetic force. As a result, the liquid metal flows inward in the rear part of the pool.

III.1.1.3.B: Model verification

Numerical calculations were carried out to validate the fillet heat transfer and fluid flow model for various welding conditions. The welding parameters are summarized in Table 3. Figure 12 shows the calculated weld bead shape for all the four cases listed in Table 3. As shown in this figure, the calculated weld bead geometry for all cases agrees reasonably well with the corresponding experimental results. In particular, the shape of the weld reinforcement and the finger penetration could be satisfactorily predicted by the model. It should be noted that some discrepancy between the experimental bead profile and the computed results are observed in Fig. 12. Part of this discrepancy is contributed by the thermal stress induced distortion, as can be evidenced by the gap between the two originally perpendicular plates.

Table 3. Welding conditions used in the fillet welding experiments.

Case No.	Contact tube to workpiece distance (CTWD) (mm)	Wire feeding rate (mm/s)	Travel speed (mm/s)	Voltage (V)	Current (A)
1	22.2	169.3	4.2	31	312.0
2	22.2	211.7	4.2	33	362.0
3	28.6	169.3	4.2	33	286.8
4	28.6	211.7	4.2	31	331.4

Joint type: fillet joint, flat position, 90 degree joint angle, and no root gap
Base metal: ASTM A-36 mild steel.

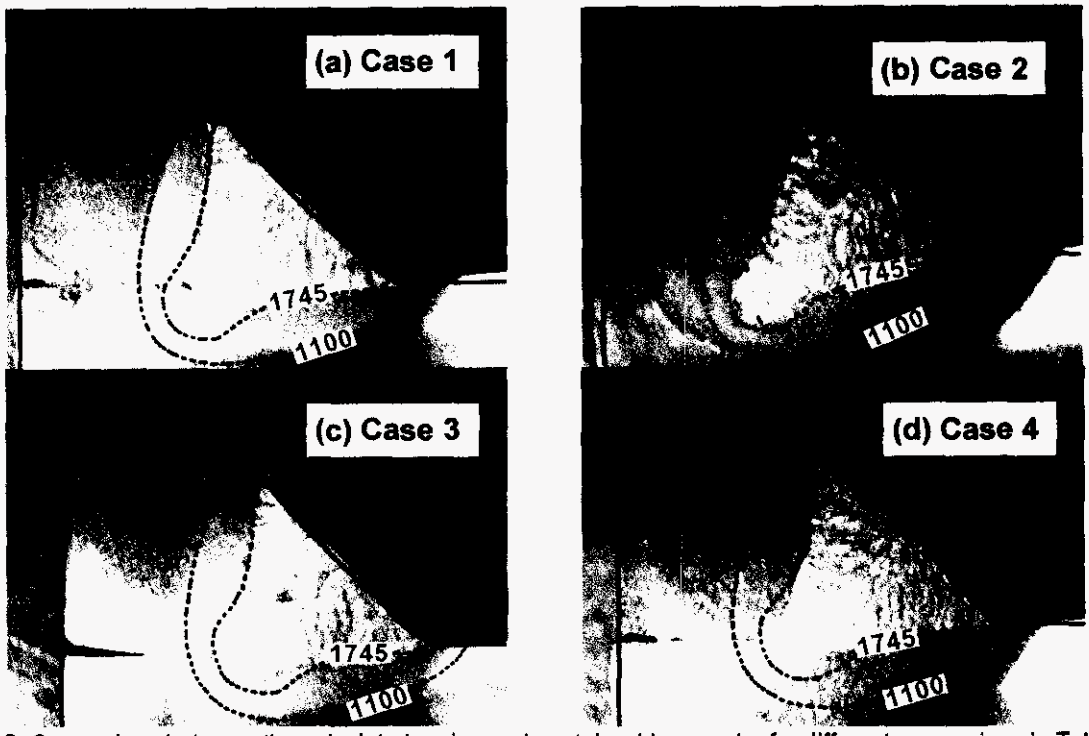

Figure12: Comparison between the calculated and experimental weld geometry for different cases given in Table 3. The 1745 K solidus isotherm represents the calculated weld pool boundary.

III.1.1.4: Summary of Weld Thermo-Fluid Models

A 3D transient thermo-fluid model with free surface and a 3D quasi-steady state thermo-fluid model were developed to simulate the heat transfer and fluid flow in GMA weld pool. The models have been used to analyze the heat transfer and fluid flow pattern for different types of welded-joints including bead-on-plate and T-fillet joints. The predicted weld bead shapes were compared with experimental results.

The following conclusions can be made from the 3D transient thermo-fluid model:

1. The 3D transient free surface model can simulate the details for the weld pool formation during GMA welding process. This includes the melting of base material, the interaction of metal droplet with weld pool, weld pool solidification, and the final weld bead shape.

2. The flow pattern in GMA welding process can be well predicted by considering the combined forces from metal droplet impact, surface tension gradient, electromagnetic force, arc pressure, and gravity. Among all of the forces, the metal droplet impact is the primary force responsible for penetration, which in combination with the outward flow on the pool surface driven by tension gradient force causes the finger penetration in GMA welds.

3. The 3D free surface model is capable of simulating heat transfer and fluid flow in various types of welds. The detailed features for GMA welds such as finger penetration, reinforcement due to wire deposition, and weld toe can be modeled. Good agreement was observed between the predicted and actual welds.

The results from the quasi-steady state weld heat transfer and fluid flow model can be summarized as:

The model was developed to calculate the temperature profiles, velocity field, weld pool shape and size and the nature of the solidified weld pool reinforcement surface during GMA welding of fillet joints. The numerical model

solves the continuity, momentum conservation and energy conservation equations in a boundary fitted coordinate system. The driving forces for liquid metal convection in the weld pool include surface tension, buoyancy and electromagnetic forces. The heat transfer from metal droplets was simulated using a volumetric heat source. The weld pool surface profile was calculated by minimizing the total surface energy, which includes the surface tension energy, gravity potential, work done by arc force.

The numerically computed fusion zone geometry, finger penetration characteristic of the GMA welds, the solidified surface profile of the weld reinforcement and cooling rates were in fair agreement with the experimental results for various welding conditions. The numerical model allows efficient solution of the temperature and velocity fields in a complex physical domain containing a deformable free surface.

III.1.2: Microstructure Model

III.1.2.1: Background of Weld Microstructure Model

Modeling of steel weldment microstructure requires understanding of the phase transformation kinetics and the thermal cycles in the material. The thermal cycles can be obtained from reliable mathematical models by comprehensive modeling of heat transfer and fluid flow during welding, which has been discussed in the previous section. In recent years, several phase transformation models have been developed for modeling microstructure in steel welds and HAZ. Coupling these phase transformation models with the calculated thermal cycles from a reliable thermal model is essential for quantitative understanding of steel weldment microstructure.

The phase transformation model developed by H.K.D.H. Bhadeshia et al. [Ref. 4] was adopted due to its robust capability in prediction of welding induced phase transformations from first principles of transformation thermodynamics and kinetics. The model has been refined and tested in the past decade for its capability to quantitatively predict phase volume fractions in weld zone as functions of chemistry and heat input. Bhadeshia's model was originally developed to predict the microstructure in the weld zone. To apply the model to predict the microstructure in HAZ, the thermal cycles at various locations in the HAZ needs to be calculated from the weld thermal model. In addition, grain growth in the weld HAZ needs to be incorporated in the available phase transformation model. The thermal cycles were first used to calculate grain growth in the HAZ. The grain growth in the weld HAZ was simulated based on grain growth kinetics. After that, the prior austenite grain size and thermal cycles were used as inputs for the following calculation of the decomposition of austenite to its daughter phases (ferrite, bainite, or martensite).

III.1.2.2: Model Description

The microstructural evolution in the weld metal of low alloy steel is schematically shown in Fig. 13. The final weld metal microstructure is dominantly determined by the austenite decomposition process within the temperature range from 1073 to 773 K. During cooling of the weld metal, allotriomorphic ferrite is the first phase to form from the decomposition of austenite in low alloy steels. It nucleates at the austenite grain boundaries and grows by a diffusional mechanism. As the temperature decreases, diffusion becomes sluggish and displacive transformation is kinetically favored. At relatively low undercoolings, plates of Widmanstatten ferrite forms by a displacive mechanism. At further undercoolings, bainite nucleates by the same mechanism as Widmanstatten ferrite and grows in the form of sheaves of small platelets. Acicular ferrite nucleates intragranularly at inclusions and is assumed to grow by the same mechanism as bainite in the present model. The morphology of acicular ferrite differs from that of conventional bainite because the former nucleates intragranularly at inclusions and within large austenite grains, while the latter nucleates initially at austenite grain boundaries and grows by the repeated formation of subunits to generate the classical sheaf morphology.

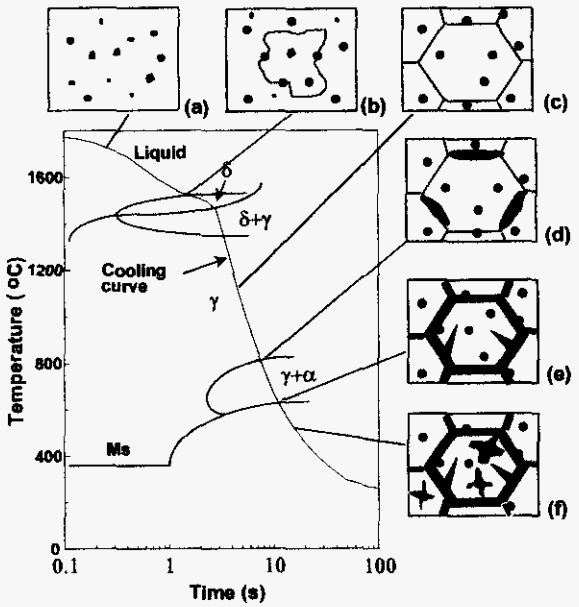

Figure 13: Schematic diagram for microstructrural evolution in steel welds.

III.1.2.3: Model Assumption

An important assumption in the model is that "Paraequilibrium" assumed in the calculation of phase transformations. "Paraequilibrium" is a constrained phase equilibrium when a phase change is so rapid that one or more components cannot redistribute within the phase in the available time scale. For transformation in steels, the diffusion coefficients of substitutional and interstitial components differ significantly. It is possible that the sluggish substitutional alloying elements may not have sufficient time to redistribute during the transformation of austenite to ferrite under some circumstances, even though carbon may partition into austenite. In the model, "paraequilibrium" is assumed at the III boundary. Under the "paraequilibrium" condition, the substitutional solute/iron atom ratio remains constant everywhere. Since carbon is a fast diffusing species in iron, it can partition to an extent which allows it to achieve local (para) equilibrium at the interface.

Considering the rapid cooling rates involved, it is reasonable to assume paraequilibrium in the weld metal under welding condition. Under this assumption, the carbon concentration in austenite ($x^{\gamma\alpha}$) and that in the ferrite ($x^{\alpha\gamma}$) at the interface can be determined from a calculated multicomponent phase diagram. Then the diffusion-controlled growth rate for ferrite can be calculated using the theory relevant to Fe-C alloys by substituting the carbon concentrations in austenite ($x^{\gamma\alpha}$) and that in the ferrite ($x^{\alpha\gamma}$) at the interface.

III.1.2.4: Model Validation

The weld microstructure model has been well tested for microstructure prediction in fusion zone (Ref. 4) for low alloy steels. After the model was modified, it was extended to predict microstructure in both weld fusion zone and HAZ in this project. Fig. 14 shows the spatial distribution of phase volume fractions in the weld zone and its HAZ. The weld composition is (wt. %): 0.095 C, 1.05 Mn, 0.32 Si and heat input is 1.0 kJ/mm. The phase volume fractions are calculated as functions of chemistry and cooling rates. Four phases were predicted in the investigated weld samples. It can be observed that the volume fractions of phases in weld zone are constant but the quantities varied significantly in the weld HAZ. This is because the prior austenite grain size and cooling rates within austenite decomposition range (800°C ~ 500°C) at all locations in weld zone are almost the same. However, the prior austenite grain size varied significantly in weld HAZ. In addition, the cooling rates are quite different at various locations in the HAZ. More low temperature austenite daughter phases (Acicular ferrite, bainite, and Martensite) were observed at the locations near fusion line than those near the base material region. In contrast, less high temperature austenite daughter phases (grain boundary ferrite and Widmanstatten ferrite) were observed at the locations near fusion line.

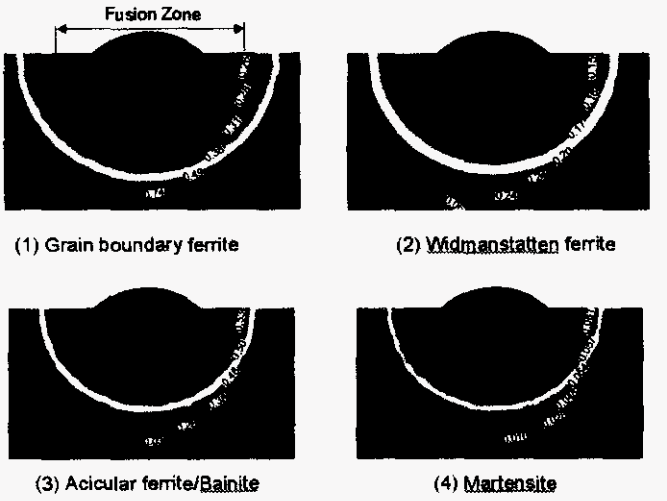

Fig. 14: Spatial distribution of various phases in weld zone and HAZ.

Fig. 15 shows the comparison of experimental microstructure [Ref. 5] and calculated results for phase volume fractions in weld zone. It is observed that the predicted weld microstructures are comparable with experimental results for all of the welds with different chemistry.

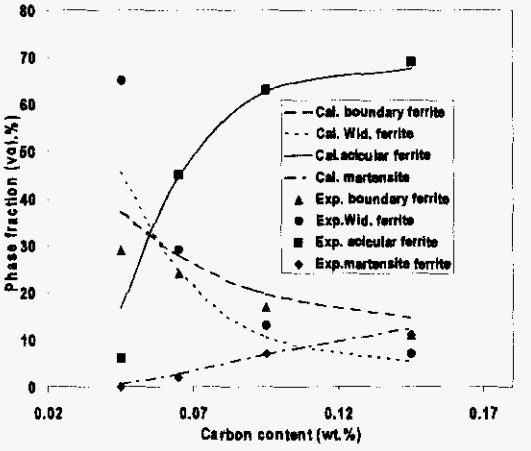

Fig. 15: Comparison of predicted and experimental microstructure.

The developed weld microstructure model is able to quantitatively calculate the prior austenite grain growth and the volume fractions of various phases (austenite, ferrite, bainite, and martensite) as functions of chemistry and heat inputs. The bottom left picture in Figure 6 shows a predicted bainite phase distribution map in a weldment, in which the value of bainite phase at each location can be identified in the contours. Similar maps are also available for other phases. The corresponding calculated hardness map is shown in the bottom right picture in Figure 6. This is an under-matched weld.

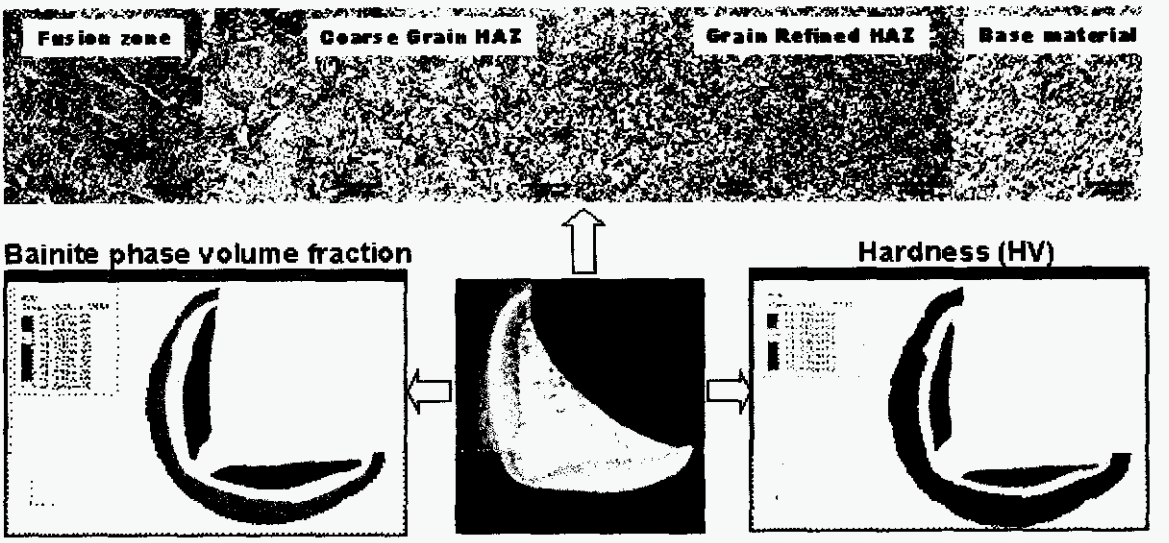

Figure 16. Comparison of actual and predicted spatially distributed microstructure and hardness.

III.1.3: Weld Material Property Model

III.1.3.1: Background on Weld Property Model

In recent years, extensive effort has been made in the prediction of weld material properties (hardness, yield strength, and toughness) based on metallurgical modeling. Various models are now available for quantitative prediction of weld material properties based on empirical equations. However, the empirical equations cannot predict the local material property at each point in a weld, which is dependent on the microstructure and thermal cycle at that location.

Some initial work has been made to predict the spatial variation of weld material property by combining the thermal cycles from thermal analysis and microstructure modeling. From FEA thermal analysis, the heating and cooling rates at each material point can be obtained. The microstructure at each material point at various temperatures can be effectively predicted by microstructure modeling. The spatial distribution of weld material property was then predicted based on the calculated microstructure using mixing law.

Table 4 shows the variation of predicted yield strength as functions of chemistry. It can be observed that the yield strength increases accordingly with the increasing of carbon content. As stated previously, the material property at each location was calculated based on the microstructure at that location. The mixing law was used for quantitative calculation of the yield strength of the material with various phases. The closer to fusion boundary, the larger the amount of bainite and martensite. As a result, higher yield strength is expected at locations near the fusion line than those near the base metal. The predicted yield strength from this approach is comparable with the experimental data. The comparison of predicted and experimental determined yield strength in weld zone for four welds is given in Table 4.

Table 4: Comparison of experimental [Ref.5] and calculated strength.

	Yield Strength (MPa)	
Carbon (wt. %)	Experimental	Calculated
0.045	435	431
0.065	450	437
0.095	470	460
0.145	511	487

III.1.3.2: Determination of Stress-Strain Curves Using Gleeble

The residual stress resulting from welding process is determined by the plastic deformation at elevated temperatures. The true stress-strain curves are the prerequisite for welding residual stress analysis. One of the task in this project is to determine the true stress-strain curves of two steels at elevated temperatures using Gleeble thermal-mechanical simulator at ORNL. In this project, tensile tests were carried out on two steel samples A and B provided by Caterpillar, in which steel A is high strength steel and steel B is mild steel. The chemistry of the two steels is listed in table 5. Experimental data based models have been established to predict the stress-strain curves for the investigated two steels.

Table 5: Chemical compositions for steel A (HS) and steel B (MS)

Mat.	C	Mn	P	S	Si	Ni	Cr	Mo	Cu	Al	B	Ti	Zn	Nb	V
HS	0.19	1.24	0.012	0.006	0.33	0.01	0.15	0.04	0.01	0.045	0.0023	0.032	0.0	0.00	0.06
MS	0.06	0.90	0.016	0.004	0.04	0.01	0.02	0.01	0.02	0.032	0.0000	0.002	0.0	0.01	0.00

To investigate the effects of microstructure on stress-strain curves, the steels were tested under two conditions. In the first set of experiments, the steels were heated to austenitizing temperature (1200°C) and held for 5 minutes. Then the samples were cooled at 20°C/s to different temperatures and were subjected to tensile tests. These isothermal tests were performed at 40, 100, 200, 300, 400, 500, 600, 700, and 800 °C. During testing, the transformation characteristics were also measured in these samples. In the second set of experiments, the steels were heated to test temperatures without austenitizing and were subjected to tensile tests. The isothermal test temperatures were 25, 100, 200, 300, 400, 500, 600, 700, and 800°C. The motivation behind this research is to compare the response of steel to loads during weld heating and weld cooling conditions.

III.1.3.2.A: Gleeble Test Results:

Transformation Characteristics

The dilatation measurements from the steel A and B are compared in Fig. 17. The data showed that Steel A has higher hardenability than that of Steel B. It was found out the in steel A, the tensile tests at 500°C may overlap with the transformation of austenite to bainitic ferrite. In case of steel B, for the same temperature, the austenite might have almost transformed to ferrite. This difference in transformation temperature and microstructure is expected to have significant effect on the stress-strain characteristics.

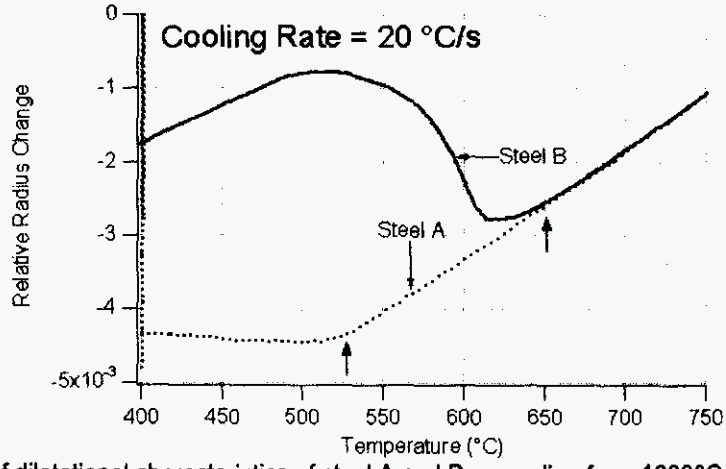

Fig. 17 Comparison of dilatational characteristics of steel A and B on cooling from 1200°C at a rate of 20 °C/s

Results from Steel A

The measured stress-strain characteristics from steel A during on-cooling experiments are shown in Fig. 18 and the data from on-heating experiments are shown in Fig. 19. The measurements in both cases show some stress-relaxation characteristics. This is attributed to the slow strain rate of ~0.01 s^{-1} used in the present studies. The comparison of stress-strain characteristics at 500°C during on heating and on cooling showed interesting features. On-cooling data shows lower yield strength and exhibits strain hardening over large strain values. In addition, there are distinct two hardening regimes. Such hardening behavior has been reported by Cottrell [17] during tensile testing of austenite while it decomposes to martensite. Similarly, in the steel A, the first strain hardening regimes may be attributed to austenite and the second one to the bainitic ferrite that forms from austenite.

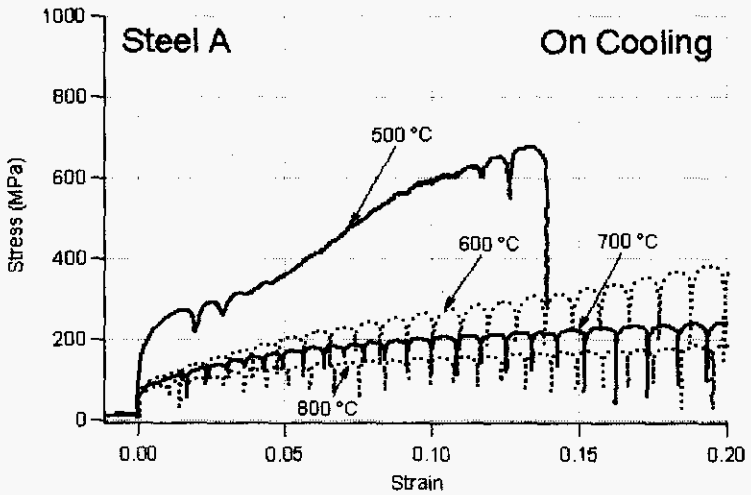

Fig. 18 Comparison of true stress-strain characteristics from steel A during on cooling experiments.

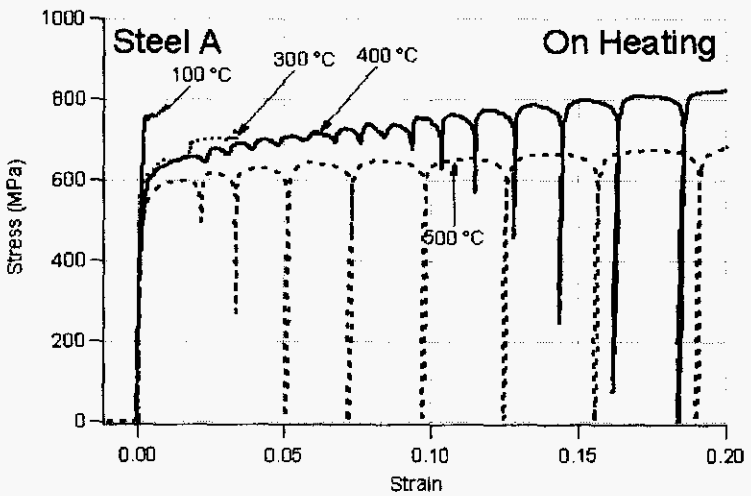

Fig. 19: Comparison of true stress-strain characteristics from steel A during on heating experiments.

Results from Steel B

The measured stress-strain characteristics from steel B during on-cooling experiments are shown in Fig. 20 and the data from on-heating experiments are shown in Fig. 21. The results showed that the measured stress-strain characteristics from on cooling and on heating experiment at 500°C showed only minor differences. The ultimate

tensile strength of on-cooling experiment was slightly above that of the on-heating experiment. However, the on-cooling data did not show two different hardening regions. It is important to note that at 500°C, the austenite in steel B is expected to have transformed to ferrite completely. Interestingly, the on cooling experiments at 600°C did not show the two hardening regions either. At this temperature, the steel B is expected to have a mixed microstructure of austenite and ferrite.

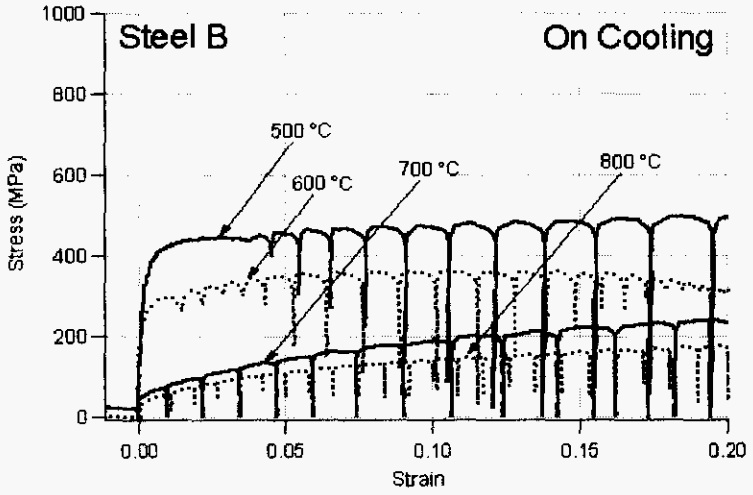

Fig. 20 Comparison of true stress-strain characteristics from steel B during on cooling experiments.

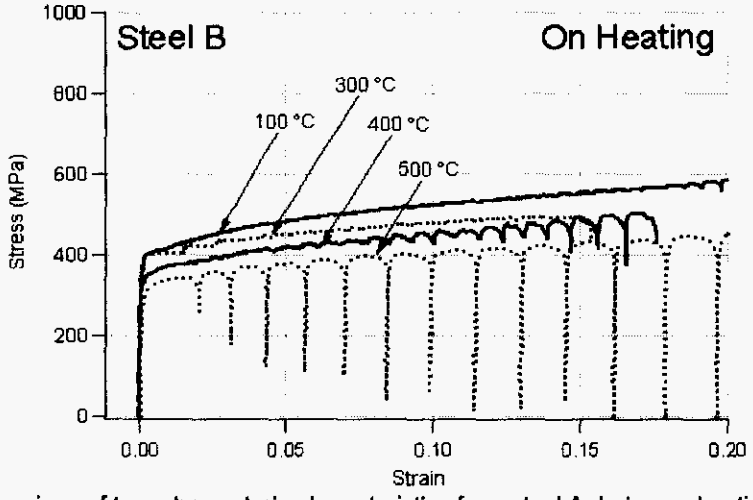

Fig. 21: Comparison of true stress-strain characteristics from steel A during on heating experiments.

Implications

The above results indicate that stress-strain characteristics of mixed microstructure of austenite and ferrite in high strength steel is expected to be significantly different from a mixed microstructure in low strength steel. This is related to complex interplay of hardenability and difference in flow characteristics of ferrite and austenite at different temperature. The present results also show that there is a possibility of substantial stress relaxation at slow strain rates.

III.1.3.2.B: Discussion of stress-strain curves

The stress-stain data from all the samples were analyzed further. Some of the elevated temperature tests done on both steel A and B showed some fluctuations of strain rates, although the average strain rate of the tests remained

constant. These fluctuations in strain rate also lead to changes in flow stress. Therefore, suitable models to predict the strain rate effects were explored. The hyperbolic sine function formulas have been used before to describe the strain rate effect in describing the flow stress of steel. The equation is given below.

$$\overset{o}{\varepsilon} = A\sinh(\alpha\sigma)^n \exp\left\{\frac{-Q}{RT}\right\} \tag{7}$$

In this equation, the strain rate ($\overset{o}{\varepsilon}$) is related to flow stress (σ), activation energy (Q), temperature (T), Gas constant (R), and some material specific parameters such as "α" and "n". Using non-linear fitting, these parameters were derived. The comparison of model predictions and the measured data at 393 K is shown the Fig. 22.

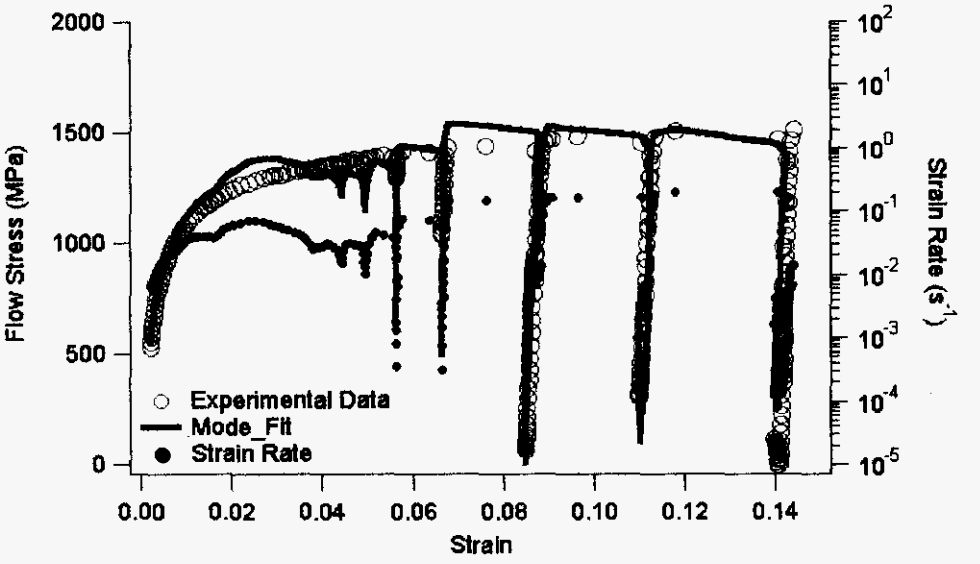

Fig. 22. Comparison of predicted flow stress by hyperbolic sine function model and the measured flow stress at 393 K from steel A. The model is able to predict the changes in flow stress in accordance with fluctuations in strain rate.

Based on the experimental data, a code has been developed to predict stress-strain curves for the two steels at various temperatures.

The material properties in weld fusion zone and HAZ vary with locations depending on the thermal cycles and chemistry. One of the major focuses in the weld material property model is to predict true stress-strain curves as functions of temperature and microstructure. True stress-strain curves at ambient and elevated temperatures are critical input data for simulation of weld residual stress. These stress-strain curves can be different for the same material at the same test temperature. Figure 23(a) shows the true stress-strain curves for two different steels (steel A-high strength steel and steel B-mild steel) tested at 500°C using Gleeble machine at Oak Ridge National Laboratory.

It can be observed that the stress-strain curves are quite different for the same material with different thermal cycles (e.g. on heating and on cooling). The difference results from the different microstructures, as shown in Figure 23(b), obtained under the test conditions of on heating and on cooling. The data from steel A (high strength steel) on cooling seems "abnormal" since the obtained values at the beginning, which correspond to the low strain data, are even much lower than the data for steel B (mild steel). Microstructure modeling can provide the detailed insight into this phenomenon. The calculated evolution of microstructure vs. time and temperature is shown in Figure 23(c). The volume fractions of various phases vs. time and temperature can well explain the stress-strain curve for steel A on cooling test. It can be observed austenite continues to decompose into bainite during the test period at 500°C. Thus, the yield stress for steel A during the

period of on cooling test keeps increasing as shown in Figure 23(a).

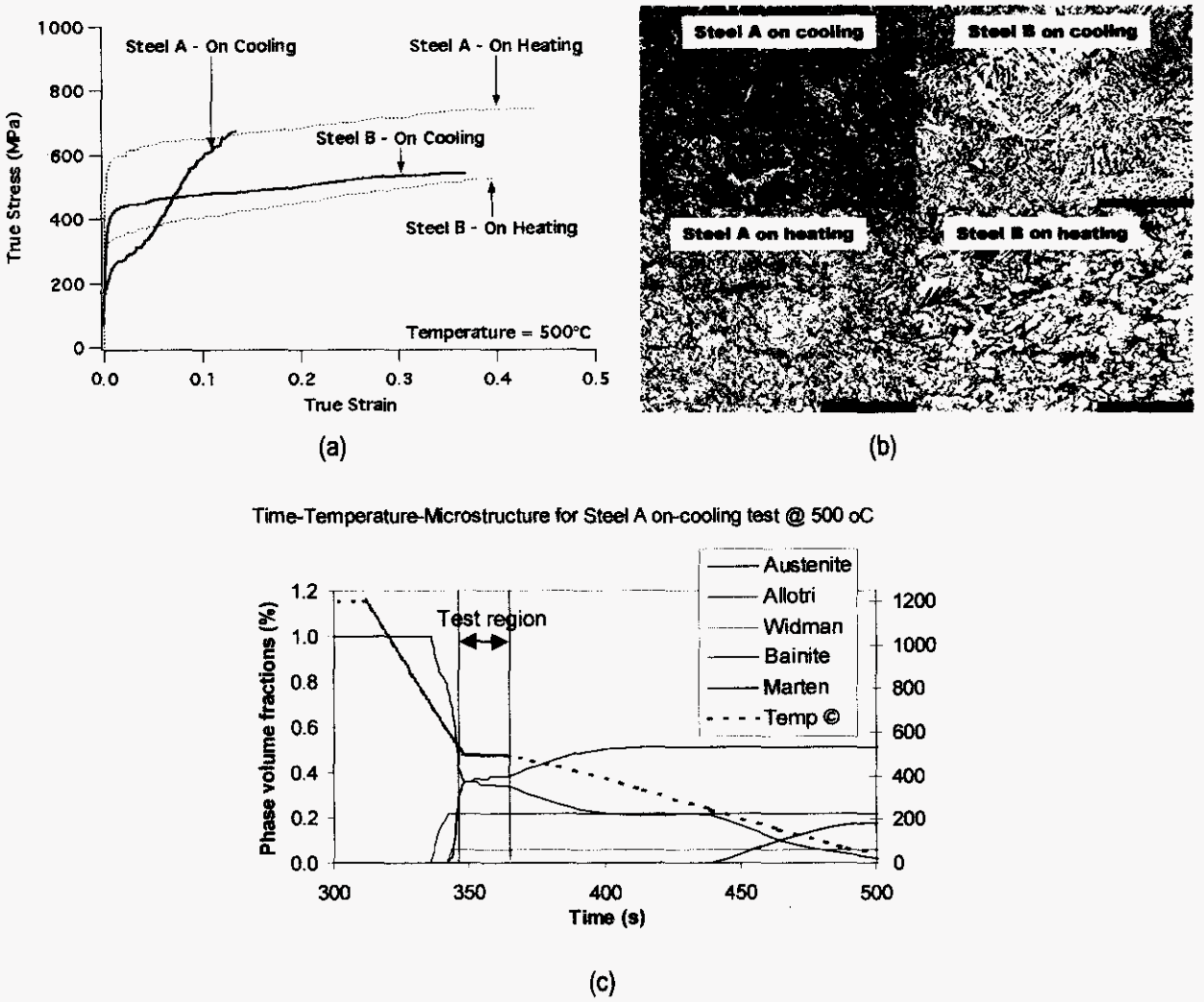

Figure 23: (a) True stress-strain curves from Gleeble test; (b) Microstructures obtained at different thermal cycles; and (c) Evolution of microstructure vs. time and temperature.

III.1.4: Weld Residual Stress Model

III.1.4.1: Background on Weld Residual Stress Model

The weld residual stress model was based on an existing weld structural model, which was developed by Battelle and Caterpillar over the past 8 years. The structural model was developed based on ABAQUS commercial finite element codes by implementing a special user materials subroutine-UMAT. UMAT is a user subroutine interface in ABAQUS that can be used to model user-specific material behavior. It allows the user to develop its own Fortran subroutine to interface with ABAQUS solver for user-specific material modeling. On one hand, it is a very powerful tool, virtually allowing for any kinds of material modeling that is not built in the ABAQUS material model library. On the other hand, however, it is a very complicated process, requiring the user not only to have a solid understanding of finite element theories, but also the skills and experience to implement a sophisticated material model as a UMAT plug-in.

UMAT-CAT [6] is such an implementation of material model developed by Battelle and Caterpilla Inc., specifically for the purpose of modeling material behavior during the welding process. It was initially developed during the FASIP program as part of the numerical modeling tools for arc welding process. Specific features of UMAT-CAT include (Ref. 6):

- Use field variables to trace temperature history and peak temperature at material points
- Use internal state variables to trace thermal and mechanical strain development
- Use internal state variables to trace yielding locus and yield surface evolution
- Model stress/strain history annihilation due to material melting/re-melting ("Annealing") and incorporate its effects into yield surface determination
- Implement a general nonlinear work hardening model
- Allow multiple material definitions (up to 10 different materials)
- Finite strain, large deformation considerations
- Incorporate virtual element detection (VED) to model continuous weld metal deposition associated with a moving arc
- Incorporate an initial stress self-equilibrating scheme to include pre-weld residual stress history

III.1.4.1: Model Description

The task in this project is to further enhance the existing UMAT-CAT capabilities by incorporating the effects of microstructural phase transformation effects on the material modeling. To do this, the following specific sub-tasks have been completed.

1.UFIELD Mapping – Develop an approach using UFIELD subroutine to accessing, interpolating, and passing external microstructure phase volume information into UMAT as field variables.
2.Theoretical Formulation of Phase Transformation Effects – Derive the constitutive formulation for the phase transformation process as related to the effects on the material's constitutive behavior.
3. Numerical Implementation and Coding – Implement the phase transformation model into the existing UMAT-CAT framework.
4. Testing and Verification – Validate the developed subroutine with weld simulation models.

The microstructural phase transformation during a welding process is a very complicated material phenomenon. There are many constitutive formulations proposed by a number of authors over the years in regard with how to theoretically describe the phenomenon and how to incorporate its effects into the constitutive law. In this project, the constitutive theory proposed by Fish et al. (Ref .7) is used for this work.

Our emphasis in UMAT-CAT development is for weld residual stress modeling. In order to capture the major impact of phase transformation on residual stress, the material model is further simplified. We have decided in UMAT-CAT 4.0 to only incorporate the phase transformation effects during the cooling phase of the welding process. This decision is based on the following major considerations:

- It is widely believed that the phase transformation occurred during the cooling phase (at relatively low temperature range) has the most impact on the final residual stresses, if there are any effects at all. During the cooling process, the austenite phase is decomposed into ferrite or martensite phases, depending on the cooling rate. By modeling the phase transformation in this process, we should be able to capture most of their effects on residual stress.

- The phase transformation during the heating process is occurred at relatively high temperature (above 750°C normally). At this high temperature range, the material is very soft and stress level is very low. Therefore, the stress/strain built-up in this process is very small, if there is any.

- The existing UMAT-CAT has already implemented a mechanism called "Annealing", which gradually eliminates the plastic strain build-up during the heating process at high temperature (above 750°C, this parameter is configurable in the input deck). Therefore, even if there were some additional strains contributed by the phase transformation to the plastic strain build-up during the heating process, these strains would also have been annealed.

- Numerical convergence considerations. Introduction of additional terms in the constitutive formulation at very high temperature range may complicate the convergence of UMAT algorithm (note that we are using the same robust incremental plasticity theory and numerical algorithms at both low and high temperature regions).

It is important to be aware that, according to the phase transformation theory, the phase transformation will not occur during the cooling process unless the peak temperature at the material point has reached a threshold value before. This threshold temperature will be one of the new control parameters passed into UMAT-CAT 4.0 from ABAQUS input deck and is configurable (default value: 800°C). UMAT-CAT 4.0 will keep track of the history of peak temperature at each material point for the entire thermal history (in case of multi-pass welds) and decide if the phase transformation effects should be triggered or not at that point.

III.1.4.2: Model Formulation

Based on the work of Fish et al (Ref .7), when phase transformation effects are considered, the total strain increment at a material point from t->t+Δt can be expressed as:

$$\Delta \in_{ij} = \Delta \in_{ij}^{e} + \Delta \in_{ij}^{pl} + \Delta \in_{ij}^{th} + \Delta\xi \frac{\delta}{3}\delta_{ij} + \Delta \in_{ij}^{TP} \qquad (8)$$

This expression derives from the classical incremental plasticity theory in which the total strain increment can be decomposed into the elastic, plastic, and thermal strain component increments. The last two terms in Eq. (8) represent the contributions of phase transformation to the strain increment. $\Delta\xi \frac{\delta}{3}\delta_{ij}$ represents the volumetric strain increment due to phase change and $\Delta \in_{ij}^{TP}$ represents the additional strain plasticity induced during the phase transformation. $\Delta\xi$ is the increment of phase volume fraction from t->t+Δt and will be calculated based on the internal field variables passed in from the UFIELD routine. UFIELD reads the phase volume fraction information from an external file. When multiple phases exist of (austenite, ferrite, pearlite, bainite, and martensite), the total value of the volumetric strain increment $\Delta\xi \frac{\delta}{3}\delta_{ij}$ will be calculated based on the mixture rule. The transformation induced plasticity $\Delta \in_{ij}^{TP}$ will be calculated based on Berveiller and Fischer as follows:

$$\Delta \in_{ij}^{TP} = \frac{5}{4}\frac{\left(\delta^2 + 3/4\gamma^2\right)^{1/2}}{\sigma_{y^*}} s_{ij}^{L}\Delta\xi \qquad (9)$$

$$\sigma_{y^*} = \sigma_y^n\left(\frac{1-\sigma_y^0/\sigma_y^n}{\ln\left(\sigma_y^0/\sigma_y^n\right)}\right) \qquad (10)$$

where s_{ij}^{L} is the local deviatoric stress tensor , σ_y^0 and σ_y^n are the yield stress of the parent (at time t) and product phase (at time t+Δt), respectively. $\Delta\xi$ is the incremental change of the volume fraction from t->t+Δt.

In the case of numerical instability or unavailability of yield stress for a specific phase, it may be difficult to calculate the strain plasticity according to Eqs (9) and (10). In this case, a more simplified formula can be used to calculate the transformation strain plasticity:

$$\Delta \epsilon_{ij}^{TP} = \frac{3}{2} K s_{ij}^{L} \Delta \xi \qquad (11)$$

where K is a constant of magnitude 4~5 x10^{-5} MPa^{-1} and can be configurable from input deck. The two phase transformation-related parameters, δ and γ, will be set as configurable parameters with the default values as follows: a) δ=0.008 for ferrite, pearlite, and bainite; b) δ=0.04 for martensite; and c) γ=0.2 for all phases.

The existing UMAT routine (UMAT-CAT 3.0) uses the classical incremental plasticity theory for the material modeling at both low and high temperatures. To account for the specific material behavior under welding conditions (e.g., at melting or near-melting temperatures) and to improve numerical stability of the algorithms, some specific features were added into UMAT, such as Virtual Element Detection (VED) and Annealing. Apart from these specific features, the fundamental strain decomposition form of the incremental plasticity theory is very similar to Eq. (8) except for the last two phase transformation strain terms. To add in the phase transformation strains, separate modules have been developed to calculate these terms. Since the phase transformation strains are dependent on the stress state at the material point (which is unknown until strain is calculated), these strain terms must be placed into the iteration loop of the plastic strain computation algorithm until a convergence is reached.

The two calculated phase transformation strains have been stored in two additional solution-dependent variables (SDVs) in UMAT, just like other elastic and plastic strain components. These two phase transformation strains can then be contour plotted in ABAQUS post processor. An additional variable will also be added in UMAT to trace/store the peak temperature at a material point for the entire welding history. This peak temperature variable will be compared to the configured threshold value at each time step to dictate if the phase transformation effects should be triggered or not. The contour plot of the peak temperature variable at the last time step can also be used to estimate the size of melting zone.

III.1.4.3: Model Test and Validation

This example demonstrate the application of UMAT-CAT 4.0 on a 2-D weld model with the temperature solutions obtained from ABAQUS thermal analysis. It is a single-pass T-Fillet weld as shown in Fig. 24. The temperature solutions are obtained by ABAQUS along with the DFLUX routine. The microstructure phase volume fractions were calculated by the external microstructure model and passed into UMAT-CAT by UFIELD routine. For the purpose of demonstrating the effects of microstructural phase transformation effects on residual stresses, three different cases were analyzed in this example using UMAT-CAT4.0:

Case #	**Description**
BaseLine Case	No Phase Transformation Effects
Case 1	With Phase transformatoin effects. About 7% Martensite in the weld after cooling
Case 2	With Phase transformation effects. About 70% Martensite in the weld after cooling

*Note: Annealing feature was turned on for all 3 cases

Fig.24 (a) shows the distribution of peak temperatures (Solution Dependent Variable #17) at the material points in and near the weld region. This is the maximum temperature experienced at these material points during the entire welding process. From this peak temperature distribution, we can estimate the size of the molten weld zone (>=1500°C) as well as the region in which the phase transformation occurs (>=950°C, the threshold temperature).

The residual stress distributions for the baseline case without phase transformation effects are shown in Fig. 24(b). As expected, tensile transverse residual stress (S11) occurs on near the weld toe.

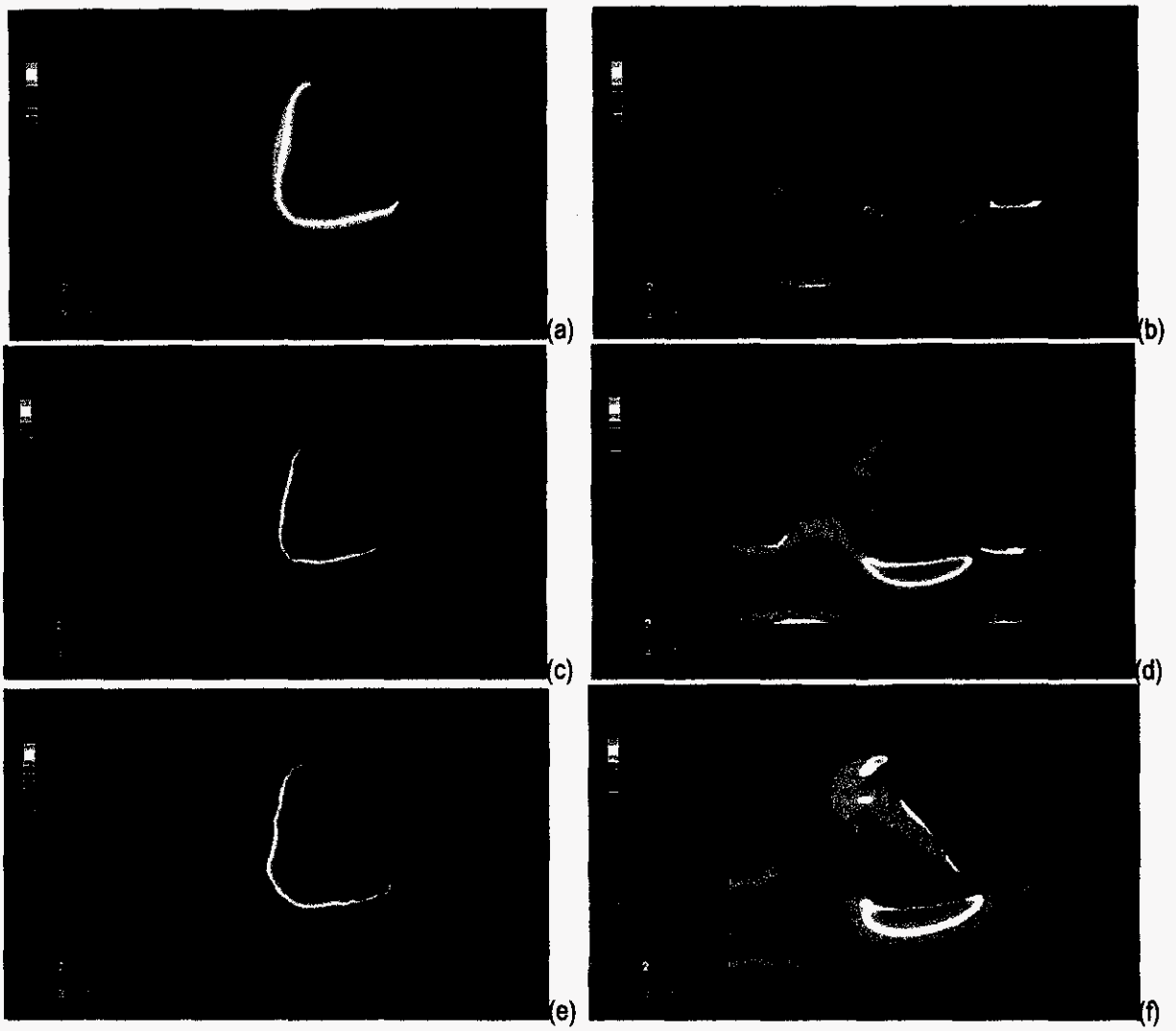

Fig. 24: (a) Peak Temperature Distribution – Molten Zone of the Fillet Weld (°C); (b) BaseLine Case – S11 (MPa); (c) Case 1 – Martensite Phase Volume Distribution; (d) Case 1 – S11 (MPa); (e) Case 2 - Martensite Phase Volume Distribution; and (f) Case 2 – S11 (MPa).

For the 2 cases with phase transformation effects, the final martensite phase volume distributions (Field Variable 6) are shown in Fig. 24(c) (Case 1) and Fig. 24(e), respectively. Case 1 forms roughly 7% martensite in the weld and Case 2 has roughly 70% martensite. These phase volume data were generated by the external microstructure program and read in by UFIELD into UMAT-CAT 4.0. The corresponding residual stress distributions for Case 1 and 2 are show in Figs 24(d) and (f), respectively.

A comparison of transverse residual stress (S11) distributions among the 3 cases is shown in Fig. 25. This is plotted along the top surface of the bottom plate starting from the weld toe. Compared to the baseline case, the magnitude of tensile residual stress (S11) near the weld toe is reduced in Case 1 when the phase transformation effects are considered (Case 1, 7% martensite). This is an indication of the effects of compressive strain generated by the phase transformation offsetting the tensile thermal strain caused by cooling. When the phase transformation effects become dominant (Case 2, 70% martensite), the transverse (S11) residual stress even becomes compressive.

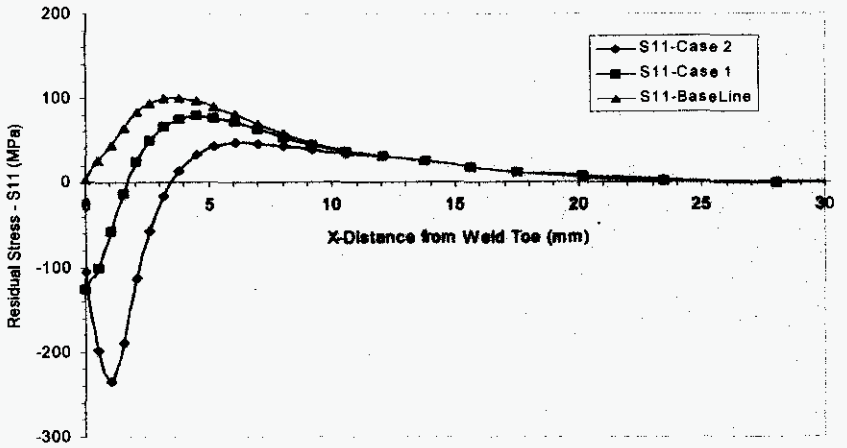

Fig. 25. Comparison of Transverse Residual Stress (S11) at the Top Surface of Bottom Plate.

The weld residual stress model was used to predict the residual stress pattern in a bead-on-plate weld sample, as shown in Fig. 26(a) and (b). The geometry of the weld sample is 152 mm x 152 mm x 12.7 mm. The welding parameters are as follows: 350A, 29.0V, and 8mm/s travel speed. Fig. 26 (c) shows the comparison of predicted and measured residual stresses at three points along the centerline. It can be observed that the predicted residual stresses are reasonable compared with those measured using x-ray.

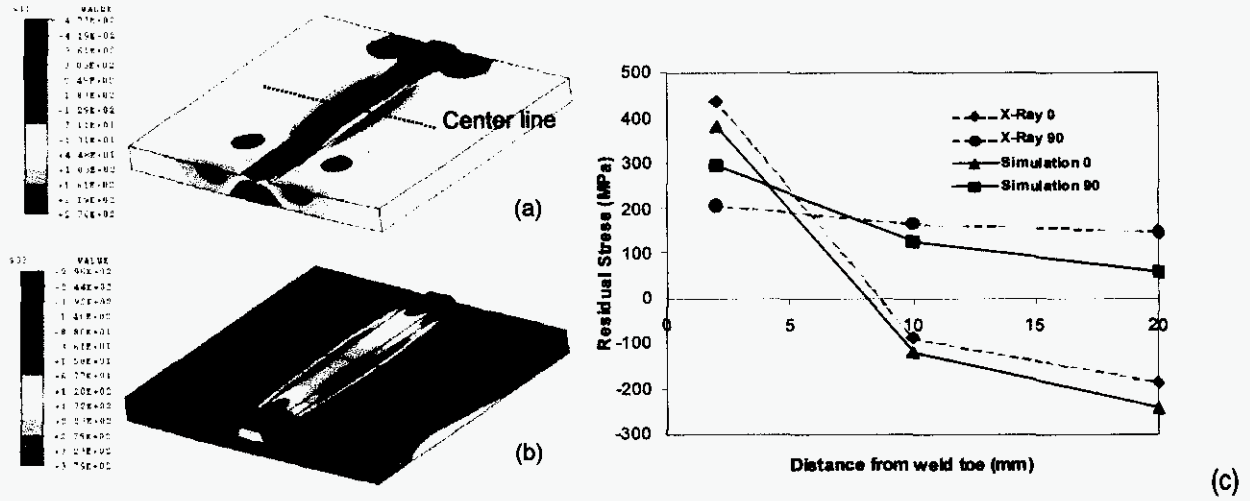

Fig. 26: residual stresses in the as-weld samples in direction (a) perpendicular and (b) parallel to welding direction. (c) Comparison of predicted residual stress with experimental data.

III.1.5: Weld Fatigue Model

III.1.5.1: Background on Weld Fatigue Model

In welded joints, it is generally accepted that crack propagation dominates the majority of the fatigue lives. It is well known that residual stresses can have significant effects on fatigue performance of welded joints. However, effective methods are not available in the literature in quantitatively relating a given residual stress distribution to fatigue life. Two major difficulties involved in such efforts are: One is that the residual stress distributions can have many subtle variations from a joint to another once material changes or welding procedures vary; the other one is that a given residual stress distribution must be directly related to a fatigue driving parameter in order to achieve a quantitative life prediction.

III.1.5.2: RESIDUAL STRESS MODEL FOR FATIGUE

III.1.5.2.A: Residual Stress Decomposition

Recently, a large amount of published residual stress distributions have been analyzed in detail by Dong and Hong (Ref. 8) in support of on-going fitness for service assessment procedures for pressure vessel and piping components. It was found that, although residual stress distributions in welded joints can exhibit many subtle variations, their contributions to fracture driving force can be drastically simplified by considering three fundamental components of a general residual stress distribution, i.e., membrane, bending, and self-equilibrating. As shown in Fig. 27, a given residual stress state can be decomposed into the three fundamental components by enforce equilibrium conditions as follows.

$$\sigma_m^r = \frac{1}{t}\cdot\int_0^t \sigma^r(x)dx$$

$$\sigma_b^r = \frac{6}{t}\int_0^t \sigma^r(x)(\frac{t}{2}-x)dx \qquad (12)$$

$$\sigma_{s.e.}^r = \sigma^r(x) - \sigma_m^r - \sigma_b^r(1-\frac{2x}{t})$$

Similar decomposition techniques in a mesh-insensitive manner were discussed in a series of recent publications (e.g., Ref. 9) for loading-induced stress distribution at a weld for both characterizing stress concentration effects and simplifying stress intensity solutions. Once a residual stress distribution is available from a residual stress prediction model, the through-thickness distribution $\sigma^r(x)$ such as at weld toe can be readily analyzed through Eq. 12 as a post-processing exercise. Both σ_m^r and σ_b^r after using Eq. 12 are expressed as constants, respectively. The component $\sigma_{s.e.}{}^r(x)$ can be expressed either as in the form of polynomial function of *x* or as discrete data points

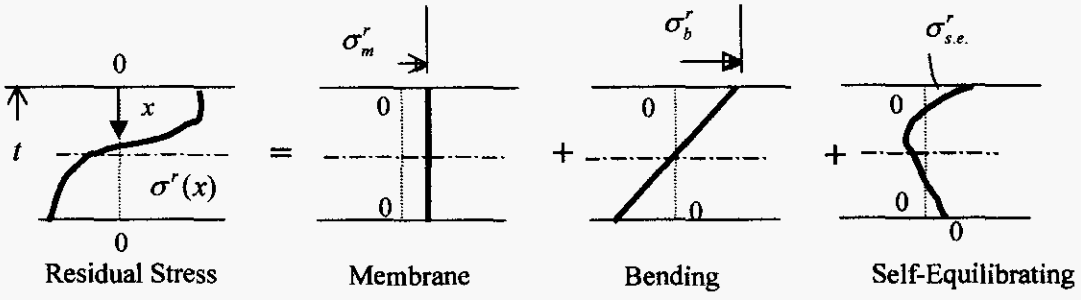

Fig. 27: Residual stress decomposition into 3 simple stress states.

III.1.5.2.B: Residual Stress Induced Stress Intensities

The significance of Eq.12 is that it transforms any arbitrary and complex residual stress distribution into an equilibrium equivalent stress state represented by three simple components. Then, a fatigue driving force in the fracture mechanics context becomes the seeking of stress intensity factor solutions corresponding to the three simple stress states. In this regard, a weight function approach is desirable, if it is available for a given joint geometry; however, this is often not the case. Assume that the weight function for a given joint geometry and crack configuration is expressed as *w(a,x)*, the stress intensity factor for a crack size of *a* along x can be expressed as:

$$K(a) = \int_0^a \sigma^r(x)w(a,x)dx \qquad (13)$$

Eq. 13 can be written with respect to a known weight function $w_p(a,x)$ for a simple straight plate as follows :

$$K(a) = \int_0^a \left(\sigma_m^r + \sigma_b^r(1-2x/t) + \sigma_{s.e.}^r(x)\right) \cdot w_p(a,x)dx \tag{14}$$

or

$$K(a) = K_m(a/t) + K_b(a/t) + K_{s.e.}(a/t) \tag{15}$$

The significance of Eq. 14 lies in the fact that the three components of a general residual stress distribution in Eq. 12 fully contains the geometry effects of the weld residual stresses for a given weld geometry and that the K solution can be performed using the same weight function $w_p(a,x)$ for a simple straight plate specimen.

If assuming the residual stress distribution at a hypothetical location such as a weld toe is stationary, i.e., the stress distribution remains the same as the crack propagate, typical load-controlled K solution from literature for straight plate specimens can be directly used for the membrane and bending components of a given residual stress state (Ref. 9):

$$K = K_m + K_b = \sqrt{t}\left[\sigma_m^r \mathrm{f_m}\left(\frac{a}{t}\right) + \sigma_b^r \mathrm{f_b}\left(\frac{a}{t}\right)\right] \tag{16}$$

The $\mathrm{f_m}\left(a/t\right)$ and $\mathrm{f_b}\left(a/t\right)$ are dimensionless functions of *a/t* for the membrane and bending components, which are described in details in ref. 9. If the $\sigma_{s.e.}^r(x)$ is negligible, Eq. 16 provides the K solution for the total residual stress effects on crack driving force under load-controlled conditions.

However, as discussed by Dong and Hong recently (Ref. 9), weld residual stresses re-distribute as a crack propagates. If K based on load controlled conditions are used, the crack driving force tends to be excessively over-estimated. A more appropriate K solution should be formulated using displacement-controlled conditions. However, the most of the K solutions and weight function solutions in the literature are based on load-controlled conditions. This is in part due to the complexities involved in considering displacement-controlled conditions. To overcome this difficulty, Battelle has recently developed a simplified engineering estimation formula for approximating displacement-controlled conditions. The weight function approximating displacement controlled conditions becomes simply:

$$w_p(a,x) = 2.24\sqrt{\frac{a}{\pi}}\frac{1}{\sqrt{a^2-x^2}} \tag{17}$$

As for the self-equilibrating part of the residual stress distribution, if it can be expressed in a form polynomial with respect with *x*:

$$K_{s.e.}(a) = \int_0^a \sigma_{s.e.}^r(x) \cdot w_p(a,x)dx \tag{18}$$

The validity of the approximate K solution scheme is documented in Fig. 28. It can be seen that using a 3 dimensional finite element alternating method for the same hypothetical residual stress distribution, the K solution is essential. Furthermore, if load-controlled conditions are assumed, the stress intensity (K) can be rather significantly

over-estimated as shown.

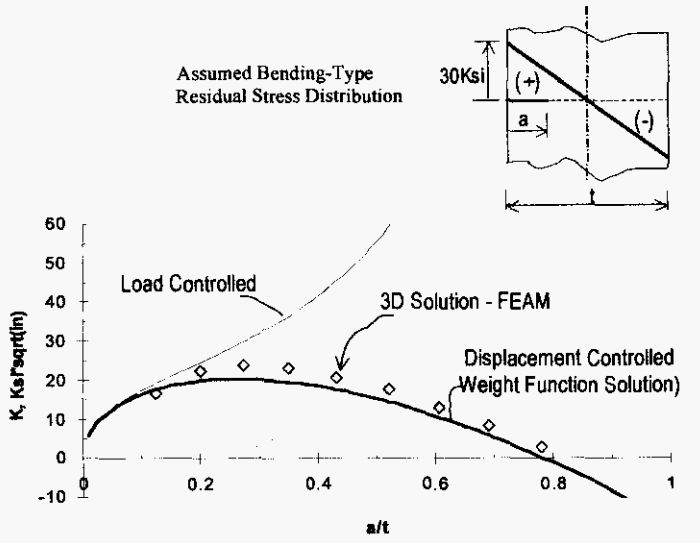

Fig. 28: Validation of approximate K solution procedure and comparison of K solutions using load-controlled and displacement-controlled conditions

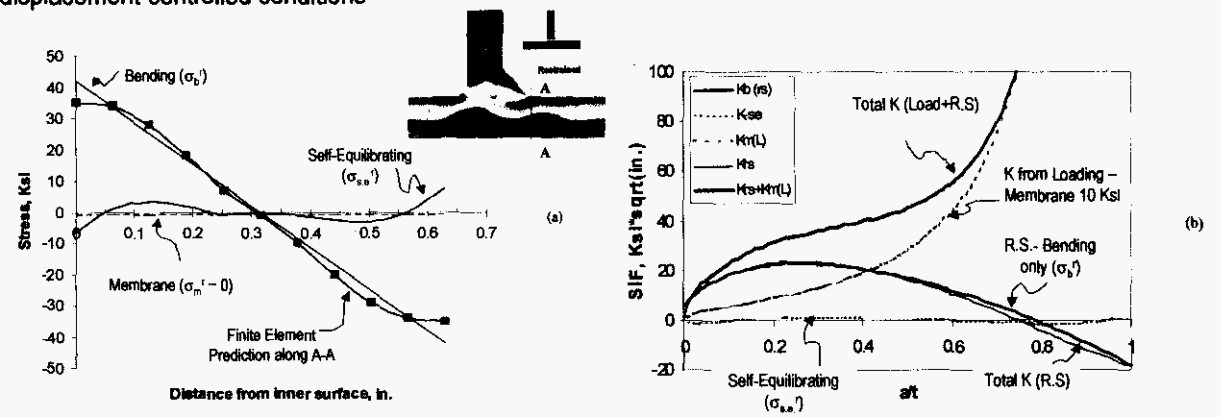

Fig. 29: Residual stress decomposition for a T-fillet weld along A-A and contributions to K solution: (a) residual stress components after decomposition; (b) comparison to K due to residual stress components and a remote membrane loading of 10Ksi

If a realistic residual stress distribution for a T fillet weld such as that shown in Fig. 29 is considered, the detailed residual stress contributions to K can be quantified and the requirements for residual stress estimate requirements can be demonstrated in terms of their contributions to K solutions. In the meantime, remote loading induced stress intensities can then be consistently considered as the total fatigue driving force.

If we assume the T-fillet is also subjected to a remote tension in addition to the as-welded residual stress state, the remote loading induced stress intensities can be calculated under load-controlled conditions, as shown as $K_m(L)$ in Fig. 29(b). As for the residual stress induced stress intensities, by following the decomposition procedures described in Eq. 1-1, the membrane, bending, and self-equilibrating parts of the residual stress distribution along line A-A are plotted in Fig. 29a. The membrane component σ_m^r is negligible and therefore, is not shown individually in Fig. 29b. The bending component σ_b^r is dominant, with the maximum stress above the base material yield strength (about 37Ksi), occurring at the top surface. The self-equilibrating part $\sigma_{s.e.}^r$ is rather small with peak stresses less than 5Ksi. The resulting K as a function of *a/t* from both bending and self-equilibrating parts of the residual stresses (based on

Eq. 1-1) are shown in Fig. 28b, in which the K contribution from the self-equilibrating component is nearly not noticeable. As expected, the bending component dominates the residual stress contribution to K. The difference between the total K (due to both loading and residual stresses) and the K due to loading only signifies the contribution of the residual stresses for the full range of crack depth (a/t). Once the stress intensities due to weld residual stresses and service loading are obtained as shown in Fig. 29b, the service life can be predicted using by invoking Paris law, which is described in the next section.

III.1.5.3: Two-Stage Crack Growth Fatigue Model

Based on the Battelle JIP on weld fatigue, it is further demonstrated that the whole propagation based fatigue life can be further described as small crack propagation (or nucleation to "engineering" size crack) to long crack propagation, governed by stress intensities corresponding to the two stages of the crack growths, respectively. With such characterization, when a relative crack size is small (a/t <0.1), the crack growth behavior is dominated by $\Delta K_{a/t<0.1}$, in which the weld toe notch effects are dominant. Once a crack size becomes larger than a/t =0.1, the stress intensities are not influenced any more by the presence of a notch. The modified two-stage crack growth model is expressed as:

$$\frac{da}{dN} = C\ (M_{kn})^n (\Delta K_n)^m \qquad (19)$$

where the notch-induced stress intensity magnification factor is expressed as

$$M_{kn} = \frac{K_{Notch}(\text{with local notch effects})}{K_n(\text{based on through thickness } \sigma'_m \text{ and } \sigma'_b)} \qquad (20)$$

The effectiveness of the two-stage growth law is demonstrated in Fig. 30 by considering various short crack data (including commonly referred "microstructurally short", "physically short", and "mechanically short" cracks in the literature). The importance of Fig. 30b is that once both "short" and long crack growth data can be consolidated into a single curve (or narrow band), fatigue life can then be predicted by integrating Eq. 2-1 with M_{kn} and ΔK expressions are defined from the on-going JIP work.

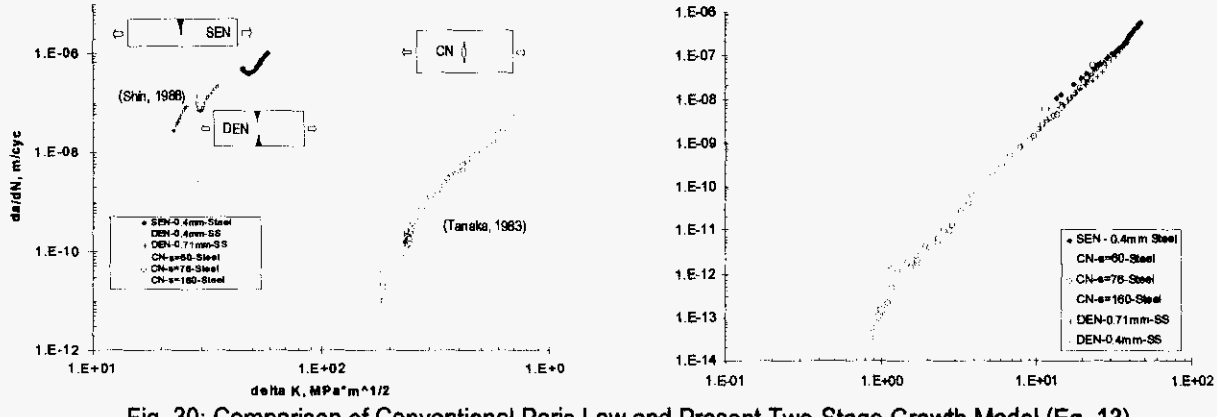

Fig. 30: Comparison of Conventional Paris Law and Present Two-Stage Growth Model (Eq. 13)

Eq. (19) works well for as-welded conditions in which the presence of high tensile residual stresses tends to wash out any load ratio effects and the parameter ΔK_n implicitly considers the residual stress effects on an average sense. However, to explicitly take into account of weld residual stress effects, the stress intensity (K) contribution due to residual stresses should be taken into account using the K solutions for any given crack size, the K due to residual stresses can be assumed to be solely determined by displacement controlled K solution scheme as demonstrated earlier. Based on the further investigations and review of existing literature in this subtask thus far, it is proposed that the crack growth model in Eq. (19) can be further modified to explicitly consider weld residuals stress effects, as

follows:

$$\frac{da}{dN} = C\ (M_{kn})^n (\Delta K^+ K_{max})^m \tag{21}$$

where, ΔK^+ represents the positive range of the K due to both applied load and residual stresses (i.e., $K = K_n + K_{rs}$) and K_{max} is its maximum within a given cycle, both of which are a function of the applied load ratio and residual stress state at the growing crack tip. The exponents *n* and *m* are the crack growth law exponents corresponding to the "short" and long crack growths.

III.1.5.4: Two-Stage Growth Fatigue Model Incorporating Weld Residual Stress Effects

III.1.5.4.A: Overall Procedure

The two-stage crack growth model incorporating residual stress effects is developed to estimate fatigue lives for welded structures. Fatigue Life Prediction with Considering Residual Stress Effects. The overall procedure for two-stage growth fatigue model incorporating weld residual stress effects is given in Figure 31.

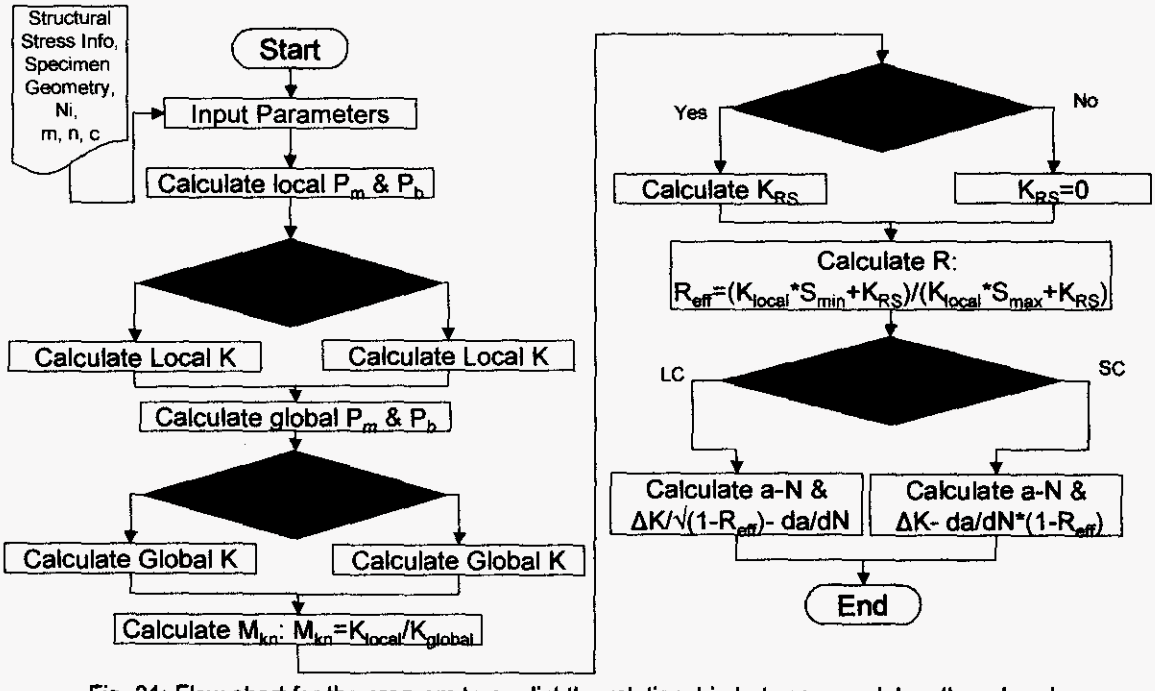

Fig. 31: Flow chart for the program to predict the relationship between crack length and cycle

(1) Calculate structural stresses and notch stresses.

   a. Perform finite element analysis on the specimens.

   b. Conduct structural stress method to obtain far-field membrane and bending structural stresses (σ_m^t, σ_b^t), and equivalent membrane component (σ_m) of structural stress at t_1=0.1t.

   c. Calculate notch stresses (P_m, P_b), which is function of a/t.

(2) Obtain stress intensity factors using the far-field structural stress and notch stresses.

   a. Calculate load controlled K values (K_{max} and K_{min}) induced by cyclic loading.

   b. Characterize the given residual stress distribution and perform a functional fit, if the residual

stress is included in the specimen.

c. Calculate displacement controlled K solution (K_{RS}) induced by residual stress.

d. Calculate effective load ratio, R_{eff}, based on combined K ratio,

$$R_{eff} = \frac{(K_{mim} + K_{RS})}{(K_{\max} + K_{RS})}.$$

(3) Decide coefficients C and *m* of the regression line from the data sets using the following relationships:

a. Long crack growth behavior (LCB) :

$$\frac{da}{dN} \cdot \frac{1}{(M_{kn})^2} \quad \text{vs.} \quad \frac{\Delta K_n}{\sqrt{1 - R_{eff}}}$$

b. Small crack growth behavior (SCB) :

$$\frac{da}{dN} \cdot \left(\frac{\sqrt{1 - R_{eff}}}{M_{kn}}\right)^2 \quad \text{vs.} \quad \Delta K_n$$

(4) Calculate the fatigue cycles using the following equations with the C and *m* obtained from (3), and validate them with the test data [10, 11].

a. Long crack growth behavior (LCB) : $N_f = \int_{a_i}^{a_f} \frac{(1 - R_{eff})^{\frac{m}{2}}}{C \cdot (M_{kn})^n (\Delta K_n)^m} da + N_i$

b. Short crack growth behavior (SCB) : $N_f = \int_{a_i}^{a_f} \frac{(1 - R_{eff})^{\frac{n}{2}}}{C \cdot (M_{kn})^n (\Delta K_n)^m} da + N_i$

III.1.5.4.B: Model Validation

Comparison with Toyosada's [Ref.10]

The specimen shape and dimensions are in Fig. 32. It is under center cracked tension (CCT) with 10mm crack. The width and thickness of the specimen are 50mm and 4mm, respectively. The specimens were made of HT-50 steel plate. As shown in Fig. 32a, the residual stresses are generated using the line heating with different heating locations on the specimen; one is flame line heating along a centerline (Case 1) and the other is along edge line (Case 2). Due to the heating location difference, there exist different residual stresses as shown in Fig. 32b.

Three types of specimens are considered:

- C specimen: compressive residual stress at the crack tip (Case 2)
- T specimen: tensile residual stress at the crack tip (Case 1)
- N specimen: no residual stress (no heating)

The measured stress distributions in the specimens are shown in Fig.32b. For all 3 types of specimens, applied maximum load is 26.46kN and load ratio (R) is R=0.05.

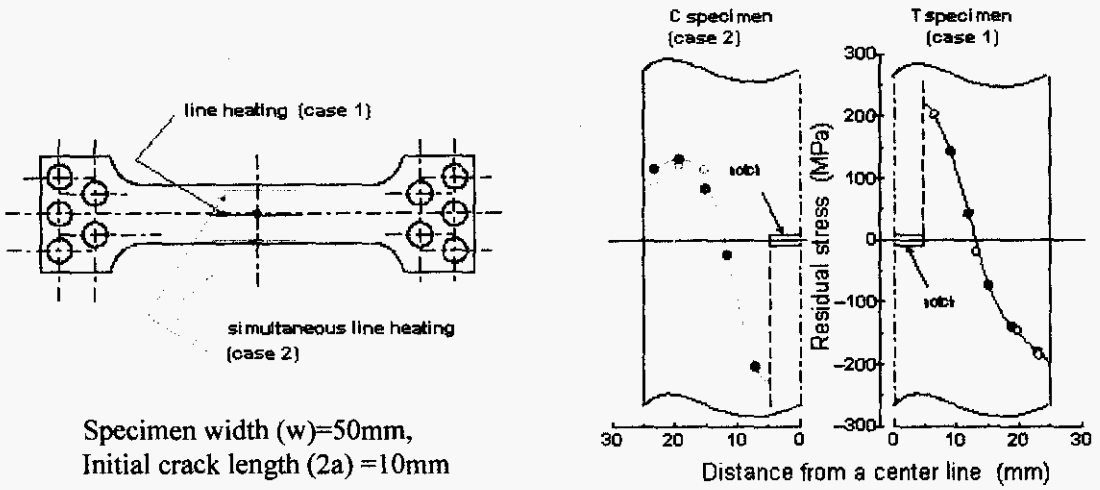

Fig. 32: Toyosada, et al [Ref.10]'s model (a) Specimen; (b) Measured residual stress distribution after line heating

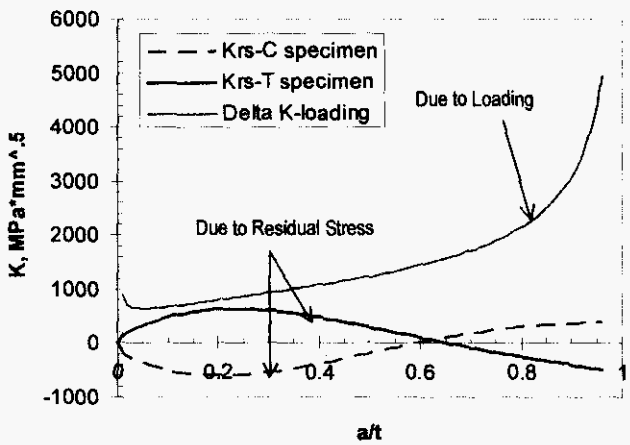

Fig. 33: K calculations due to residual stress and loading

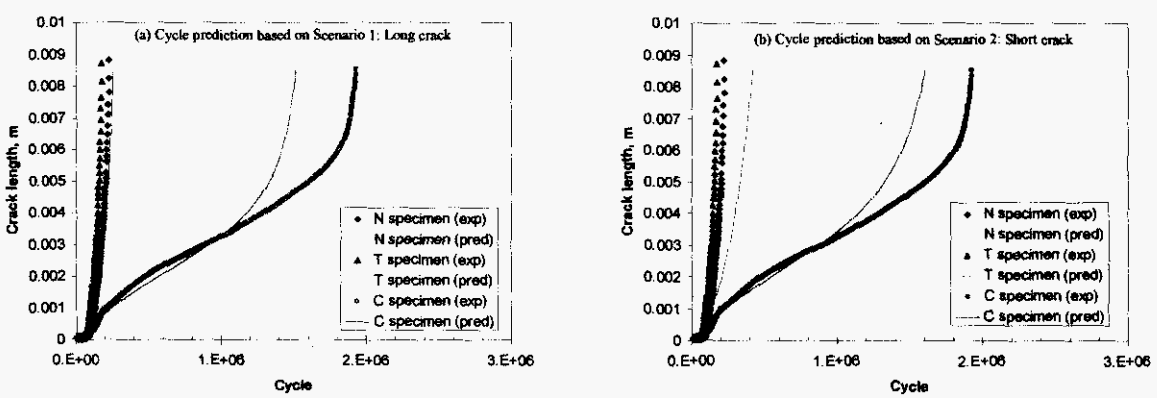

Fig. 34: Crack growth comparison between prediction and measurement using two different scenarios

Fig. 33 shows the K behaviors verse the crack size. Fig. 34 shows the K behaviors verse the crack size. Finally, crack growth comparison between prediction and measurement is shown in Fig.34a (for LCB) and 34b (for SCB). It can be

observed that the predicted crack growth from both scenarios is in reasonable agreement with the actual test data.

Comparison with Glinka's [Ref. 11]

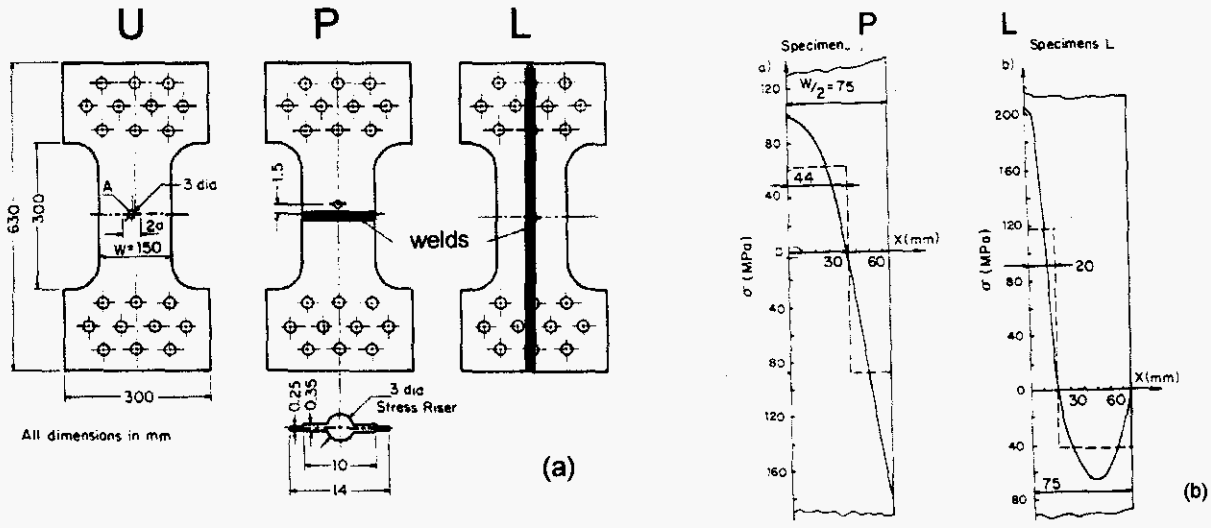

Fig.35: Specimen preparation and measured weld induced residual stress distribution in Specimen P and L from Glinka's[Ref. 11]: (a) Three different specimen preparation, where P and L are welded specimens (weld in red line); (b) Welding induced residual stress distributions in Specimens P and L.

The specimen shapes and dimensions are in Fig. 35a. It is under center cracked tension (CCT) with 14mm crack. The width and thickness of the specimen are 150mm and 4mm, respectively. The material used is low alloy hot-rolled and normalized medium strength steel 18G2AV. As applying the welding in parallel to initial crack direction (P specimen) or in normal to initial crack direction (L specimen), different types of residual stresses can be generated (see Fig. 35b). U specimen has no residual stresses in the specimen. Two different loading conditions are applied:

1) $\Delta\sigma$ =111 MPa, R=0.35

2) $\Delta\sigma$ =107 MPa, R=0.5

K behaviors are shown in Fig. 36a. R_{eff} based on Ks is all positive regardless of crack size and cyclic loading ratio shown in Fig. 36b-c.

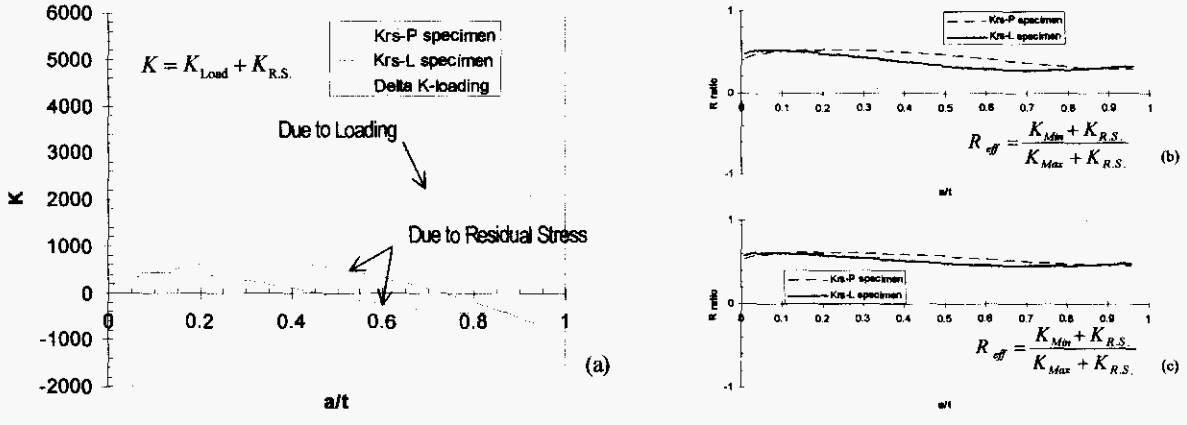

Figure 36: (a) K range for P, L specimens; (b) Load ratio calculation when R=0.35; (c) Load ratio calculation when R=0.5

Figs.37 (a), (b),(c) and (d) show the crack growth predictions using Scenarios 1 and 2. The predictions from both scenarios show good co-relation with test results.

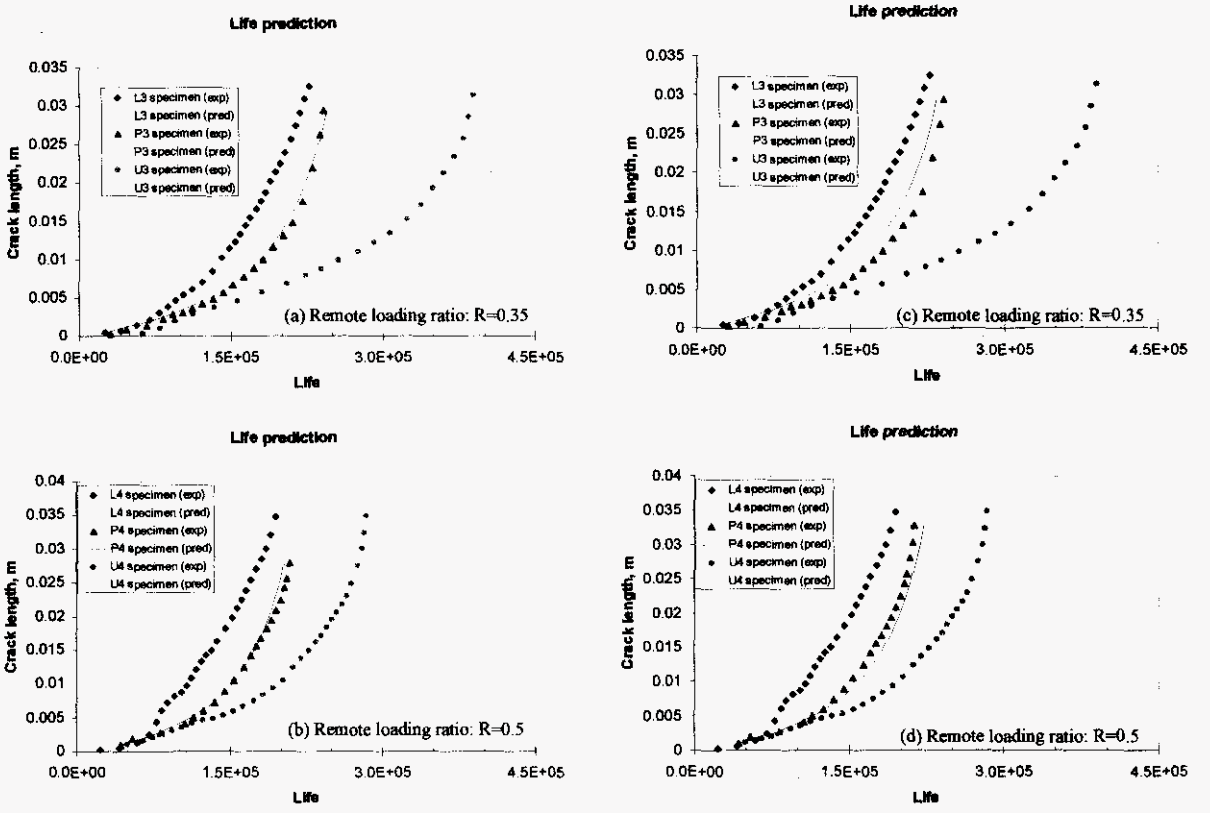

Fig. 37: (a) and (b) - Crack length vs. cycle prediction using Scenario 1: Long crack; (c) and (d) - Crack length vs. cycle prediction using Scenario 2: short crack

III.1.5.5: Weld Residual Stress Effects on Fatigue Lives

The objective is to provide a numerical procedure to analyze weld residual stress effects, and be able to predict fatigue lives for the specimens with residual stresses, based on the life measurements from the specimens without residual stresses. Note that here mean life means the life without residual stresses, which is known beforehand. Fig. 38 shows the flow chart for fatigue life prediction considering the effect of residual stresses.

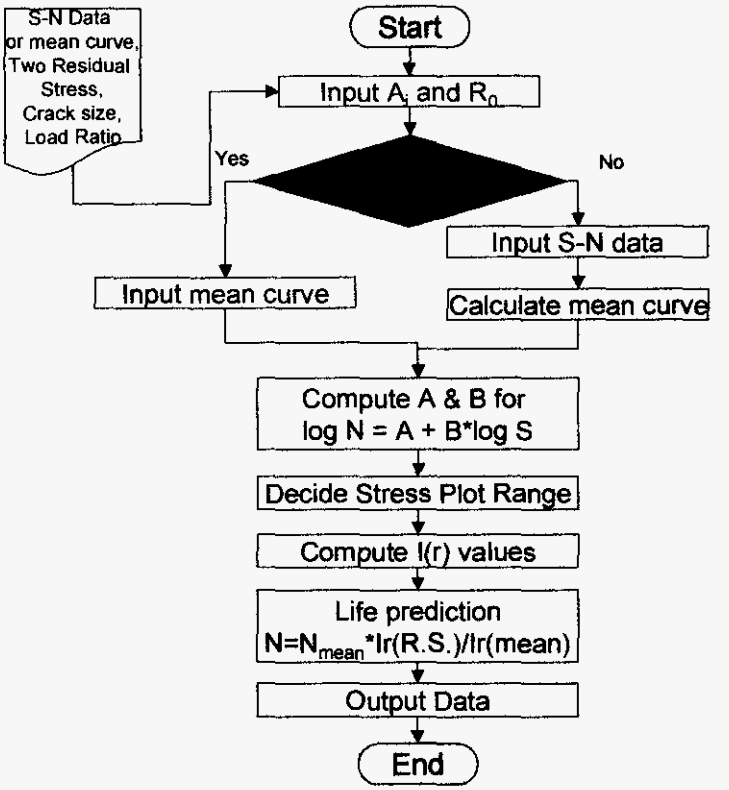

Fig. 38: Flow chart of the program to predict fatigue life incorporating residual stresses

Life Prediction

$$N = \frac{1}{C} \cdot t^{1-\frac{m}{2}} \cdot (\Delta\sigma_s)^{-m} \cdot I(r) \tag{22}$$

So, the relationship between the mean life N_{mean} and the life with residual stress N_{RS} should be:

$$N_{RS} = N_{mean} \cdot \frac{I_{RS}(r)}{I_{mean}(r)} \tag{23}$$

I(r) Calculation

$$I(r) = \int_{\frac{a_i}{t}}^{1} \frac{1}{\frac{1}{\sqrt{1-R_{eff}}} \cdot \left[f_m(\frac{a}{t}) - r \cdot \left(f_m(\frac{a}{t}) - f_b(\frac{a}{t}) \right) \right]} d(\frac{a}{t}) \tag{24}$$

where $R_{eff} = \dfrac{K_{\min} + K_{RS}}{K_{\max} + K_{RS}}$,

$$K_{RS}(a) = 2.24 \cdot \sqrt{\frac{A+a}{\pi}} \int_{A}^{A+a} \frac{RS(x)}{\sqrt{(A+a)^2 - x^2}} \cdot dx ,$$

$$K_{\max} = \sigma_{\max} \cdot (f_m + f_b) ,$$

$$K_{\min} = R \cdot \sigma_{\max} \cdot (f_m + f_b) , \text{ and}$$

$$R = \frac{\sigma_{\min}}{\sigma_{\max}} .$$

Note: $R_{eff} = R$ when the mean life is calculated.

Example and Validation

In this example, the mean life (without residual stress) is given, and fatigue lives need to be predicted for the specimen under both uniform tensile (+100MPa) and compressive (-100MPa) residual stresses. The fatigue life prediction under different residual stress distribution is displayed in Fig.39. It can be seen that the fatigue life is increased when the specimen is under compressive residual stress, while the life is decreases under tensile residual stress.

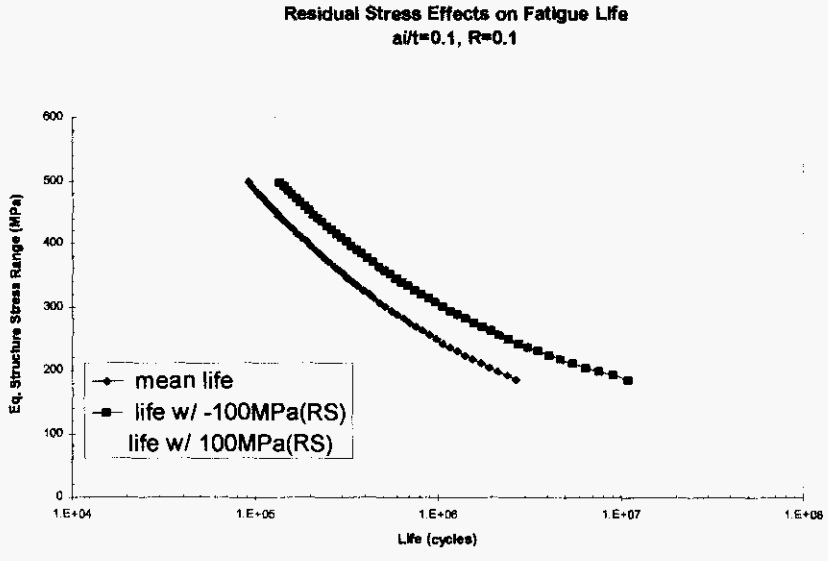

Fig.39: Fatigue life prediction under different residual stress distribution

Result compassion between prediction and measurement is displayed in Fig. 40. The solid blocks are data from the weld stress relieved specimens (without residual stress), and the empty blocks are from as-welded specimens (with residual stress). The thin solid lines are predictions with the bending-type of tensile residual stresses.

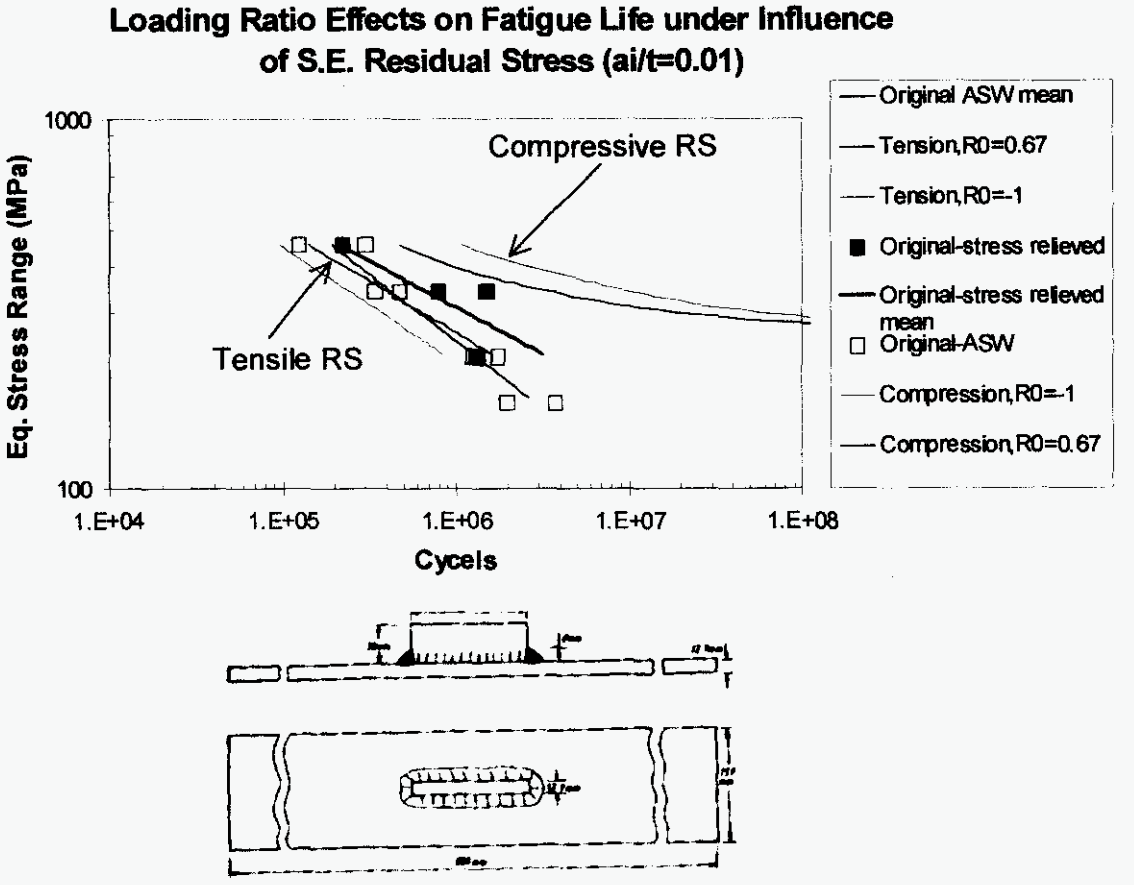

*The fatigue testing data is from Maddox [Ref. 12]
*All as-welded cases were spot-heated to ensure high tensile residual stresses.

Fig. 40 Residual stress effects on fatigue life

III.1.5.5: SUMMARY of Weld Fatigue Model

- A consistent procedure for incorporating any arbitrary weld residual stress distributions into a fatigue driving force model has been established. The driving can be expressed as stress intensity parameter under displacement controlled conditions.
- The stress intensities (K) due to residual stresses can be directly added to the stress intensities induced by remote loading. However, the residual stress induced intensities should be considered as mean-stress effects, not contributing directly to ΔK in conventional Paris type crack growth law
- Developed a two-stage growth model and examined more detailed crack nucleation definition based on recent short crack data from literature and further considerations in the proposed two-stage growth model
- Fatigue lives incorporating residual stress effects can be calculated using K ratio, which combines the displacement controlled K for residual stress effects and the load controlled K for pure loading.
- Based on two-stage crack growth, the crack growth verses cycle can be predicted. The notch effects can be calculated based on the structural stress concept.
- There is a good agreement between predictions and experiments using Toyosada's [10] and Glinka's [11] models.
- The prediction of crack growth vs. cycles either using Scenario 1(long crack behavior) or Scenario 2 (small crack behavior) shows good correlations with testing data for Toyosada's and Glinka's cases.

III. 2: Special Welding Wire Design and Evaluation

III.2.1: Background on Special Welding Wire

A special weld consumable has been developed in this project to introduce compressive weld residual stress at weld toe. The concept was based on a special welding wire developed in Japan [13]. The welding wire developed in Japan can generate compressive residual stress at weld toe by the expansion of volume due to low temperature martensite transformation. This allows the weld metal to transform its austenite in the latter stages of cooling and therefore maximize the effect of the martensitic transformation in terms of volumetric expansion since the thermal contraction effect won't diminish the phase transformation expansion. The special welding wire will also be referred as Lower Temperature Transformation Wire (LTTW) in the follow sections of this report.

Experimental results in Japan have shown that weld fatigue strength can be increased by 2X due to the introduction of compressive residual stress at weld toe. In this project, Colorado School of Mines, one of the project partners, developed a new welding wire. Considering the similar effect of Mn on martensite transformation, the Nickel has been replaced with Manganese to reduce the cost in the new welding wire developed in this project.

III.2.2: Optimize Wire Composition for Desired Ms and Mf

The first step of this project was to develop a welding-wire manufacturing procedure that resulted in good quality consumables. This included the determination of the main wire fabrication variables such as powder mixing times, speed of drawing and filling, drawing sequences, filler elements drying method, and conditions for cleaning and baking of the final product. Restrictions in the amount of metal powder filling that can be added to the wire and a limit to the drawing speed and final wire size were established, still appropriate selection of strip metals and filling powders (chemistry and size) allows the manufacture of any required composition. Specific welding parameters were established together with known welding wire compositions.

With a sound welding-wire manufacturing procedure, compositions that mapped the martensite field of the Schaeffler diagram were manufactured (Figure 41). These weld metals (Table 6) resulted in slightly different martensite fractions as well as a range of predicted transformation temperatures that were later evaluated.

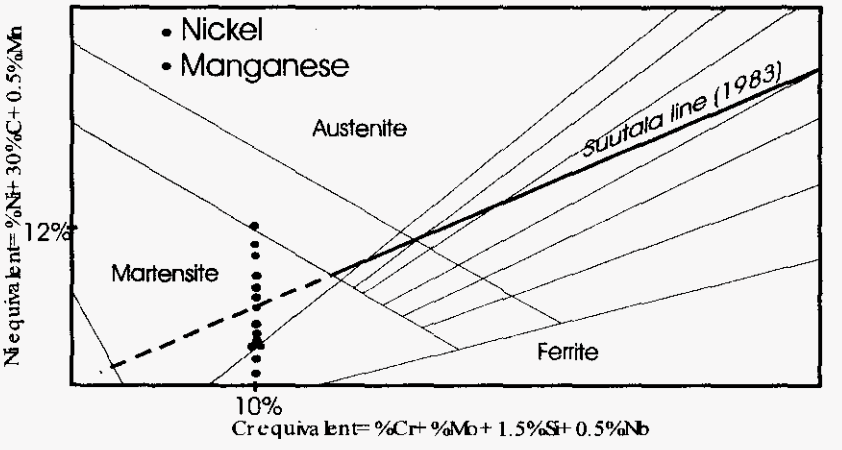

Fig. 41. View of the Schaeffler diagram depicting the experimental matrix of this study.

During the first welding trials, noticeable reductions in the fluidity of the molten metal were encountered (Figure 42a). This resulted in rough morphologies, especially in those weld metals with high manganese content. The problem was partially solved by establishing a hot welding parameters window. After preliminary weld test runs, and based only on the bead morphology, a new set of welding parameters (32V, 25.5cm/min, 300 to 350A) was determined. These welding conditions showed to improve the morphology of the weldments but undercutting became a problem.

Table 6. Composition of Experimental Weld Metals

Wire Code	Element content (as dep. wt.%)				
	%Cr	%Mn	%Ni	Ms (°C)	Mf (°C)
Mn1	12.3	1.76	0.08	533	400
Mn2	11.8	3.68	0.07	520	400
Mn3	11.2	5.93	0.07	370	270
Mn4	11.3	7.6	0.07	272	160
Mn5	10.8	9.02	0.07	150	50
Mn6	11.2	12.8	0.07	NA	NA
Mn7	10.7	14.4	0.08	25	NA
Cr1	10.5	0.09	0.1	537	486
Ni1	11	0.2	3.41	293	147
Ni2	11.3	0.22	6.17	220	113
Ni3	12	0.28	9.99	170	135
Ni4	9.8	0.2	11.2	NA	NA
Ni5	10.4	0.21	12.2	NA	NA

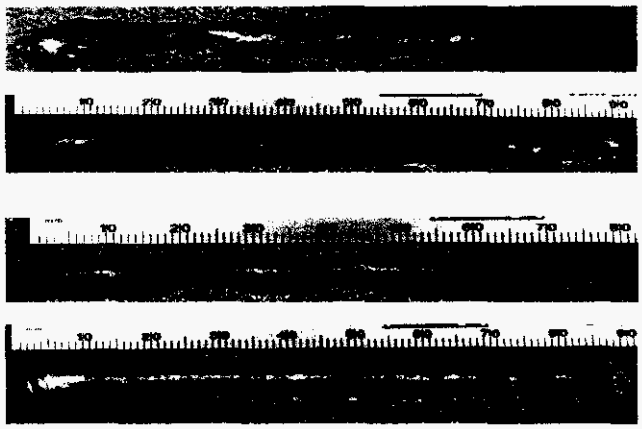

Fig. 42. Views from different Mn-based weld alloys. Bead on plate weldments. From top to bottom: 0.2Si, 0.27Si, 0.35Si, and 1.88Si. ASTM A-36 base material.

Further work in this area was performed and the addition of other fluidity enhancing elements, like silicon, required. Additional testing later revealed that these elemental additions did not modify the martensitic transformation and strongly affected the morphology of the final weldment (Figure 43).

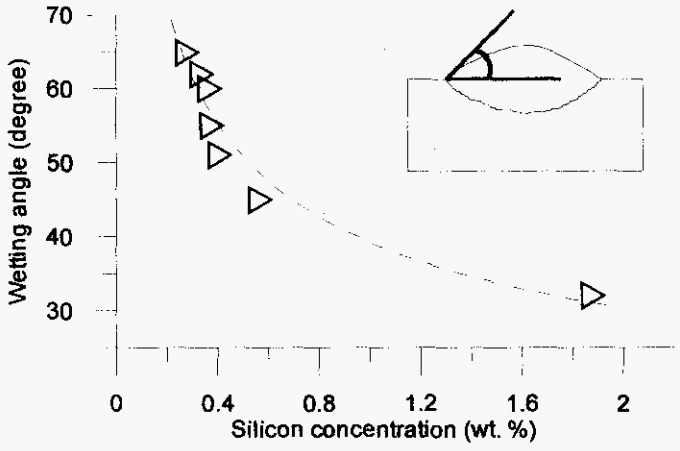

Fig. 43. Effect of silicon additions on the resulting weld geometry (BOP coupons).

A dilatometric characterization of all the alloys in the experimental matrix was also performed. With the aid of a thermomechanical simulator (Figure 44), the coefficients of thermal and martensite transformation start and finish temperatures were determined (Figures 45 and 46). For every composition, at least four samples were analyzed.

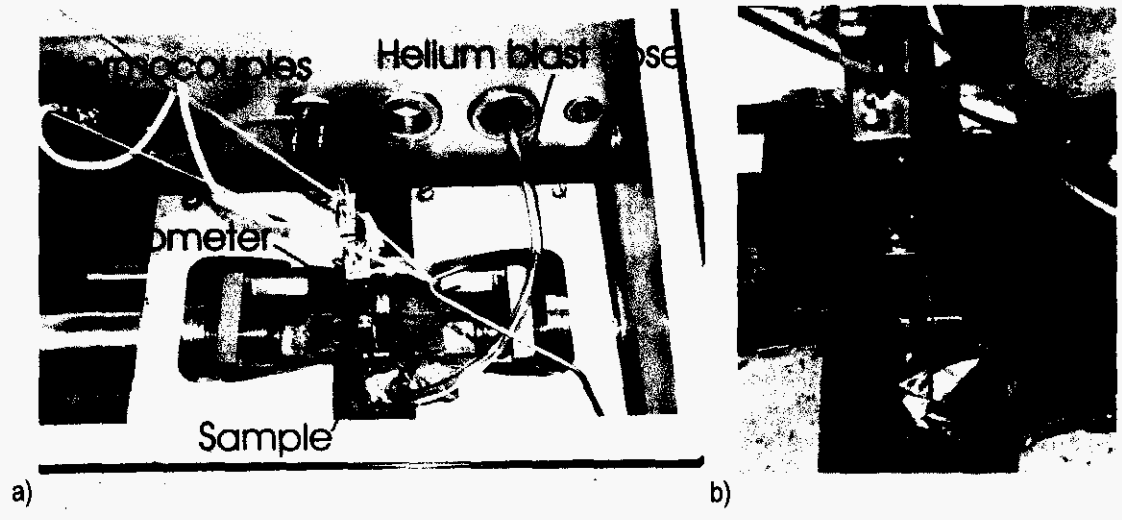

Fig. 44. General view of the Gleeble 1500 testing chamber (a) and detail of a typical sample set-up (b). The circumferential dilatometer is held by means of rubber bands to allow it to move freely.

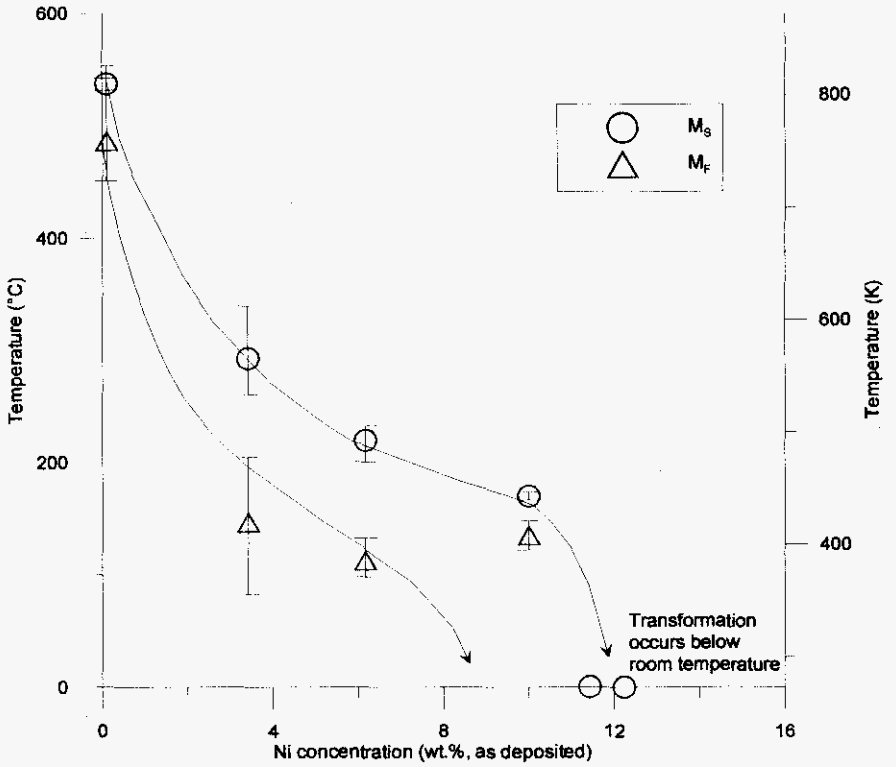

Fig. 45. Martensite transformation temperatures for the Ni-based weld metals. Gleeble 1500 Thermomechanical Simulator.

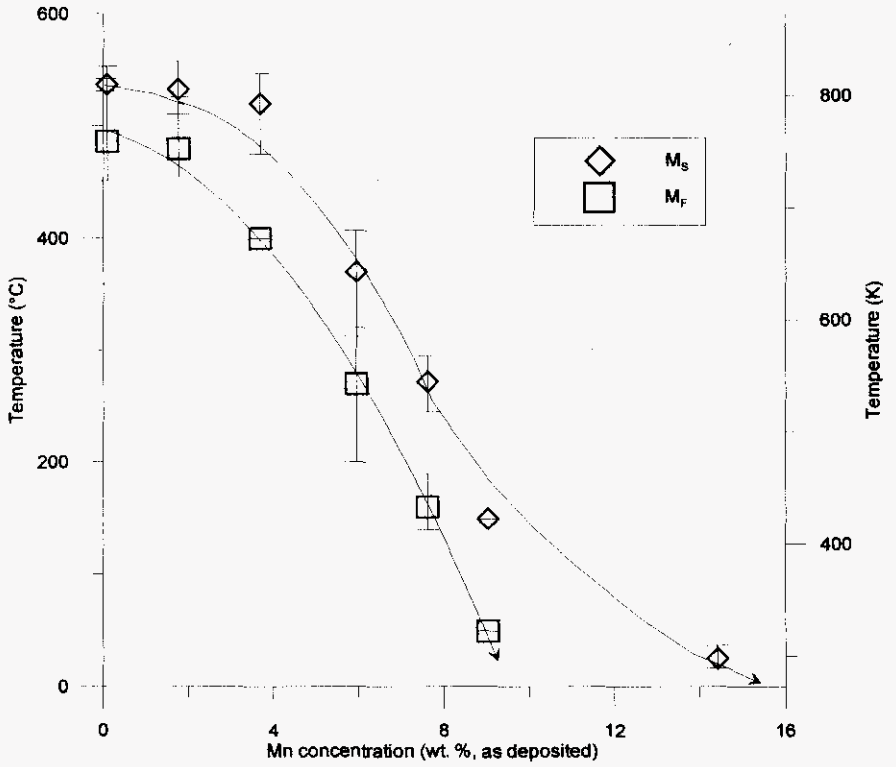

Fig. 46. Martensite transformation temperatures for the Mn-based weld metals. Gleeble 1500 Thermomechanical Simulator.

The criterion used to determine the pertinent transformation temperatures was the inflexion points of the cooling regime (Figure 47). The first inflexion point in the cooling stage was taken to be the Ms temperature and the second inflexion point as the martensite finish temperature.

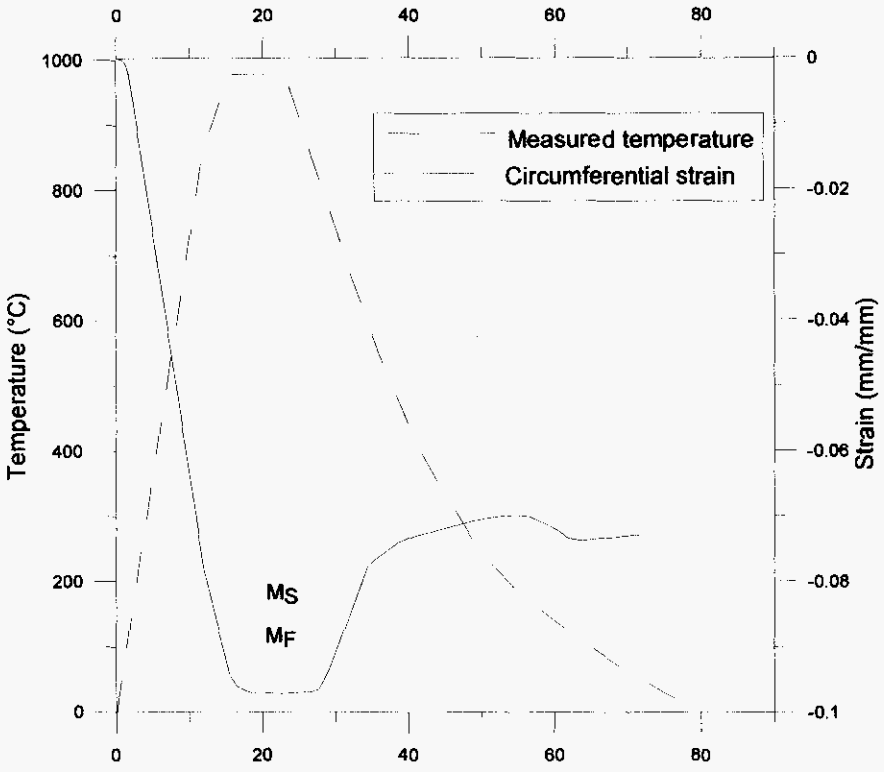

Fig. 47. Typical (Ni3 alloy) temperature vs. time and stain vs. time profile. As evaluated with circumferential dilatometers (Gleeble 1500).

Upon analysis of the evaluated transformation temperatures, discrepancies with predictive tools were found (Figure 48). Changes of curvature in the transformation temperature vs. composition relations were also found (Figures 45 and 46). Microsegregation analysis were conducted on Ni-Cr and Mn-Cr based weldments to help understand both, the difference between measured martensite start temperatures and estimated temperatures by traditional Ms predictive equations and mathematical models like the one developed by QuesTek and changes of the effect of alloying elements in the martensitic transformation.

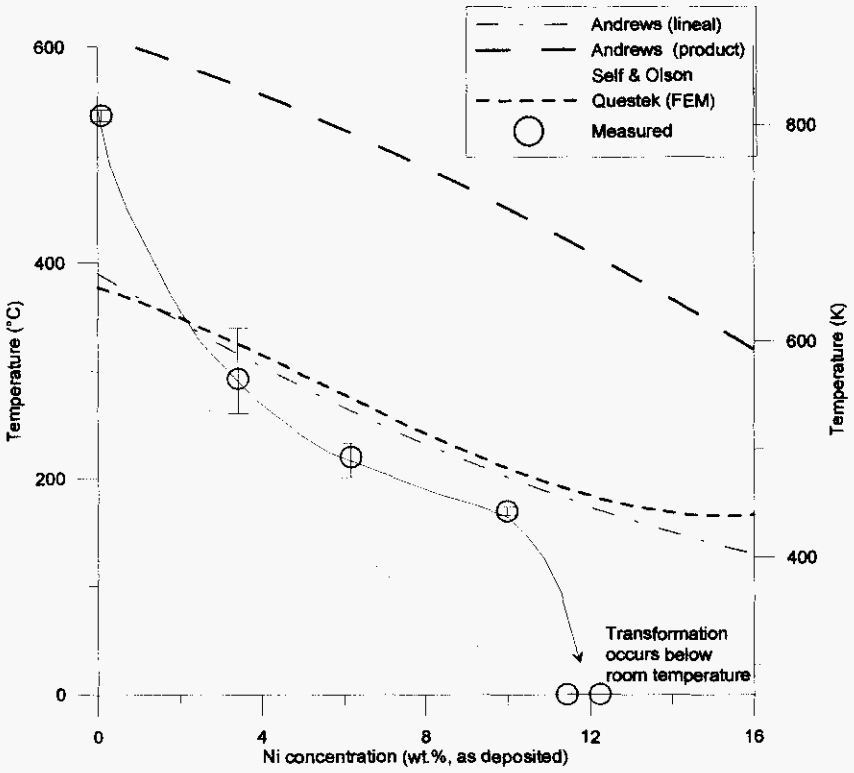

Fig. 48. Comparison of the analyzed martensite start temperatures of the Ni-based weld-metals with predictive values.

Optical and scanning electron microscopy with special etchants revealed the original solidification microstructure (Figure 49). With the aid of electron discharge spectroscopy (EDS) segregation profiles were obtained and analyzed. In the nickel-based welds, segregation of both nickel and chromium was found. Maximum concentration of chromium occurred in the interdendritic region at the ferrite-austenite interphase. The minimum chromium concentration occurred in the middle of the interdendritic region (Figure 50). This minimum was at the same level as the bulk concentration of chromium inside the dendrites of both nickel and manganese-based welds.

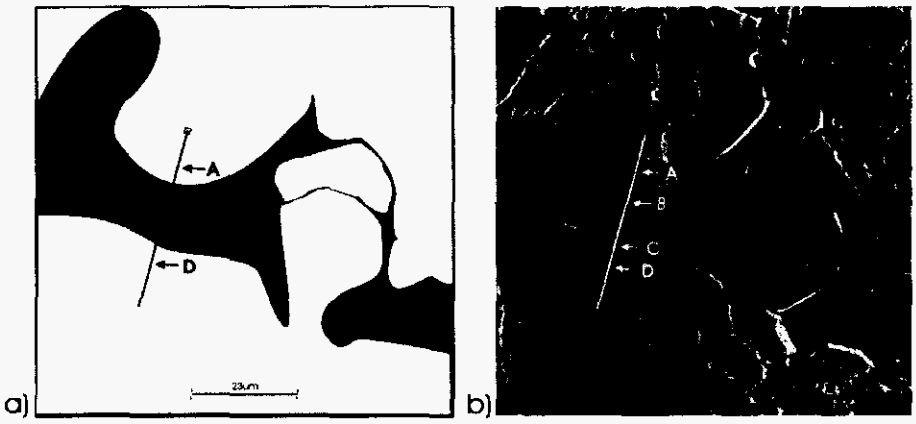

Fig. 49. Schematic representation (a) of a typical EDS linear analysis and its electron micrograph (b). In both sections points A and D correspond to two different dendrite arms, B and C to the dendrite solidification boundary and the line to the actual analyzed section.

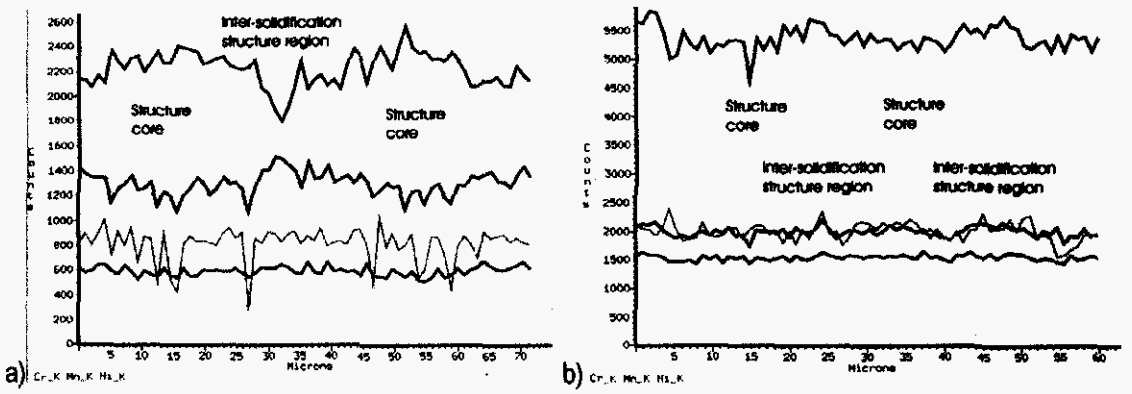

Fig. 50. Ni1 (a) and Ni3 (b) segregation profiles from EDS.

In Mn-based alloys with less than ten weight percent manganese, the segregation profile of chromium mirrors that of manganese. For the case of alloys with manganese content above ten weight percent, chromium had it maximum at the region that solidified last. Although manganese segregation was observed to be lower in these alloys, its maximum was at the same region as that for chromium. (Figure 51).

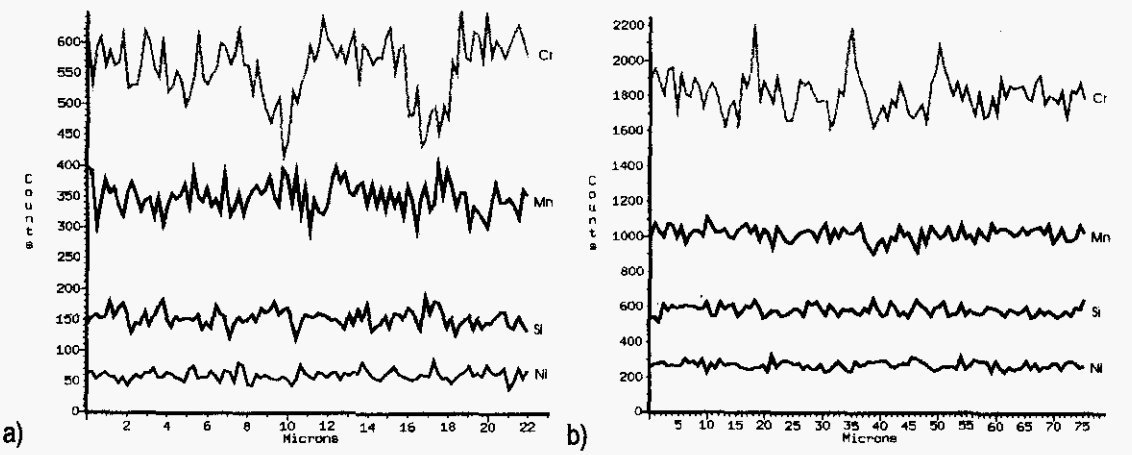

Fig. 51. Mn5 (a) and Mn6 (b) segregation profiles from EDS.

From this segregation study, compositional boundaries between primary solidification phases can be proposed (dashed line in Figure 51): Chromium to nickel equivalents ratios of less than 1.55 result in primary austenitic weld metals being the manganese effect 0.66 times that of nickel (Nieq=0.66Mn). This is valid for Mn-based as well as for Ni-based weld alloys (Figure 50).

III.2.3: Evaluation of Weldability

For fatigue resistance perspective, two main characteristics were required from this weld metal: (1) To have a low Ms so a compressive residual stress was induced in the weld toe by means of phase transformations; (2) To have good bead morphology so no stress concentrators were created. The first involved the maximum fraction of transformed martensite at the latest possible stage of the cooling so the thermal contraction effect interference with the phase-transformation volumetric change was minimized and the second involved the modification of the molten metal fluidity.

The developed Mn-Cr-Si satisfies all the previously presented requirements. The thermal contraction effect is minimized since this alloy starts to transform to martensite at 187°C. Furthermore, the transformation ends well above room temperature (118°C), insuring the maximum possible formation of martensite. Metallographic and XRD analyses indicate that this composition results in over ninety volume percent martensite with some traces of ferrite, its primary phase (Figure

52). A good bead morphology was also evident of this weld metal (Figure 53 and Figure 54). The selection of manganese over nickel for the development of this weld metal was based on cost considerations.

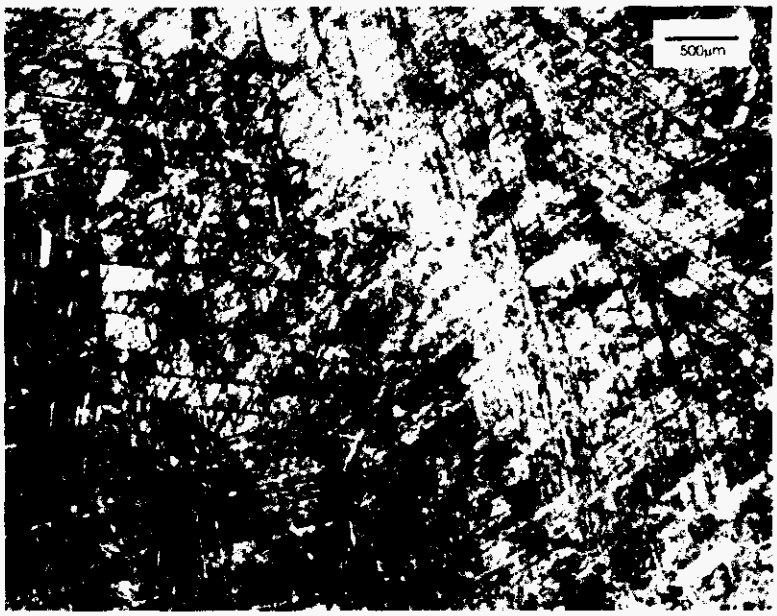

Fig. 52. Best effort weld metal metallography.

With the best effort weld metal (1.3mm diameter) partial penetration fillet joints were prepared using semi-automatic welding equipment. The obtained coupons exhibited good penetration and fusion (Figure 53). 32 Volts, 300 Amps., traveling speed of 381mm/min (15ipm), wire feeding speed of 148 mm/sec (350ipm), and 28lt/min (60cfh) of welding grade Helium as shielding gas was employed for their production. A flat welding position with a working distance of 12mm was employed. No preheating or post-weld treatment of any kind was performed in these welds made on quenched and tempered martensitic steel. The obtained coupons had a penetration in excess of 1mm and a profile with an average radius of curvature of the weld toe close to 2mm. No measurable undercut was found in any sample; neither any type of defect (inclusion, crack, porosity, etc.) was found. The fusion area didn't present any signs of abnormal segregation or material incompatibility and the fusion line was located over 1mm ahead of the original joint. Metallographic analyses revealed a high fraction of martensite contained in the weld metal (over 90%).

Fig. 53. Traditional fillet joint: General top view and transversal cut.

FASIP-methodology fillet welds were manufactured using the same best effort weld metal as well as two other leaner compositions on WELDOX-700 (quenched and tempered martensite, see Table 7 for details) steel plates. FASIP-compliant coupons were obtained with all of those weld alloys using similar parameters: 34.5 volts, 284mm/min (11.2 ipm) traveling speed, 190mm/sec (450ipm) feeding, currents of the order of 317amp. and a working distance of 22mm. The

welding gun was traveling 7° downwards a 7° tilted flat setup (arc perpendicular to the welding plane) and weaving at a frequency of 4Hz and amplitude of 3mm with a dwell time of 0.15 seconds. A typical industrial shielding gas mixture ($90Ar10CO_2$) flowing at 21lt/min (45cfh) was employed.

The resulting coupons showed no measurable undercutting but a much better geometrical shape than those obtained with the conventional welding technique. The throat reinforcement was reduced from over 1.5mm to almost zero, the average weld toe radius was increased to close to 4mm while still having a weld size of about 7mm and a penetration of over 1mm.

Fig. 54. FASIP fillet joint, best effort alloy: General top view and transversal cut.

III.2.4: Weld Residual Stress

Table 7. Chemistry Of Weldox 700 (Equivalent To CAT 1E1032) High Strength Structural Plate With Properties (YS=700mpa).

N	C	Mn	Si	P	S	Cr	Ni	Mo	Cu	V	Al	Ti
0.0051	0.129	1.197	0.337	0.013	0.0022	0.251	0.041	0.16	0.006	0.032	0.045	0.014

The FASIP compliant fillet coupons were used for residual stress analysis. X-ray diffraction (XRD) techniques were used for this. Longitudinal residual stress measurements were obtained using 9 exposures (20sec) with double detectors from -45° to 45°. Transversal residual stress measurements were obtained using similar methodology but with only 5 exposures. All of the measurements were done with a 2mm collimator distance. With the obtained information, a residual stress state pattern at the weld toe (on the continuous plate side) was obtained.

The analyses were performed at the middle section of the 150mm long specimens so start and finish welding transients were avoided. No previous treatment was done to the components other than typical cleaning with a grinding disc to remove any type of rolling slag or oxides. No post-weld mechanical or heat treatment was performed other than the weld-slag removal by means of metal wire manual brushing.

A correlation between the martensite start temperature and the maximum residual stress was found (Figure 55). The maximum compressive residual stress was always found in the region adjacent to the weld toe. As previous experiments indicated, the higher the Ms the lower the induced compressive residual stresses since the effect of the thermal contraction override the phase-transformation generated volumetric expansion.

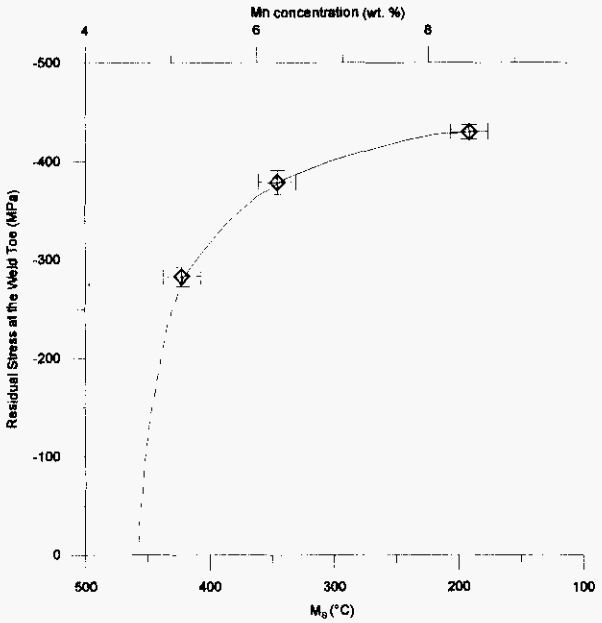

Fig. 55. Transversal residual stress measurements taken at the weld toe. Mn-based weld metals.

Only the best effort weld metal (Ms=180°C) stress field was completely mapped (Figure 56). The compressive field extended to 0.95mm under the surface, and surface level measurements at 2.54mm from the weld toe still indicated compression.

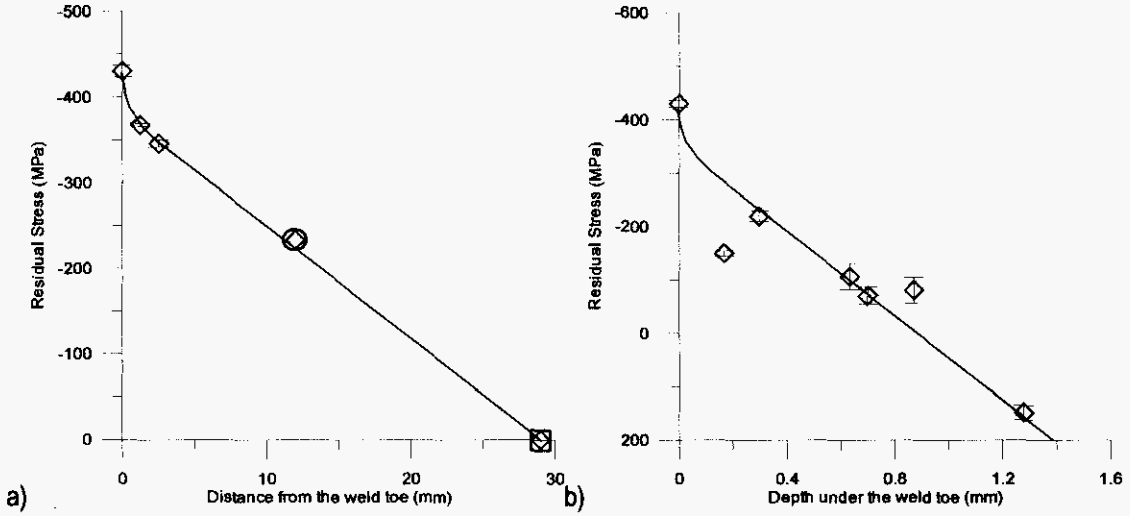

Fig. 56. Residual stress profile measured from the weld toe at the surface level (a) and underneath it (b). Best effort weld metal. X-ray diffraction measurements.

III.2.5: Evaluation of Weld Properties

Hardness measurements taken on different weld metal samples indicate a weld metal tensile strength of the order of 1 to 1.1Gpa; strength comparable to that of the high strength steels (Figure 55). Slightly higher hardness was measured in the fillet samples (XRD-coupons) than in non-diluted samples. This difference is clearly related to the carbon picking from the base material (0.05 wt. % C in the weld metal, 0.1 wt.% C in the base material).

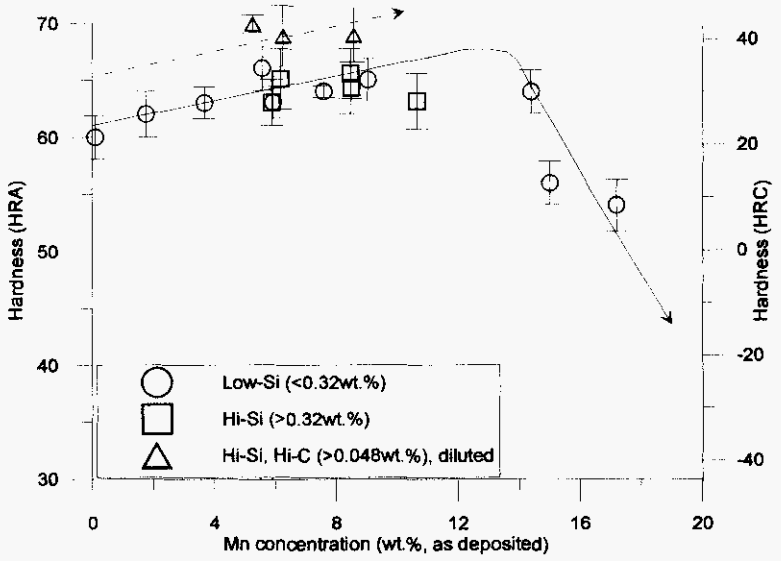

Fig. 57. Hardness measurements of Mn- based weld metals.

Charpy V-notch toughness analysis performed on the best effort weld metal revealed low energy absorption upon impact. The results indicate that there is a direct correlation between carbon content at the joint and the amount of absorbed energy during impact (Figure 58). Samples with lower carbon concentration (0.05wt. % C) were obtained when welding with higher fractions of CO2 in the shielding gas. The samples with lower carbon concentration exhibited the higher toughness at any testing temperature (Figure 59).

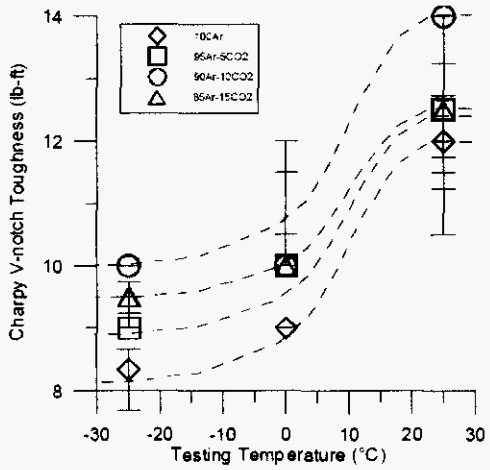

Fig. 58. Charpy V-notch toughness measurements of high carbon content coupons (0.10 to 0.17 wt. % C).

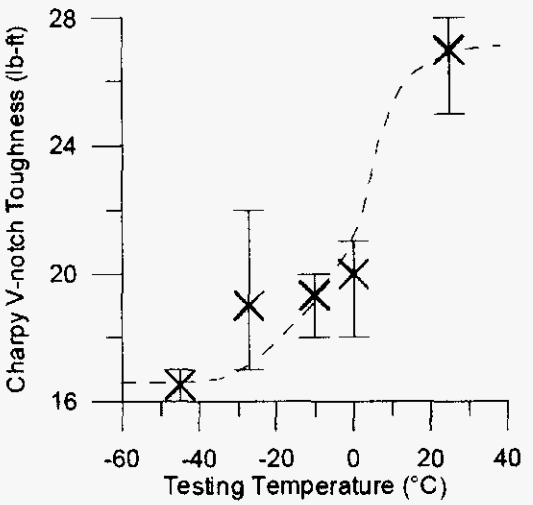

Fig.e 59. Charpy V-notch toughness measurements of low carbon content coupons (0.05wt. % C).

Detailed SEM inspection revealed that the low-carbon samples did not exhibit any brittle fracture surfaces. The entire surface of all the tested coupons exhibited mostly dimpled surface, evidence of ductility of the twinned martensitic matrix. Only the specimens tested at -45°C presented a modest (less than 10% of the total area) brittle broken surface (see Figure 60a).

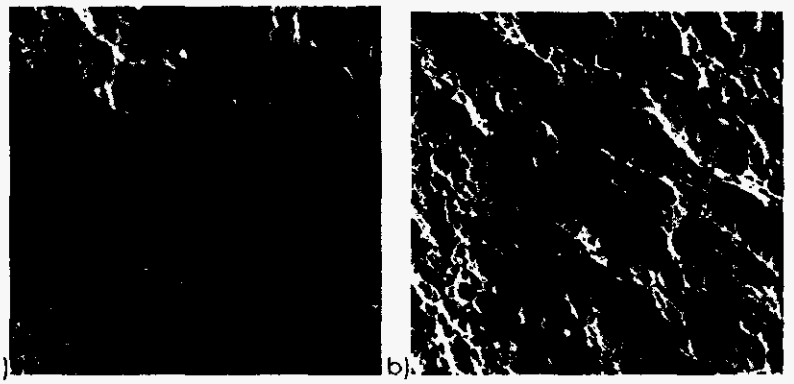

Fig.e 60. Fracture surface of the low carbon containing coupons. Tested at -45°C (a) and +25°C (b).

III.2.6: Conclusions

- A methodology that altered weld metal composition for the purpose of creating a compressive residual stress field in steel structural welds toes was established.
- Segregation of chromium, nickel, and manganese are responsible for the encountered differences between evaluated and predicted M_S temperatures. The differences are not systematic and are related to the partitioning behavior these elements manifest for different steel phases.
- In primary austenitic compositions, nickel, manganese and chromium exhibit a maximum concentration at the region where the last liquid solidified.
- In weld metals, primary austenite forms when Cr_{eq} to Ni_{eq} ratios are less than 1.52, while primary ferrite forms at higher ratios. Within the range of compositions of this study, the conversion for the manganese effect to nickel is 0.6 (e.g. Ni_{eq}=0.6Mn). This conversion should be expected to increase slightly as the manganese content is raised.
- A direct correlation between the martensite start temperature and the magnitude of the induced compressive residual stress exists.
- Silicon additions and modifications to welding parameters can alter the morphology of weld beads. As little as

0.4-wt %-Si addition will noticeably improve the bead morphology of Mn-Cr-based GMA welds in steel.

- A Mn-Cr-Si weld alloy that induces a 430MPa compressive stress field at the weld toe by means of the martensitic transformation has been developed. This field is maximum at the weld toe surface.
- Low cost welds possessing good morphology and fatigue resistance can be produced using conventional welding parameters and shielding gases with these Mn-Cr-Si weld metals.

III.3: Technical Demo on Weld Fatigue Life Improvement in High Strength Steel Welds

A technical demo has been made in applying Virtual Welded-Joint Design approach to design fatigue resistant high strength steel welds. In the demo, non-load carrying cruciform joints have been produced for both mild and high strength steels using special welding wire, low temperature transformation wires (LTTW). It should be pointed out that three special welding wires (LTTW 1, LTTW 2, and LTTW 3) have been evaluated for fatigue life improvement. All of the special welding wires were developed to have low temperature martensite transformations. LTTW 3 is the wire developed in this project. LTTW 1 and LTTW 2 were obtained from external manufacturers to investigate the effects of compressive residual stress on weld fatigue life improvement. Weld residual stresses have been measured using neutron and x-ray diffractions at ORNL. The predicted residual stresses from modeling are comparable with the measurement results. In particular, compressive residual stress can be obtained at weld toe if special welding wire used. All test specimens were welded by FASIP welding, which gives better fit up and smoother toe shape and results in longer fatigue life. This compressive residual stress combined with the desired weld bead shape can lead to more than 10× fatigue life improvement in high strength steel welds. Both fatigue test and modeling prediction have validated this result.

III.3.1: Fatigue Test Sample Preparation

Non-load carrying cruciform joint specimens was prepared as shown in Figure 62. This flat bar shape was determined in accordance with the test equipments at Caterpillar in order to minimize the fabrication cost of specimens.

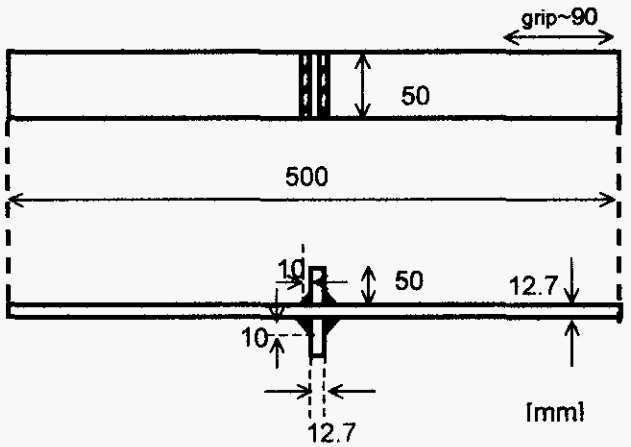

Fig. 61: Fatigue test specimen geometry

Panels of 500 mm (L) * 700 mm were welded by applying FASIP welding to obtain welds with large toe radius for lower stress concentration factor. The shielding gas consists of 85% Ar + 15%CO_2 for LTTW and 90% Ar + 10%CO_2 are used for the conventional consumable. The long welded panels were then cut into the specimens, as shown in Figure 62, for fatigue test. The mechanical properties and chemical compositions of steel plates were examined and the results are shown in Table 8 and Table 9.

Table 8: Mechanical Properties of Steel Plates (Average value of two specimens) and LTTW.

Material	Yield Strength, 0.2% offset	Ultimate Strength	Elongation	Reduction of Area
	MPa	MPa	%	%
MS	370	456	38.4	81
HS	758	822	19.6	55

Table 9: Chemical Composition of Steel Plates (Wt %).

Mat.	C	Mn	P	S	Si	Ni	Cr	Mo	Cu	Al	B	Ti	Zn	Nb	V
MS	0.06	0.90	0.016	0.004	0.04	0.01	0.02	0.01	0.02	0.032	0.0000	0.002	0.00	0.01	0.00
HS	0.19	1.24	0.012	0.006	0.33	0.01	0.15	0.04	0.01	0.045	0.0023	0.032	0.00	0.00	0.06

III.3.2: Weld Profile

The joint profile was measured, as shown in Figure 62, and the stress concentration factor was calculated. Joint profile was measured by utilizing macro pictures as shown in Figure 62 as an example. Stress concentration factor was calculated by the following equation. Toe number is identical to the welding sequences.

$$K_t = 1 + \{1.348 + 0.397 * \ln(S/t_1)\} * Q^{0.467} * f(\theta)$$

$$f(\theta) = \{1 - \exp(-0.9 * \beta * \theta)\} / \{1 - \exp(-0.9 * \beta * \pi/2)\}$$

$$Q = l_2 / \rho / 2.8(W/t_1)$$

$$W = t_1 + 2l_2$$

$$S = t_2 + 2l_1$$

$$\beta = \{W/2l_2\}/2$$

where t_1: main plate thickness (mm)
t_2: thickness of attachment (mm)
□: frank angle at toe (radian)
l_1: weld leg length (mm)
l_2: weld height (mm)
□: radius at weld toe (mm)

The values of stress concentration factors are around 2.0 for all toes. These SCF values are much lower than those from welds with conventional bead shape. Note those data are representatives produced from only one section.

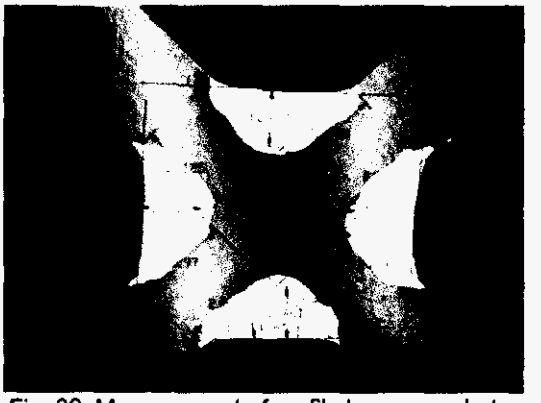

Fig. 62: Measurement of profile by macro photo.

III.3.3: Weld Residual Stress

One of the major concerns in this research is the residual stress around the weld toe. The purpose of using LTTW is to introduce compressive residual stress in welds for weld fatigue improvement. Measurement of the residual stress at the weld toe is challenging due to the steep stress gradient around the welds. In this project, neutron and x-ray diffractions at ORNL were used to measure weld residual stress. The measured residual stresses were compared with the results from the simulation. The proposed measurement plan is given in Figure 63.

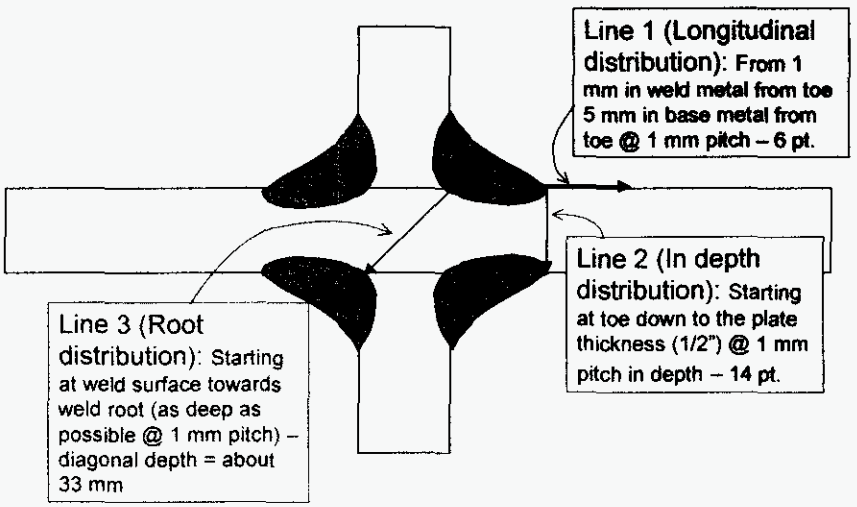

Fig. 63: Proposed plan for weld residual stress measurement using neutron diffraction (line 2 and line 3) and x-ray diffraction (line 1).

Line 1 was measured using x-ray diffraction for residual stress on the surface. Lines 2 and 3 were planned to be measured using neutron diffraction for residual stress distribution within the welds. The set-up for neutron diffraction for the cruciform-joint was given in Figure 64. Due to the limited working time for neutron facility, only the residual stresses along line 2 have been measured so far. From the perspective of fatigue life prediction at weld toe failure, the residual stress data along line 2 are sufficient. Knowledge of residual stress along line 3 can be used for cases with weld root failure, which is the typical failure mode for load-carrying welded-joint.

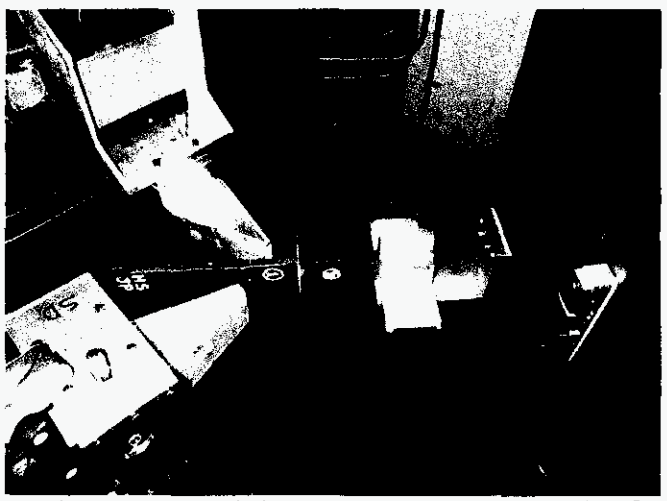

Fig. 64: Neutron scattering experiments were carried out on the new Neutron Residual Stress Facility (NRSF2) at ORNL.

III.3.3.1: Simulated Weld Residual Stress

Welded residual stresses were simulated for both conventional welding wire and special welding wire. Since the stress-strain curves at elevated temperatures are not available, the prediction for special welding wire is an approximation. The primary purpose is to simulate the effect of martensite transformation on the weld residual stress formation. The simulated transverse weld residual stresses in direction 1, which is the fatigue test loading direction, are shown in Figure 65. It can be observed that tensile residual stress was formed at weld toe in the weld with conventional wire. In contrast, compressive residual stress was at weld toe with special welding wire. The analyzed residual stress along the thickness of plate in loading direction, which is critical for fatigue life prediction, is shown in Figure 66 with tendency lines. Five points of data were extracted from the analysis results, thus the 4th order polynomials fit perfectly.

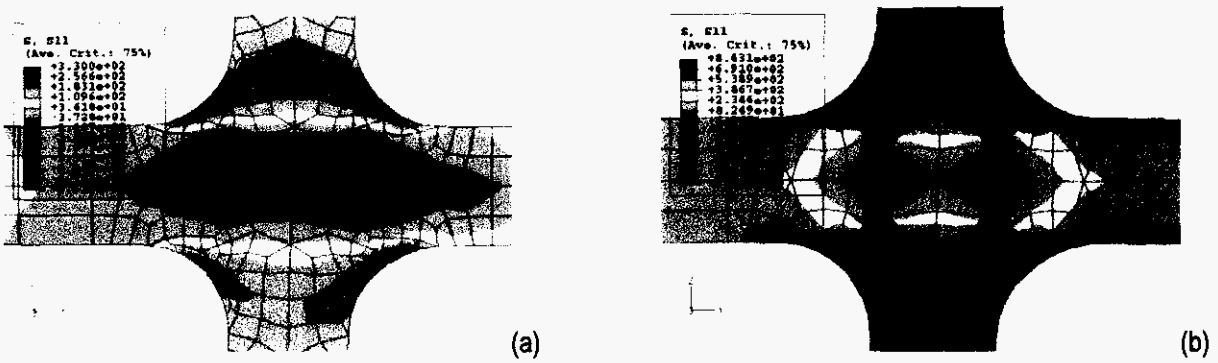

Fig. 65: Simulated residual stress (S11) in the welds with (a) conventional welding wire and (b) special welding wire.

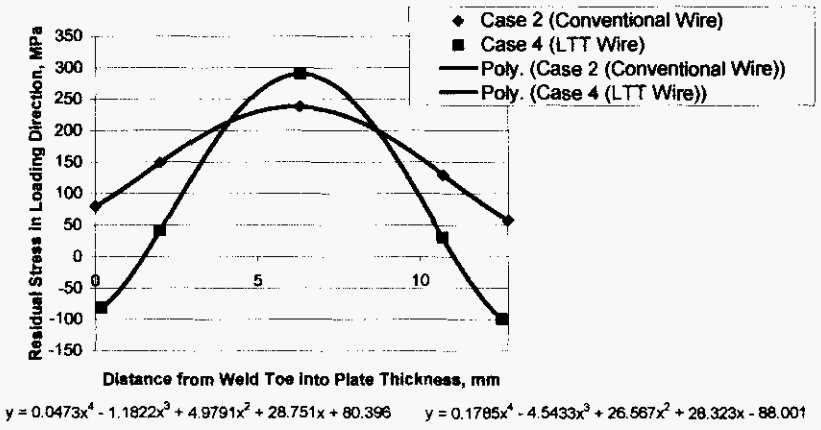

Fig. 66: Residual Stress Distribution from Welding Simulation.

III.3.3.2: Measured Residual Stress

Neutron diffraction measures residual strain in thickness, thus strain was converted with the following equation:

$$\sigma_x = \frac{E_N}{1+\nu}\left\{\varepsilon_x + \frac{\nu}{1-2\nu}\left(\varepsilon_x + \varepsilon_y + \varepsilon_z\right)\right\},$$

where E_N: Young's Modulus for neutron diffraction;

ν: Poison's ratio;

$\varepsilon_x, \varepsilon_y, \varepsilon_z$: Measured strain in x, y, z direction.

E_N=243 GPa, ν=0.28 from a literature [14] is used since we do not have measured data. Since neutron diffraction

data was available from certain depth such as 0.25 mm, surface residual stress were obtained by averaging extrapolated neutron diffraction stress and X-ray stress.

Fig. 67 shows processed measured strain with fitted 5th order polynomials. The fitted 5th order polynomials were used as input to fatigue model for life prediction. Comparing the measured residual stresses with the simulation results, we can see there are some discrepancies through the plate thickness. However, the patterns of the measured residual stresses on and near the surface for the investigated 3 welded-joints are consistent with those from the simulation, i.e., tensile residual stress at weld toe with conventional welding wire and compressive residual stress at weld toe with special welding wires.

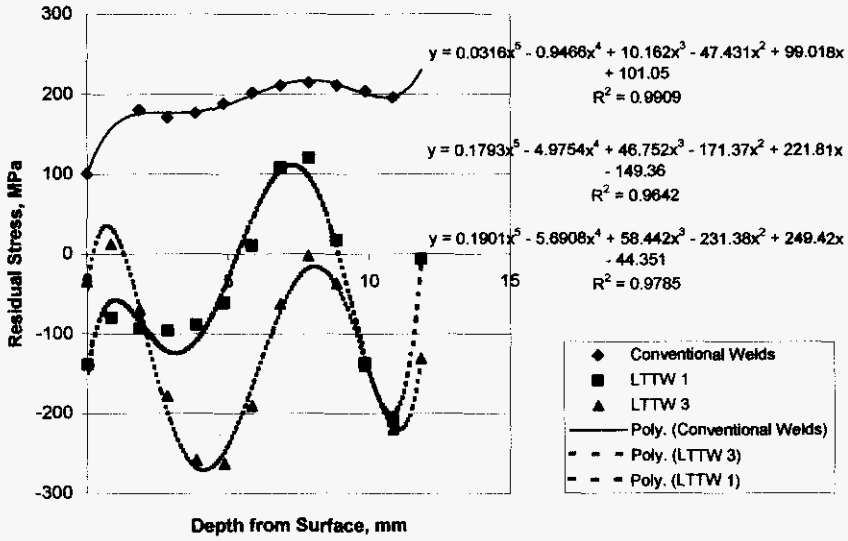

Fig. 67: Residual Stress Distribution from Measured Data. LTTW 3 is the wire developed in this project and LTTW 1 is a special welding wire from another manufacturer.

III.3.4: Fatigue Test and Model Prediction

The fatigue test results and fatigue life prediction for the welded-joints using both conventional and special welding wires are summarized in this section. The wire developed in this project by Colorado School of Mines is named LTTW 3, while the other two special welding wires (LTTW1 and LTTW2) were obtained from other manufacturers to investigate the effects of compressive residual stress on weld fatigue life improvement. The fatigue test results for the conventional and three special welding wires are shown in Figure 68 (Caterpillar's proprietary information and not provided in this report).

The results from the fatigue test show significant high fatigue performance by the combination of high strength steel and LTTW. For example, the fatigue life for the welded-joint using LTTW1 is more than 10 times higher than that from BS 7608 F-class mean curve at stress range of 400 MPa. Mild steel with LTTW consumables specimens had similar results to high strength steel with conventional consumables specimens around B-class mean curve of BS 7608.

In this Figure, it can be observed the weld fatigue life using the combination of FASIP weld bead shape and LTTW1 is more than 4x higher than that using FASIP bead shape alone. This means compressive residual stress at weld toe can lead to significant extra fatigue life improvement building on the FASIP welds. On the other hand, the weld fatigue test data are also compared with the data in literature, in which only the special wire was used and the effect of weld bead shape was not considered. We found that the weld fatigue strength by the combination of FASIP and special consumable is much higher than that using special consumable alone in literature. In conclusion, the fatigue strength of welds using the combination of the technologies is much higher than that using FASIP welds or special

consumable alone.

The two-stage crack growth weld fatigue model was evaluated by utilizing coupon fatigue test results of conventional wire joints and three kinds of low temperature transformation welding wire joints. As shown in Figure 68, the simulated life prediction agrees with high ends of LTTW fatigue test results, which are the fatigue life from LTTW 1. Considering the simulation results have all kinds of idealistic situation, this validation shows the maximum attainable S-N curve from LTTW wire welding.

III.3.5. SUMMARY

1. The fatigue test results have shown more than 10x fatigue life improvement in high strength steel welded-joints could be achieved by the combined effects of weld bead shape with lower stress concentration factor and compressive residual stresses from special welding wire. The fatigue strength of welds using the combination of the technologies is much higher than that using FASIP welds or special welding wire alone.

2. The predicted fatigue lives using two-stage crack growth model considering the effect of compressive residual stress with LTTW wire welds are in a reasonable agreement with the high end of fatigue test results.

IV. Accomplishments

Through the project, we have achieved our proposed project objective, which is to improve the fatigue life by 10x for high strength steel welded-joints based on a systematic "Virtual Welded-Joint Design" approach. Two major technologies have been generated from this project: (1) a systematic simulation approach for virtual welded-joint design and (2) the technology to increase high strength steel weld fatigue strength by the combination of compressive residual stress from special welding wire and the desired weld bead shape from an unique welding process. Figure 69 is a schematic summary of the accomplishment of Virtual Welded-Joint Design project.

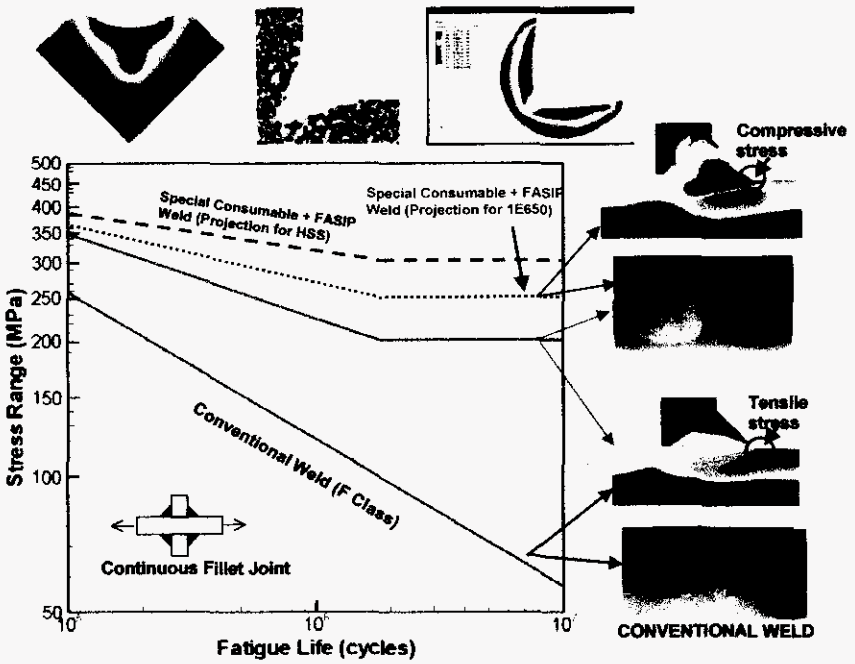

Fig. 69: Schematic diagram summarizes the fatigue strength improvement for high strength steel welds based on the systematic Virtual Welded-Joint Design approach.

In virtual welded-joint design, the accomplishments in modeling include:

(a) Development of a 3D thermo-fluid model to predict weld bead shape for GMA welding with free surface, which can be used to design welding parameters for desired weld bead shape;
(b) Modification of a weld microstructure model to predict the phase transformations and grain growth in the weld fusion zone and heat affected zone;
(c) Establishment of the relation of weld properties (strength, hardness, stress-strain curves) vs. weld microstructure;
(d) Enhancement of a weld residual stress model by the incorporation of the effects of phase transformations (e.g. volume change and transformation induced plasticity);
(e) Development of a two-stage crack growth model for the weld fatigue life prediction considering the effect of residual stress.

The Virtual Welded-Joint Design approach has been used for the design of welding process parameters and welding wire for structurally sound and fatigue resistant welded-joints. The fatigue test results and modeling prediction both show more than 10x fatigue life improvement based on the systematic "Virtual Welded-Joint Design" approach by considering the combined the effects of weld bead shape, residual stress, and microstructure.

The accomplishments for practical applications in this project include the development of a unique welding procedure (welding wire + welding process) for making fatigue resistant welded-joints. The weld bead shape with larger toe radius and thus lower stress concentration was obtained by adopting a Caterpillar proprietary welding process through optimizing welding parameter. The compressive residual stress at weld toe was achieved by using special welding wires. The results from neutron and x-ray diffraction analysis show that compressive residual stresses were formed in the welded-joints using special welding wires. In contrast, tensile residual stresses exist at the weld toe using conventional welding wire. More then 10X fatigue life improvement has been achieved in high strength steel welds by the combination of the desired weld bead shape and compressive residual stresses.

The extensive research work pursued in this project has resulted in the publication of 6 technical paper and 9 technical presentations at international conferences, which are detailed in the "Technology Transfer and Commercialization" section in this report.

V. Conclusions

The results from this project have clearly demonstrated that the fatigue strength of high strength steel welds can be significantly improved by the systematic design approach considering the weld bead shape, residual stress, and microstructure. The results reported here indicate a breakthrough of fatigue strength improvement in high strength steel welds.

1. The 3D transient thermo-fluid model developed in this project is able to simulate the complex heat transfer and fluid flow phenomena in GMA weld pool. The model can be used to predict weld bead formation for various types of welded-joints including butt and T-fillet joints. The results here indicate the significant promise to use weld thermo-fluid model to design desired weld bead shape for high performance welded-joint.
2. The inhomogeneous microstructures in both the weld fusion zone and the heat-affected zone can be predicted by coupling a modified weld microstructure model with the thermal cycles from thermal model. Some weld material properties such as yield strength and hardness can be predicted accordingly based on the predicted microstructures.
3. The effect of phase transformations on weld residual stress formation can be effectively simulated after the incorporation of the transformation-induced plasticity in the residual stress model.
4. The structural stress based two-stage crack growth weld fatigue model is effective in the prediction of the effect of residual stress on weld fatigue life.
5. The special welding wire developed in this project can introduce compressive residual stress at weld toe.
6. The fatigue life/strength in high strength steel welds can be significantly improved by the combination of weld bead shape, residual stress, and microstructure.

VI. Technology Transfer and Commercialization

For the purpose of technology transfer and commercialization, one technical paper has been published in a peer-reviewed journal and 5 technical papers have been published in conference proceedings. Nine technical presentations have been made at International conferences and 3 presentations made at Corporate level technical forum within Caterpillar. An advisory committee, which includes members from different industrial sectors, welding institutes (Edison Welding Institute and The Welding Institute), and national laboratories, was formed to diffuse the technologies developed in this project.

The models developed in this project have been applied within Caterpillar for both R&D and technical assistance projects. Caterpillar has also allocated new research funding to further evaluate and benchmark the welding wire and procedure for fatigue life improvement in high strength steel welds. The ultimate goal is to apply the fatigue resistant welded-joints for the design of high performance and lightweight fabricated structures.

Publications

Technical Papers

1. Z. Yang, X. L. Chen, N. Chen, H. W. Ludewig and Z. Cao: "Virtual Welded-Joint Design by Coupling Thermal-Metallurgical-Mechanical Modeling", in Proceedings of 6th Intl. Conf. On Trends in Welding Research, ASM International, Pine Mountain, GA, April 2002.
2. Z. Yang, Z. Cao, X. L. Chen, and H. W. Ludewig: "Virtual Welding – Applying Science to Welding Practices", in the proceedings of the 8th Intl. Conf. On Numerical Methods in Industrial Forming Processes, American Institute of Physics, Columbus, OH, June 2004, p.1308.
3. Z. Cao, Z. Yang, and X. L. Chen: ""Three-Dimension Simulation of GMA Weld Pool with Free Surface", Welding Journal, vol. 83, 2004, p.169s.
4. X. L. Chen, Z. Yang, A. Nanjundan, and N. Chen: "Achieving manufacturing quality and reliability using thru-process simulation", *Journal de physique. IV, Colloque : JP.* 120, (2004): 793 (8 pages).
5. X. L. Chen, Z. Yang, and F. W. Brust: Chapter 7 *"Modeling distortions and residual stress during welding: practical applications"* in the book "Processes and Mechanisms of Welding Residual Stress and Distortions", to be published by Woodhead Publishing.
6. F. Martinez, S. Liu, and G. Edwards: "The Development of a Compressive Residual Stress Around Structural Steel Weld by Means of Phase Transformations" in the Proceedings of the ASM Materials Solutions 2004 Conference, Columbus OH, October 2004.

Technical Presentations

1. Z. Yang, X. L. Chen, N. Chen, H. W. Ludewig and Z. Cao: "Virtual Welded-Joint Design by Coupling Thermal-Metallurgical-Mechanical Modeling", 6th Intl. Conf. On Trends in Welding Research, ASM International, Pine Mountain, GA, April 2002.
2. Z. Yang, Z. Cao, X. L. Chen, and H. W. Ludewig: "Virtual Welding – Applying Science to Welding Practices, the 8th Intl. Conf. On Numerical Methods in Industrial Forming Processes, American Institute of Physics, Columbus, OH, June 2004.
3. Z. Yang, Z. Cao, X. L. Chen, N. Chen, and H. W. Ludewig: "Virtual Welded-Joint Design – A Systematic Modeling Approach for High Performance Welds", 83rd AWS Convention, Chicago IL, April 2002.
4. Z. Cao, Z. Yang, and X. L. Chen: ""Three-Dimension Simulation of GMA Weld Pool with Free Surface", 83rd AWS Convention, Chicago IL, April 2002.
5. F. Martinez, S. Liu, and G. Edwards: "The Development of a Compressive Residual Stress Around Structural Steel Weld by Means of Phase Transformations", International Conference on Joining of Advanced and Specialty Materials VII, Columbus OH, October 2004.
6. F. Martinez, S. Liu, and G. Edwards: "Improvement for Fatigue Resistance in Structural Steel Weldments though Microstructural Trans formations", Glen Edwards Commemorative Symposium, Golden CO, June 2003.
7. F. Martinez, S. Liu, and G. Edwards: "Effects of Manganese and Nickel on the Phase Stability of High Alloy Weld

Metals", 84th AWS Convention, Detroit MI, April 2003.
8. F. Martinez, S. Liu, and G. Edwards: "High Alloy Weldments for Fatigue Resistance in Structural Carbon Steel", 83rd AWS Convention, Chicago IL, April 2002.
9. W. Zhang, T. DebRoy, and G. G. Roy: "Modeling of Solidified Surface Profile in GTA Welded Butt and Fillet Joints", 83rd AWS Convention, Chicago IL, April 2002.

VII. Recommendations

(a) Further development is needed for the 3D transient thermo-fluid model, which should include the enhancement of the simulation of the effect of surface tension on the small droplets.
(b) The individual models so far can only be manually "integrated" due to the challenges such as different software involved and the long computational time for the weld thermo-fluid model. The models ideally should be integrated using a unified framework, which needs further research on model integration and the speed up of the welding pool simulation.
(c) For general engineering design applications, the fracture mechanics based fatigue model developed in this project should be further validated and refined by comparing fatigue life predictions with experimental testing for some selected joint types in which more complex 3D residual stress distributions dominate.
(d) Simplified residual stress models which can still provide adequate through-thickness resolution need to be developed to facilitate the day to day application of the fatigue model in fatigue design of complex engineering structures.
(e) Robust experimental residual stress measurement techniques for accurately resolving through-thickness distributions within a length scale of mm remain to be developed. Although neutron diffraction technique has a capability of measuring through-thickness distributions with a sampling volume of a few mm, the specimen size limitation (cannot be too big) limits the application of the neutron measurement techniques for some large specimens which are needed to fully contain the structural joint restraint effects on residual stresses in joints in actual structure.
(f) Further evaluation and benchmark of the special welding wire and procedure are recommended before applying this technology to production.

References

1. FLOW-3D User's Manual, Excellence in Flow Modeling Software, Version 7.7, Flow Science, Inc.
2. Hirt, C. W. and Sicilian, J. M. 1985. A porosity technique for definition of obstacles in rectangular cell meshes. *Proc. Fourth International Conf. Ship Hydro.*, National Academy of Science, Washington, DC.
3. Kou, S. and Le, Y. 1988. Welding Parameters and Grain Structure of Weld Metal - A Thermaldynamic Consideration. *Metall. Trans* 19A: 1075 to 1083.
4. H. K. D. H. Bhadeshia and L. -E. Svensson: in *Mathematical Modeling of Weld Phenomena*, ed. by H. Cerjak and K.E. Easterling, p. 109, Institute of Materials (1993).
5. G. M. Evans: "The effect of carbon on the microstructure and properties of C-Mn all weld metal deposits", IIW Doc. II-1094-87.
6. User Manual for UMAT-CAT – A Welding Specific User Material Routine Interfaced with ABAQUS, Version 3.1, Caterpillar Inc., Peoria, IL, September 1999.
7. F. D.Fischer, G. Reisner, K. Tanaka, "A New Look at Transformation Induced Plasticity (TRIP)", Mathematical Modelling of Weld Phenomena 5, pp. 449-465.
8. Dong, P. and Hong, J.K., " Consistent Treatment of Weld Residual Stresses in Fracture Assessment," Proceedings of ASME PVP Conference, August, 2002, Vancouver, Canada
9. Dong, P., "A Structural Stress Definition and Numerical Implementation for Fatigue Analysis of Welded Joints," *International Journal of Fatigue*, 23, pp. 865-876, 2001.
10. Toyosada, M., Niwa, T., and Sakai, J., "Physical Meaning of ΔK_{RP} and Fatigue Crack Propagation in the Residual Stress Distribution Field," *International Journal of Fatigue*, Vol. 19, Supp. No.1, pp.S161-S166, 1997.
11. Glinka, G., "Effect of Residual Stresses on Fatigue Crack Growth in Steel Weldments Under Constant and Variable Amplitude Loads," *Fracture Mechanics*, ASTM STP 677, C.W. Smith, Ed., pp.198-214, ASTM, 1979.
12. Maddox S.J., " Influence of Tensile Residual Stresses on the Fatigue Behavior of Welded Joints in Steel," *Residual Stress Effects in Fatigue*, ASTM STP 776, ASTM, pp.63-96, 1982.
13. A. Ohta: "Fatigue Strength Improvement by Using Newly Developed Low Transformation Temperature Welding Material", Welding in the World, vol. 43, No. 6, 1999.
14. M. Mochizuki, M. Hayashi, and T. Hattori: "Numerical Analysis of Welding Residual Stress and Its Verification Using Neutron Diffraction Measurement", Journal of Engineering Materials and Technology, Transactions of the ASME, Vol. 122, pp.98-103, January 2002.
15. B. Buchmayr: in *Proceeding of an international conference on Trends in Welding Research*, Pine Mountain, Georgia, 1998, p. 685.
16. W. Zhang, C.-H. Kim and T. DebRoy: *User Manual of Modeling of Heat Transfer, Fluid Flow and Free Surface Profile during Gas Metal Arc Fillet Welding*, Department of Material Science and Engineering, The Pennsylvania State University, July 2003.
17. A. H. Cottrell, Journal of Iron and Steel Institute, Vol. 1., 1945, 93-104.

Appendix A: Nomenclature for welding pool simulation

$\vec{B}$	magnetic induction vector, Tesla
C_p	specific heat, J/kgK
f	frequency of droplet transfer, 1/s
F_b	component of body force, N
$\vec{g}$	gravitational acceleration vector, m/s^2
h_c	convection coefficient, W/m^{2}K
I	welding current, A
$\vec{J}$	current density vector, A/m^2
K	thermal conductivity, W/mK
p	pressure, N/m^2
P_{arc}	arc pressure, N/m^2
q_{evap}	heat loss form evaporation, W/m^2
r	radial distance, m
R	radius of surface curvature, m
T	temperature, K
u_0	welding speed, m/s
u	x-direction velocity, m/s
V	arc voltage, V
V_τ	velocity component in the surface tangential direction
V_d	droplet transfer velocity, m/s
V_n	velocity component in the surface normal direction
v	y-direction velocity, m/s
w	z-direction velocity, m/s
μ	viscosity, kg/ms
μ_0	magnetic permeability ,H/m
ρ	density, kg/m^3
ρ_d	droplet density, kg/m^3
β	coefficient of volume expansion, 1/K
γ	surface tension, N/m
$\partial\gamma / \partial T$	surface tension temperature coefficient, N/mK
η	arc efficiency
σ	Stefan-Boltzmann constant, 5.67x10^{-8} W/m^{2}K^4
σ_q	arc heat flux distribution parameter\
σ_j	arc current flux distribution parameter
ε	surface emissivity, 0.8
τ	the tangential direction of the pool surface